

The Pennsylvania State University
The Graduate School
Department of Materials Science and Engineering

FERROELECTRIC POLYMERS FOR ELECTRICAL ENERGY STORAGE

A Dissertation in
Materials Science and Engineering
by
Jason W. Claude

© 2008 Jason W. Claude

Submitted in Partial Fulfillment
of the Requirements
for the Degree of

Doctor of Philosophy

December 2008

The dissertation of Jason W. Claude was reviewed and approved* by the following:

Qing Wang
Associate Professor of Materials Science and Engineering
Dissertation Advisor
Chair of Committee

Ralph H. Colby
Professor of Materials Science and Engineering

Michael Lanagan
Associate Professor of Engineering Science and Mechanics

Qiming Zhang
Professor of Electrical Engineering and Materials Science and Engineering

Joan Redwing
Professor of Materials Science and Engineering
Chair, Intercollege Graduate Degree Program in Materials Science and
Engineering

*Signatures are on file in the Graduate School

ABSTRACT

The energy storage properties of vinylidene fluoride based fluoropolymers were explored. Energy density is a function of a materials permittivity and electrical breakdown strength. High values of each of these parameters are desirable for a high energy density and were explored in various fluoropolymer systems. Copolymers containing vinylidene fluoride (VDF), chlorofluoroethylene (CTFE), and trifluoroethylene (TrFE) were synthesized by a two-step approach beginning with the copolymerization of VDF and CTFE and the subsequent hydrogenation of the CTFE units to TrFE to create the terpolymer P(VDF-CTFE-TrFE). By changing the chemical composition of the fluoropolymers, the permittivity was varied from 12 to 50 due to changes in the crystal phase that converted the polymers from paraelectric to ferroelectric materials.

The electrical breakdown mechanisms of a single copolymer composition of P(VDF-CTFE) was studied as a function of molecular weight and temperature. Energy density and breakdown strength increased as molecular weight increased and temperature decreased. An electromechanical breakdown mechanism was responsible for failure at 25°C while a thermal breakdown mechanism operated at -35°C which was below the glass transition of the material. In between at -15°C, a combination of the two mechanisms was found to operate.

Electromechanical breakdown was also found to operate in a copolymer system with a fixed amount of VDF and varying amounts of TrFE and CTFE. The molecular weights were identical for all the polymers. Maxwell stress is the primary contributor to the electromechanical stress in polymers with a high amount the CTFE. Electrostrictive stress due to a crystal phase change at high electric fields is a major contributor to the electromechanical stress in polymers containing a high amount of TrFE. Energy density and electrical breakdown strength increased with increasing amounts of TrFE.

Nanometer sized silica particles were incorporated into a P(VDF-CTFE) matrix using an in-situ sol-gel process. Electrical breakdown strengths and energy densities were maximized in hybrids containing an optimized amount of silica due to the creation of new charge trap sites. These sites reduced space charge and electric loss delaying thermal breakdown in the hybrids. For optimized composites, high energy densities over 20 J/cm³ were achieved.

TABLE OF CONTENTS

List of Figures.....	vi
List of Tables.....	ix
List of Equations.....	x
Acknowledgements.....	xi
Chapter 1 - Introduction.....	1
Historical Background.....	1
Capacitor Fundamentals.....	3
Review of Capacitor Technology.....	10
Electrical Double Layer Capacitors.....	10
Electrolytic Capacitors.....	14
Ceramic Capacitors.....	16
Polymer Capacitors.....	19
Research Goals.....	22
Chapter 2 - Synthesis and Characterization of P(VDF) Based Copolymers.....	26
Ferroelectric Fluoropolymer Review.....	26
Experimental Procedure.....	35
Materials.....	35
Solution Polymerization of P(VDF-CTFE) Copolymer.....	35
Hydrogenation Reaction of P(VDF-CTFE) Copolymer.....	36
Film Preparation.....	36
Characterization.....	37
Results and Discussion.....	37
Chemical Synthesis of Polymers.....	37
Polymer Tacticity.....	39
Thermal Properties.....	43
Crystal Structure.....	47
Dielectric Properties.....	51
Chapter 3 - Electrical Breakdown in P(VDF-CTFE) Copolymers.....	62
Electrical Breakdown Review.....	62
Experimental Procedure.....	68
Materials.....	68
Emulsion Polymerization of P(VDF-CTFE) Copolymer.....	68
Film Preparation.....	68
Characterization.....	69
Results and Discussion.....	70
Molecular Weight Characterization.....	70
Thermal Properties.....	71
Crystal Structure.....	73
Dielectric Properties.....	74
Mechanical Properties.....	77
Electrical Breakdown.....	81
Energy Densities of the Copolymers.....	90
Chapter 4 - Electrical Breakdown in P(VDF-CTFE-TrFE) Terpolymers.....	92

Introduction.....	92
Experimental Procedure.....	93
Materials.....	93
Emulsion Polymerization of P(VDF-CTFE) Copolymer.....	93
Hydrogenation Reaction of the P(VDF-CTFE) Copolymer.....	94
Film Preparation.....	94
Characterization.....	95
Results and Discussion.....	95
Dielectric Properties.....	95
Crystal Structure.....	98
Thermal Properties.....	100
Mechanical Properties.....	101
Electrical Breakdown.....	102
Energy Density.....	108
Chapter 5 - Electrical Energy Storage in SiO ₂ -P(VDF-CTFE) Hybrid Materials.....	110
Polymer Composite Dielectrics Review.....	110
Experimental.....	115
Materials.....	115
Solution Polymerization of Triethoxysilyl Terminated P(VDF-co-CTFE) Copolymer.....	115
Film Preparation.....	116
Characterization.....	117
Results and Discussion.....	118
Synthesis of SiO ₂ -P(VDF-CTFE) Hybrid Materials.....	118
Structure of Hybrids.....	120
Thermal Properties.....	123
Dielectric Properties.....	123
Electrical Breakdown.....	127
Mechanical Properties.....	128
High Field Electric Displacement.....	129
Thermally Stimulated Discharge Current Measurements.....	134
Chapter 6 - Conclusion.....	144
Summary of the Results.....	144
Suggested Future Work.....	149
Appendix A: Thermal Properties of the Hydrogenated Polymers.....	152
Appendix B: Dielectric Properties of the Hydrogenated Polymers.....	154
Appendix C: Weibull Plots for the P(VDF-CTFE) 78.4-21.6 mol% Copolymers.....	167
Appendix D: Derivation of the Temperature Versus Electric Field Equation.....	169
Appendix E: Weibull Plots for the 73.6 mol% VDF Polymers.....	171
Appendix F: Derivation of the Electrostatic Maxwell Stress.....	172
Appendix G: Constants for the Electromechanical Stress Calculations.....	173
Appendix H: Thermal Properties of the SiO ₂ -P(VDF-CTFE) Hybrids.....	174
Appendix I: Electrical Breakdown Data for the SiO ₂ -P(VDF-CTFE) Hybrids.....	175
Appendix J: Thermally Stimulated Discharge Current Data for the SiO ₂ -P(VDF-CTFE).....	176
References.....	179

LIST OF FIGURES

Figure 1 - Leyden jar. Note the foil covering and chain electrode inside the jar. Source: Reference 4.	2
Figure 2 - Increase in capacitance upon filling a capacitor with a dielectric.....	5
Figure 3 - Frequency response of the various polarization mechanisms. Source: Reference 8.	9
Figure 4 - Left: Schematic of EDL and diffuse layers. Right: Geometry of EDL capacitor.....	11
Figure 5 - Equivalent circuit of EDL capacitor.	12
Figure 6 - Grahame’s model of the EDL interface. Source: Reference 13.....	13
Figure 7 - Construction of an electrolytic capacitor.	15
Figure 8 - Top left: Disk capacitor. Top right: Tube capacitor. Bottom: Multilayer capacitor.....	18
Figure 9 - Double metalized polymer layer structure.	21
Figure 10 - Ragone plot of energy storage technologies. Source: Reference 27.....	23
Figure 11 - The α crystal phase of P(VDF). Left: Chain conformation. Right: Unit cell. Source: Reference 30.	27
Figure 12 - The strongly polar β crystal phase of P(VDF). Left: Chain conformation. Right: Unit cell. Source: Reference 30.	27
Figure 13 - The γ crystal phase of P(VDF). Left: Chain conformation. Right: Unit cell. Source: Reference 31.	28
Figure 14 - The δ crystal phase of P(VDF). Left: Chain conformation. Right: Unit cell. Source: Reference 30.	29
Figure 15 - P(VDF) crystal phases processing routes. Source: Reference 31.	30
Figure 16 - P(VDF-TrFE) paraelectric-ferroelectric phase diagram. Source: Reference 38.....	32
Figure 17 - Two step synthetic scheme for making the terpolymers.....	38
Figure 18 - Melting temperatures of all the polymers synthesized by two step synthesis procedure.....	44
Figure 19 - DSC heating curves for 79.2 mol% VDF polymers.....	46
Figure 20 - DSC cooling curves for 79.2 mol% VDF polymers.	46
Figure 21 - Optical microscope image of P(VDF-TrFE) 84.8/15.6 mol% at 400x of the same area. Left: Unpolarized. Right: Crossed polarizers.	48
Figure 22 - FTIR spectra for the 78.8 mol% VDF grouping of polymers.....	50
Figure 23 - Conformation as function of temperature for P(VDF-CTFE-TrFE) 81.2/7.2/11.6 mol%.....	51
Figure 24 - Room temperature permittivity and loss tangent versus frequency for 78.8 VDF mol% polymers.	53
Figure 25 - Room temperature permittivities of the polymers at 1 kHz.	54
Figure 26 - Temperature varying dielectric properties on heating for P(VDF-CTFE-TrFE) 78.8/0.0/21.2 mol%.....	55
Figure 27 - Zoomed plot of temperature varying dielectric properties on heating for P(VDF-CTFE-TrFE) 78.8/0.0/21.2 mol%.....	56

Figure 28 - Temperature varying dielectric properties on heating for P(VDF-CTFE-TrFE) 78.8/14.0/7.2 mol%.....	58
Figure 29 - Temperature varying dielectric properties on cooling for P(VDF-CTFE-TrFE) 78.8/14.0/7.2 mol%.....	59
Figure 30 - Curie transition and melt temperatures for the dielectric data. T_c data collected for the dielectric heating cycles.....	61
Figure 31 - Peak permittivity values from dielectric data measured at 1 kHz on the heating cycle.....	61
Figure 32 - DSC heating curves of the P(VDF-CTFE) 78.4-21.6 mol% copolymers.....	72
Figure 33 - DSC cooling curves of the P(VDF-CTFE) 78.4-21.6 mol% copolymers.....	72
Figure 34 - Diffraction patterns for the P(VDF-CTFE) 78.4-21.6 mol% copolymers.....	73
Figure 35 - Permittivity versus frequency measured at 25°C for the P(VDF-CTFE) 78.4-21.6 mol% copolymers.....	75
Figure 36 - Permittivity versus temperature upon heating for the 294k P(VDF-CTFE) 78.4/21.6 mol% copolymer.....	76
Figure 37 - Complex mechanical properties of the 294k P(VDF-CTFE) 78.4-21.6 mol% copolymer.....	78
Figure 38 - Summarized complex moduli for the P(VDF-CTFE) 78.4-21.6 mol% copolymers.....	79
Figure 39 - Stress versus strain plot for the 294k P(VDF-CTFE) 78.4-21.6 mol% copolymer.....	80
Figure 40 - Diagram of the electrostatic pull-down electrical breakdown strength testing method.....	82
Figure 41 - Summarized α breakdown results for the P(VDF-CTFE) 78.4 21.6 mol% copolymers.....	84
Figure 42 - Images of 294k copolymer after breakdown testing. Image dimensions are approximately 5 by 5 cm. a. 25°C; b. -15°C; c. -35°C.....	86
Figure 43 - Temperature versus electric field for thermal impulse breakdown.....	88
Figure 44 - Combined experimental and predicted values for the 294k copolymer.....	90
Figure 45 - Low electric field dielectric properties of the 73.6 mol% polymers.....	97
Figure 46 - Diffraction pattern of the 73.6 mol% VDF polymers with varying hydrogenation levels.....	98
Figure 47 - Conformation as measured by FTIR for the 73.6 mol% VDF polymers.....	100
Figure 48 - Optical microscope images of polymers from the 73.6 mol% polymers. a, c - 26.4 mol% TrFE without and with crossed polarizers respectively. b, d - 19.3 mol% TrFE without and with crossed polarizers respectively.....	102
Figure 49 - Measured electrical breakdown strengths of the 73.6 mol% VDF polymers at 25°C.....	103
Figure 50 - Electric displacement versus electric field for the 73.6 mol% VDF polymers.....	106
Figure 51 - Energy density, and experimental and measured breakdown strengths for the 73.6 mol% VDF polymers.....	109
Figure 52 - Synthetic scheme for the triethoxysilyl-benzoyl functionalized copolymer.....	118
Figure 53 - Schematic of the SiO ₂ -P(VDF-CTFE) hybrid formation.....	119
Figure 54 - WAXD of the SiO ₂ -P(VDF-CTFE) hybrids.....	121

Figure 55 - Photographs of the SiO ₂ -P(VDF-CTFE) hybrids. Left - 0.00 wt. %. Right - 3.38 wt. %.	121
Figure 56 - Left: TEM image of the SiO ₂ -P(VDF-CTFE) hybrid with 3.38% SiO ₂ . Right: Silicon elemental EDS image of hybrid.	122
Figure 57 - Low electric field dielectric properties of the SiO ₂ -P(VDF-CTFE) hybrids.	125
Figure 58 - Temperature varying dielectric properties of the 0.24 wt.% SiO ₂ hybrid.	127
Figure 59 - Electrical breakdown strengths of SiO ₂ -P(VDF-CTFE) hybrids.	128
Figure 60 - Yield stresses and moduli of the SiO ₂ -P(VDF-CTFE) hybrids.	129
Figure 61 - Electric displacement measurements of the hybrid materials at 1 Hz.	130
Figure 62 - Electric displacement measurements of the hybrid materials at 100 Hz.	132
Figure 63 - High field losses calculated for all the hybrid materials at 10 Hz.	133
Figure 64 - Energy storage values of the 0.43 wt. % hybrid.	134
Figure 65 - Schematic of the TSDC measurement technique.	135
Figure 66 - Positive TSDC curves for the 0.00 wt. % hybrid at a constant heating rate.	137
Figure 67 - Negative TSDC curves for the 0.00 wt. % hybrid at a constant heating rate.	139
Figure 68 - Full TSDC curves for the 0.00 wt. % hybrid at a constant poling field.	139
Figure 69 - Positive TSDC curves for the 0.34 wt. % hybrid at a constant heating rate.	140
Figure 70 - Negative TSDC curves for the 0.34 wt. % hybrid at a constant heating rate.	141
Figure 71 - Composite of the three hybrids at a constant heating rate and poling field.	143

LIST OF TABLES

Table 1 - Permittivity, losses, and maximum operating temperatures of common polymer capacitor dielectrics. Permittivity and losses are measured at room temperature.	20
Table 2 - Permittivity, losses, and maximum operating temperatures of P(VDF).	24
Table 3 - Tacticity of P(VDF-CTFE) 81.2/18.8 mol%. Source: Reference 47.	40
Table 4 - Tacticity of P(VDF-TrFE) 81.2/18.8 mol%. Source: Reference 47.	40
Table 5 - Tacticity of P(VDF-CTFE-TrFE) 81.2/7.2/18.8 mol% produced by the two-step synthesis procedure. Source: Reference 47.	42
Table 6 - Tacticity of P(VDF-CTFE-TrFE) 81.0/8.3/10.7 mol% produced by direct polymerization. Source: Reference 47.	43
Table 7 - Transition temperatures and enthalpies for the 79.2 mol% VDF polymers.	47
Table 8 - Crystallinity of hydrogenated polymers.	48
Table 9 - Absolute molecular weights of the P(VDF-CTFE) copolymers.	71
Table 10 - Thermal properties of the P(VDF-CTFE) 78.4-21.6 mol% copolymers.	72
Table 11 - Storage moduli of the P(VDF-CTFE) 78.4-21.6 mol% copolymers.	79
Table 12 - Summarized high strain behavior in the P(VDF-CTFE) 78.4-21.6 mol% copolymers.	81
Table 13 - Summarized predicted breakdown strengths based on the electromechanical model of Equation 20 at 25°C.	85
Table 14 - Summarized predicted breakdown strengths based on the electromechanical model of Equation 20 at -15°C and -35°C.	86
Table 15 - Predicted values for the thermal breakdown strengths for the P(VDF-CTFE) 78.4-21.6 mol% copolymers.	88
Table 16 - Calculated energy densities of the P(VDF-CTFE) 78.4-21.6 mol% copolymers.	91
Table 17 - Crystallinity and crystal phase peaks for the 73.6 mol% VDF polymers.	99
Table 18 - Thermal properties of the 73.6 mol% VDF polymers.	101
Table 19 - Summarized mechanical properties of the 73.6 mol% VDF polymers.	102
Table 20 - Density change between the α , γ , and β crystal unit cells.	106
Table 21 - Experimental and calculated electric breakdown field for the 73.6 mol% VDF polymers.	107
Table 22 - Summarized list of the SiO ₂ - P(VDF-CTFE) hybrids.	120
Table 23 - Thermal properties of the SiO ₂ -P(VDF-CTE) hybrids.	123
Table 24 - Yield stresses and moduli of the SiO ₂ -P(VDF-CTFE) hybrids.	129

LIST OF EQUATIONS

Equation 1 - Definition of capacitance.	4
Equation 2 - Capacitance of a parallel plate capacitor with a vacuum for the dielectric....	4
Equation 3 - Capacitance of a parallel plate capacitor filled with an insulating material. .	4
Equation 4 - Polarization response of a material.	5
Equation 5 - Electric displacement of a material.	5
Equation 6 - Relation of permittivity to dielectric susceptibility.....	6
Equation 7 - Complex permittivity.	7
Equation 8 - Current density in an ideal capacitor under AC conditions.	7
Equation 9 - Conductivity of an ideal capacitor.	7
Equation 10 - Current density in a real capacitor under AC conditions.	8
Equation 11 - Loss tangent.	8
Equation 12 - Energy stored in a capacitor.	9
Equation 13 - Energy stored in a capacitor with a linear dielectric.	10
Equation 14 - Energy density for a linear dielectric material.	24
Equation 15 - Energy dissipation in electronic breakdown.	63
Equation 16 - Thermal breakdown power balance.	64
Equation 17 - Electromechanical stress balance.	65
Equation 18 - Complex modulus.	77
Equation 19 - Weibull probability distribution.	82
Equation 20 - Electromechanical breakdown equation.	83
Equation 21 - Impulse thermal breakdown.	87
Equation 22 - Conductivity of an insulating material.	87
Equation 23 - Electromechanical breakdown criterion.....	104
Equation 24 - Component stresses of the electromechanical stress.....	104
Equation 25 - Electrostatic Maxwell stress.....	104
Equation 26 - Electromechanical stain response.	105
Equation 27 - Electromechanical stress.	105
Equation 28 - Space charge movement by drift and diffusion.....	138
Equation 29 - Initial rise method for calculating the activation energy from TSDC data for an Arrhenius process.	141
Equation 30 - Graphical integration method for calculating the activation energy from TSDC data for an Arrhenius process.	142
Equation 31 - Activation energy for an Arrhenius process.....	142

ACKNOWLEDGEMENTS

I would like to thank my advisor, Professor Qing Wang, for taking me on as a fresh-faced graduate student five years ago to join his newly formed group and helping to build me into the scientist I am today. I also want to thank my group and pseudo-group members Dr. Kun Li, Dr. Yingying Lu, Bret Neese, Siwei Liang, Paisan Khanchaitit, and Jilian Pan for all their help in creating materials, characterizing them, and the helpful discussions for this dissertation. Each one has a unique imprint on this work. I also want to thank my committee members Professors Ralph Colby, Mike Lanagan, and Qiming Zhang who will be the final judges of my worthiness for this degree.

Outside my research, I want to acknowledge all the great friends I have made during my five years in Happy Valley and the support they provided me. My path through graduate school was quite bumpy at times and they were always there when I needed them no matter the time or place. I wish I could mention everyone, but the list would be too numerous and I would feel awful for leaving anyone out.

My family deserves special attention for all their support to this point in my life and through the many challenges I will face in the future. Nothing was ever easy growing up and we faced challenges around every corner. But due to this, I learned how to cope and became that much stronger.

Lastly, I've lost quite a few loved ones in recent years and sincerely wish you were all still here to see this accomplishment. I love and miss you all.

CHAPTER 1 - INTRODUCTION

Historical Background

The history of the capacitor began in the 18th century with the discovery of the first devices capable of storing electric charge. Two men are associated with this discovery.^{1,2} The first was E. Georg von Kleist, a Bishop of Pomerania who was seeking a way to trap and store electrical charge. He developed a device in 1745 and performed many experiments to verify the device's charge storing capabilities. Von Kleist shared his experiments with several colleagues of the era, but did not receive much attention for his discovery due his low stature in the scientific community and the difficulty in others repeating his results.³ A few months after Von Kleist, a similar charge storing device was developed independently by Pieter van Musschenbroek, a known physicist and mathematician who lived in Leyden, Netherlands and is generally recognized as the inventor of the first capacitor. The device was called an electrical condenser and later became known as the Leyden jar named after the place of its invention. In its first form, the condenser consisted of a corked glass bottle partially filled with water and a metal wire.^{4,5} The metal wire was partially immersed in the water and passed through the cork at the top of the bottle. The device was charged by holding it in one hand and touching the metal wire to a charge source, typically a friction machine of the time. After removing the wire from the charge source and touching it with the other free hand, the device was discharged through the body often catching the recipient by surprise. In 1747, an improved version of a Leyden jar, shown in Figure 1, was developed by an English physician and scientist named William Watson. Watson removed the water from the

earlier designs and instead wrapped the inside and outside of the bottle with separate pieces of metal foil that didn't connect. This design greatly enhanced the charge storing properties of the Leyden jar and most closely resembles the construction of modern day capacitors.



Figure 1 - Leyden jar. Note the foil covering and chain electrode inside the jar. Source: Reference 4.

The Leyden jar was a huge advancement in the study of electricity. Previous to its invention, small sparks a few centimeters long could be generated by friction machines of the time. By using a Leyden jar to capture and store the charge generated by a friction machine, it was possible to significantly increase the length of sparks from centimeters to tens of centimeters long. Where a friction machine could send a small jolt through a person, the incorporation of Leyden jars allowed scientists to kill small animals. Additionally, Leyden jars were connected in parallel creating what was called Leyden jar batteries to further increase the devices charge storage. The jars were instrumental in many experiments of the time such as establishing the electrical properties of conductors and insulators, and were used in Benjamin Franklin's famous kite flying experiment. They were also used as effective fundraising sources for experiments by entertaining nobility and other people of power.⁶ In one particular

demonstration, a Leyden jar was discharged in a demonstration to King Louis XV of France sending a shock through a chain of 180 soldiers.

In the years after its discovery, the scientists of the day began to have insight into the fundamental operating principles of the Leyden jars and laid the foundation for understanding capacitors. Early designers of Leyden jar batteries recognized the effect of surface area on charge storage preferring to use many small jars instead of fewer large jars to increase capacity. They recognized the use of thinner glass increased capacity over thick glass and improved reliability. In a capacitor designed by Æpinus, he demonstrated inductive charging and its relation to gap distance. Benjamin Franklin demonstrated that the charge in a Leyden jar was not stored in the metal foil, but in fact stored in the glass illustrating the effect of the dielectric material. He accomplished this by carefully removing the metal foil from a charged Leyden jar and observing that the built-up charge was not removed with the foil. Each of these observations was the basis of a sub-area in capacitor research and since has blossomed in the huge field that we have today.

Capacitor Fundamentals

Capacitors are simple electronic devices typically consisting of two, non-contacting metal electrodes separated by an insulating material. By applying a voltage bias to the electrodes, an electrical field is applied across the insulating material. Charge accumulates on the metal electrodes until the voltage across the gap balances the applied bias. The capacitance of a capacitor is defined as

$$C = \frac{q}{V}$$

Equation 1 - Definition of capacitance.

where C is the capacitance, q is the total charge, and V is the voltage. In the absence of a dielectric material with a vacuum between the electrodes, the capacitance of a capacitor with parallel electrodes is

$$C = \epsilon_0 \frac{A}{d}$$

Equation 2 - Capacitance of a parallel plate capacitor with a vacuum for the dielectric.

where ϵ_0 is the permittivity of free space, A is the area of the electrodes, and d is the distance between the electrodes. If an insulating dielectric material is placed between the electrodes, an increase in capacitance is observed over an empty capacitor under the same voltage bias and is represented by

$$C = \epsilon \epsilon_0 \frac{A}{d}$$

Equation 3 - Capacitance of a parallel plate capacitor filled with an insulating material.

where ϵ is the permittivity of the dielectric material. Figure 2 illustrates the difference between an empty and filled capacitor. The higher capacitance stems from an increase in charge, q , on the electrodes that originates with the dielectric material. Under a bias, the dielectric experiences a polarization that attempts to decrease the applied electric field passing through the material by setting up an opposing one. To compensate for the polarization, more charge accumulates on the electrodes until the circuit is balanced. The

polarization vector has the opposite sign convention for electric field that emerges from negative charges and terminates on positive ones. The polarization is defined by

$$P = \epsilon_0 E (\epsilon - 1)$$

Equation 4 - Polarization response of a material.

where P is the polarization and E is the electric field.⁷ Equation 4 can be rearranged to create a new term called the electric displacement

$$D = \epsilon_0 E + P$$

Equation 5 - Electric displacement of a material.

where D is the electric displacement. The electric displacement is simply the sum of the polarization obtained from an empty capacitor plus the dielectric material and represents the total charge on the electrodes.

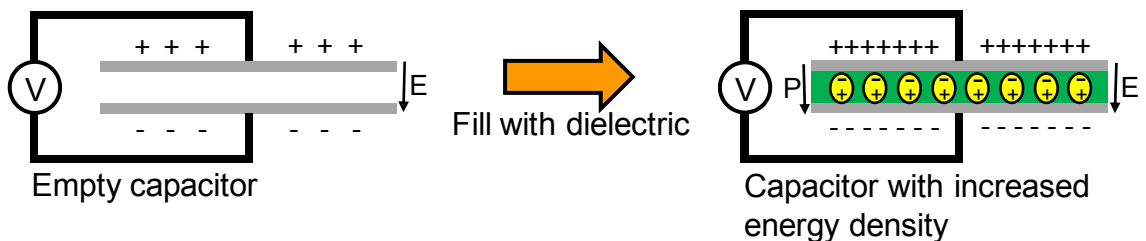


Figure 2 - Increase in capacitance upon filling a capacitor with a dielectric.

The origins of the polarization responses varies between materials. There are five polarization responses: electronic, ionic, dipolar, ferroelectric, and interfacial.^{7,8}

Electronic polarization is present in all materials and originates from the relative displacement of the electron cloud and nucleus on the atomic level. Under an applied electric field, the electron cloud and nucleus are displaced from their equilibrium position creating the polarization. Ionic polarization is present in ionic materials like salts and

ceramics. This polarization mechanism originates from the displacement of positive and negative ions from their equilibrium positions under bias. Dipolar polarization originates from the rotation of permanent dipoles usually present in organic materials under electrical bias. Ferroelectric polarization is unique to ferroelectric materials which have crystals with permanent dipoles. Under bias, polarization can originate from either ferroelectric domain wall motion in the crystals or rotation of the crystals themselves depending on the material. Finally, interfacial polarization originates from the long range motion of charged species that accumulate at interfaces in the materials such as crystalline-amorphous, grain, and phase boundaries. These individual contributions are all additive to the permittivity and can be represented by

$$\varepsilon = 1 + \frac{P}{\varepsilon_0 E} = 1 + \chi$$

Equation 6 - Relation of permittivity to dielectric susceptibility.

where χ is the dielectric susceptibility. The dielectric susceptibility contains all of the contributing polarization mechanisms which can be separated through appropriate experimentation.

The permittivity of a material is a function of frequency of the applied electric field and the electric field strength. Each polarization mechanism has its own individual frequency response that is additive to the overall permittivity. As the frequency of the field is increased, each polarization mechanism drops out as the frequency passes the response time of that mechanism. Eventually at high enough frequencies, all of the polarization mechanisms drop out and have no contribution to the permittivity with the capacitor behaving as though it was empty.

Under alternating current (AC) conditions, the complex permittivity is defined as

$$\epsilon_c = \epsilon' - i\epsilon''$$

Equation 7 - Complex permittivity.

where ϵ_c is the complex permittivity, ϵ' is the real part of the complex permittivity, and ϵ'' is the imaginary part of the complex permittivity. The real part, or ϵ' , is what is traditionally referred to as the dielectric constant and has been defined as the permittivity (ϵ) so far and will continue to be referred to as such. The dielectric constant is defined by the real part of the permittivity measured at low frequency and electric field where this quantity has little variation. The imaginary part of the permittivity, ϵ'' , is related to the loss in the dielectric and will be discussed later. In a perfect capacitor where the polarization responds in phase to the applied electric field, the current density can be defined as

$$J = \frac{dP}{dt} = -i\omega\epsilon_0(\epsilon - 1)E_0e^{-i\omega t} \text{ where the applied field is } E = E_0e^{-i\omega t}$$

Equation 8 - Current density in an ideal capacitor under AC conditions.

where J is the current density, ω is the frequency, ϵ is the material permittivity, and t is time. Dividing the current density by the electric field produces the equation

$$\frac{J}{E} = -i\omega\epsilon_0(\epsilon - 1)$$

Equation 9 - Conductivity of an ideal capacitor.

which defines the conductivity of the capacitor. For a perfect capacitor, there is no power loss in the dielectric since the integration of the product J and E over one period is always

zero. This is due to fact that the current and electric field are always $\pi/2$ out of phase from each other.

In a real dielectric, the current and electric field are almost never $\pi/2$ out of phase resulting in a power loss in the dielectric. In this case, the current density of the capacitor is

$$J = \frac{dP}{dt} = -i\omega\epsilon_0(\epsilon - 1)E_0 e^{-i\omega(t-\delta)}$$

where the applied field is $E = E_0 e^{-i\omega t}$

Equation 10 - Current density in a real capacitor under AC conditions.

where δ is a time delay.⁹ The delay in the current response originates from the response times for the individual polarization mechanisms. Interfacial and dipolar polarization both usually have long response times. For interfacial polarization the long times are usually due to the size of the charged species and the large distances they move. The long times for dipolar polarization are due to the slow orientation of large dipoles. Response times for interfacial and dipolar polarization in general can extend to the hertz and megahertz range respectively. Ionic and electronic polarization mechanisms both have smaller response times due to the small ions, electrons, and atomic nuclei being displaced and their small displacements. Response times for ionic and electronics polarization mechanisms approximately extend to 10^{12} Hz and 10^{16} Hz respectively. The loss in capacitor is usually reported as the loss tangent defined as

$$\tan \delta = \frac{\epsilon''}{\epsilon'}$$

Equation 11 - Loss tangent.

and usually reaches a local maximum near the maximum response times of the polarization mechanisms. Figure 3 illustrates the frequency response of the various polarization mechanisms for both ϵ' and ϵ'' . The loss of a capacitor plays a tremendous role in judging a dielectric's worthiness. A dielectric with a high loss leads to a large conductivity which is not desirable.

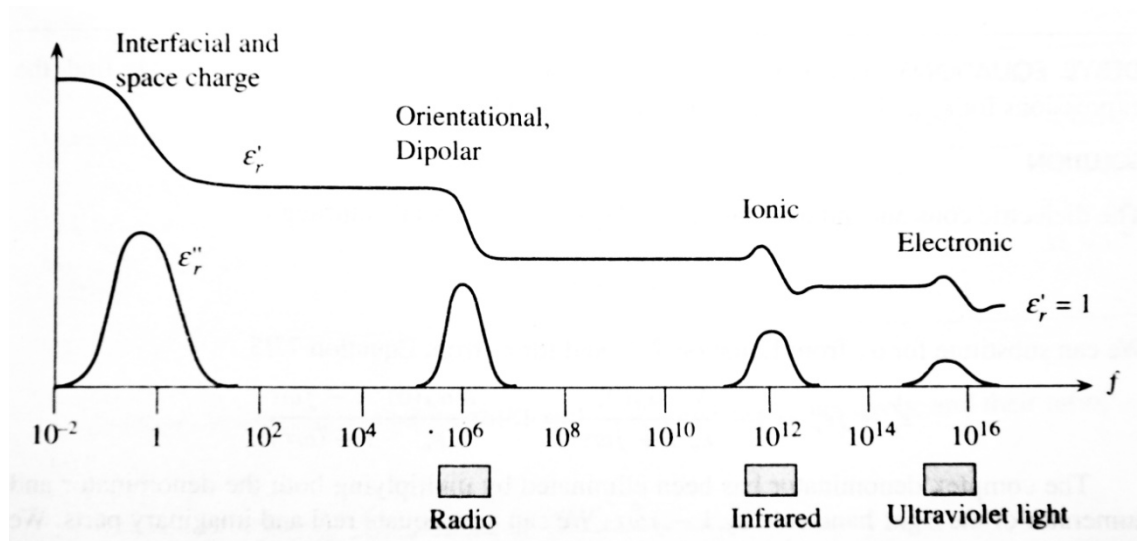


Figure 3 - Frequency response of the various polarization mechanisms. Source: Reference 8.

Along with the loss, the energy stored in a capacitor is another important metric for performance and is defined as

$$du = Vdq$$

Equation 12 - Energy stored in a capacitor.

where u is the energy stored in the dielectric.¹⁰ For a linear dielectric material, or a material whose permittivity is constant at all electric field strengths, the energy in a capacitor is

$$u = \frac{1}{2} CV^2$$

Equation 13 - Energy stored in a capacitor with a linear dielectric.

where it is a function of both the capacitance and the voltage. Energy can be increased by increasing capacitance through a higher permittivity material. Energy can also be increased by applying a higher voltage giving each individual charge the ability to do more work.

Review of Capacitor Technology

Electrical Double Layer Capacitors

Electrical double layer (EDL) capacitors go by several different names such as ultracapacitors and supercapacitors, but all refer to capacitors that use an EDL as an energy storage mechanism.^{11,12,13} The name EDL capacitors are also used to define hybrid EDL capacitors that use an EDL along with a redox process to store energy, but still display a linear dependence of charge on voltage characteristic of a capacitor. The structure of this family of capacitors relies on the use of high surface area, conductive electrodes immersed in an electrolyte media. Upon the application of a bias between the electrodes, the respective counter ions in the electrolyte diffuse to the appropriate electrode creating an EDL on each electrode. Strictly speaking, there is no flow of charge between the electrodes and electrolyte, but this rule is bent in some hybrid EDL capacitors. The dielectric in these capacitors is the thin, atomic monolayer of ions that is adsorbed to the electrode surface while the diffuse electrolyte layer outside of the monolayer is the counter electrode as shown in Figure 4. The voltage drop across the diffuse layer is very small compared to the EDL. Figure 4 also shows the geometry of a

typical EDL capacitor. The conductive electrodes are attached to metallic current collectors which are used for the application of voltage. A porous separator is used to prevent short circuiting between the electrodes while permitting the diffusion of electrolyte.

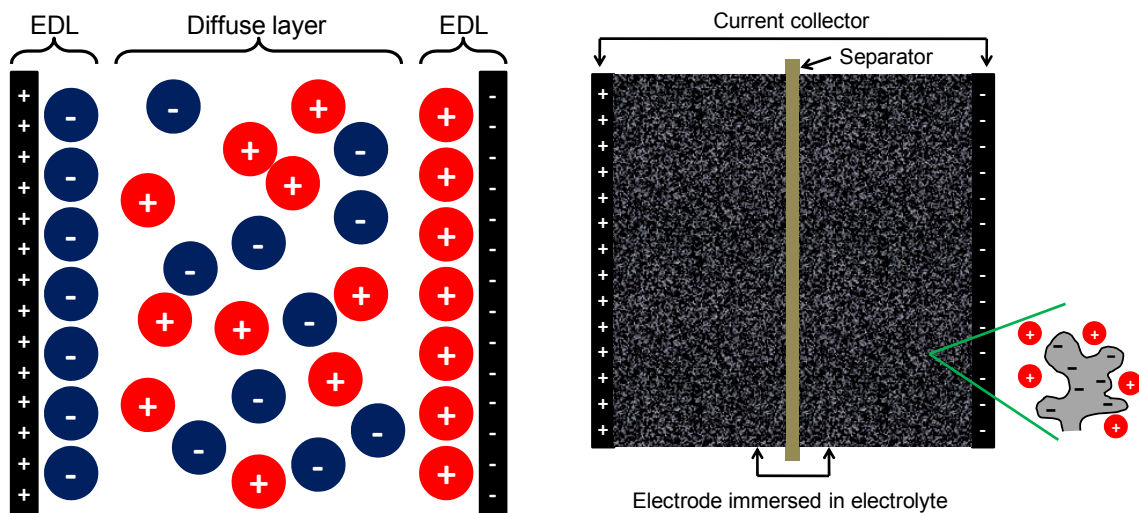


Figure 4 - Left: Schematic of EDL and diffuse layers. Right: Geometry of EDL capacitor.

In terms of energy density, EDL capacitors are unrivaled by the other capacitor technologies. This originates from the large surface areas that are available from the electrode materials. Typically, porous carbons are used which have surface areas up to $2500 \text{ m}^2/\text{g}$ making devices with high capacitances in the hundreds and thousands of farads accessible.¹¹ However, EDL capacitors also suffer from several drawbacks that have limited their wide spread adoption. The first is that they have limited operating voltages. Aqueous based electrolytes will dissociate at voltages above one volt while most organic based solvents are limited to two or three volts before dissociation. As shown in Equation 13, the low voltage limits the energy stored. The second drawback is the limited power density. While energy density can be very high, the power density or

the rate at which the energy can be stored and extracted is limited due the slow response times associated with the combined dipolar and interfacial polarization mechanisms. The maximum frequency response of EDL capacitors is usually below the kilohertz range. Third, loss in the capacitors can be significant due to an equivalent series resistance (ESR). EDL capacitors can be modeled according to the circuit diagram shown in Figure 5 as two capacitors in series with a resistor between them.¹² The capacitors in series reduces the overall capacitance of the device while the resistor represents the resistance of the electrolyte. Aqueous electrolytes have an order of magnitude lower resistivities than organic electrolytes.¹¹ The ESR plays an important role when assembling high voltage devices which requires many capacitors to be wired in series. In this configuration, abnormal behavior from one capacitor will disrupt the performance of the entire device.

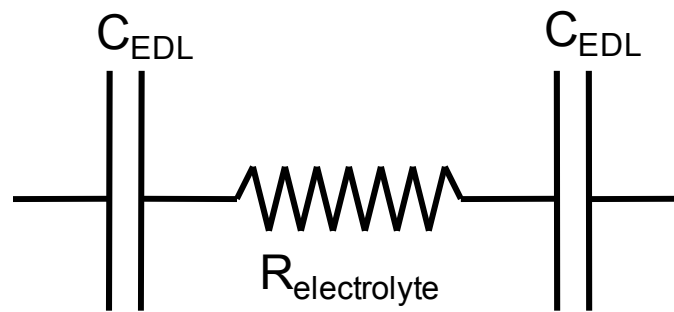


Figure 5 - Equivalent circuit of EDL capacitor.

The EDL is basis of the charge storage and has a complicated and not completely understood structure. The most basic model of the EDL is based on Helmholtz's model, similar to Figure 4, and consists of an adsorption of ions to the electrode surface creating a two dimensional monolayer. A more complex model that approaches reality proposed by Grahame and shown in Figure 6 shows the several layers of ions that make of the

EDL.¹³ Grahame's model incorporates the volume effects associated with hydrated ions and their packing density on a charged surface as well as an outer diffuse layer of ions that are weakly associated with the surface. Figure 6 specifically shows a monolayer of hydrated cations adsorbed to the anode. This three dimensional model of the EDL incorporates the capacitive contributions from various layers. A simple calculation of the permittivity of the double layer at the anode electrode in aqueous solution yields value of ~ 6 which is well below the bulk permittivity value of water at 78. The low permittivity calculated implies a saturation before maximum polarization is achieved in the monolayer possibly associated with the bulk of hydrated cations and imperfect layer packing despite the high electric fields of $\sim 10^6$ V/m across the layer. On the cathode side, a permittivity value of roughly double the anode is calculated due to better packing of smaller anions. Pore size and shape on the electrodes also plays a role in EDL packing by restricting large ions from accessing some surfaces.

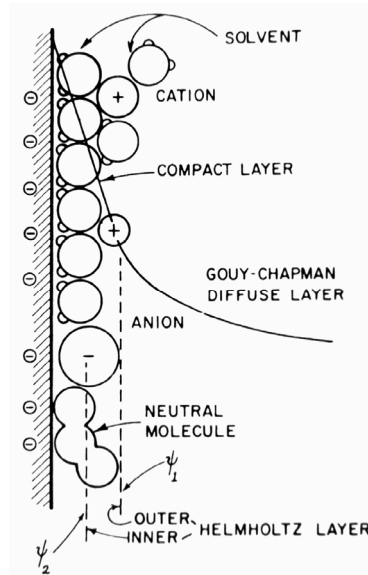


Figure 6 - Grahame's model of the EDL interface. Source: Reference 13.

Applications for EDL capacitors reside in areas where they can be used in conjunction with or as replacements for batteries.¹¹ While EDL capacitors don't have the energy density of batteries, they have superior power densities and cycle lifetimes. The high power densities make them attractive for energy re-capture applications such as regenerative braking systems and certain pulse power applications such as engine starting. The high cycle lifetimes, typically on the order of 10^5 to 10^6 , make them attractive for solar energy storage applications where energy captured during daylight can be stored for later use. Efforts are ongoing at increasing the energy density of EDL capacitors by exploring pseudo-capacitance phenomenon in electrodes made from Ruthenium and conjugated polymers that combine the EDL effects with redox reactions. Devices based on this phenomenon combine the fundamental behavior of both capacitors and batteries to create a hybrid device that still retain capacitor-like behavior.

Electrolytic Capacitors

Electrolytic capacitors offer a good combination of energy and power densities. The first patent issued for electrolytic capacitors was in 1897 by Pollack for use with aluminum followed by a patent for tantalum in 1949.¹⁴ The dielectrics in these capacitors are a thin, electrolytically grown metal-oxide film. Construction of these capacitors typically begins with two metal foils which are etched to increase their surface area.¹⁵ A metal-oxide film is grown on one of the foils while the other is left bare. Alternatively wire electrodes and porous, sintered powder electrodes are also used for metal oxide formation. The etching and use of powders can increase the surface area of the electrodes by a factor of 20 for higher capacitances.¹⁶ The two foils are then laid on top of one another and filled with an electrolyte as shown in Figure 7. The thickness of the

electrolytic metal oxide is about 100 nanometers. In these devices, the electrolyte can be thought of as the counter electrode as oppose to the bare metal foil. Aluminum and tantalum are the most popular choices for growing the metal oxide films, though other metals and their oxides such as niobium, zirconium, tungsten, and titanium have been investigated for electrolytic capacitors. Aluminum oxide has a permittivity of ~ 8.5 while tantalum pentoxide's permittivity is higher at ~ 28 . Aluminum capacitors contain a liquid electrolyte while tantalum capacitors can contain either a liquid or solid electrolyte. The solid electrolyte is typically the n-type semiconductor manganese dioxide that is deposited through a pyrolysis process.¹⁷

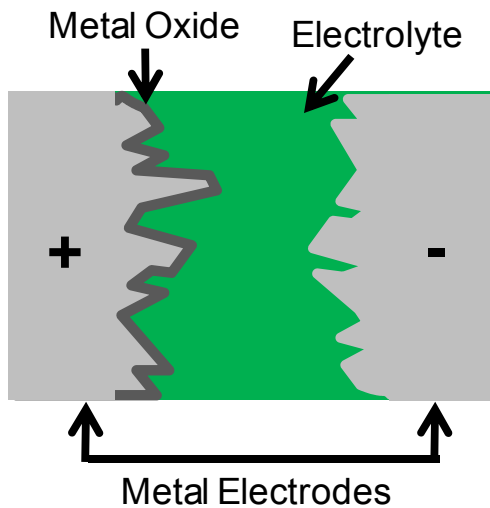


Figure 7 - Construction of an electrolytic capacitor.

Within the metal oxide dielectric, polarization is due to ionic and electronic mechanisms. Outside the metal oxide, an electrostatic and EDL contribute to the polarization. The presence of the EDL limits the frequency response of these capacitors to below ten kilohertz, roughly a decade of response better than just an EDL capacitor because of the added electrostatic polarization.⁸ Unique to electrolytic capacitors is that

they must be used in a certain polarity due to the possibility of degradation of the metal-oxide film to the original metal under a sufficiently high reverse bias. This limits some high field AC applications since the high voltage swings would cause the capacitor to leak on each half cycle. But this damage, if minor, can be repaired through a sufficiently high forward bias to re-grow the weak points in the oxide. Electrolytic capacitors also have some retifying properties because of the metal to metal-oxide interface. The metal oxide formed in the electrolysis reaction is high quality and purity and in the case of aluminum oxide can withstand electric fields on the order of 10^9 V/m.⁸ High purity metal foils greater than 99.99% are required to grow metal-oxide film with these properties.

Applications for electrolytic capacitors are widespread due to their low-cost and reasonable energy and power densities. Aluminum devices represent the bulk of the market while tantalum devices are restricted to applications where high capacitance, temperature stability, reliability, and/or longevity are required. While aluminum is a widely available metal, tantalum is rare in comparison making these capacitors more expensive. Additionally, tantalum devices are preferred for use with solid electrolytes for applications where electrolyte leakage may be an issue. Low voltage examples where electrolytic capacitors are used are in printed circuits and other micro electronics. High voltage examples requiring high power delivery include audio equipment and camera flashes.

Ceramic Capacitors

Ceramic capacitors can be split into two categories of low and high permittivity dielectrics. Low permittivity ceramics range from 15-500 with high permittivity materials ranging from 2000 to 20000.¹⁶ Examples of low and high permittivity ceramics

are titania and barium titanate respectively.^{16,18} The construction of a ceramic capacitor is typically in a parallel plate configuration with electrodes attached directly to the dielectric. In order to improve the capacitance density, ceramic capacitors are sometimes formed into multilayers with alternating dielectric and electrode layers. Hollow tubular shapes are also produced with electrodes on the inner and outer surfaces. Figure 8 illustrates the different geometries used. The dielectrics are produced starting with powders of the dielectric materials which are mixed with 5 -10 % by volume of an organic binder, typically a polymer. The starting powders are made from milled, pure dielectric materials or particles made from a synthetic chemical route. Once combined with the binder, the resulting slurry can be extruded to the various shapes. The organic binder material is burned out at a high temperature above the decomposition temperature of the binder followed by a sintering step at even higher temperature to reduce the porosity of the final piece and increase its density. Isostatic pressure at high temperature may also be used to this purpose. The final capacitor is encapsulated in a polymer, usually an epoxy resin, to prevent the infiltration of water into the device.⁸

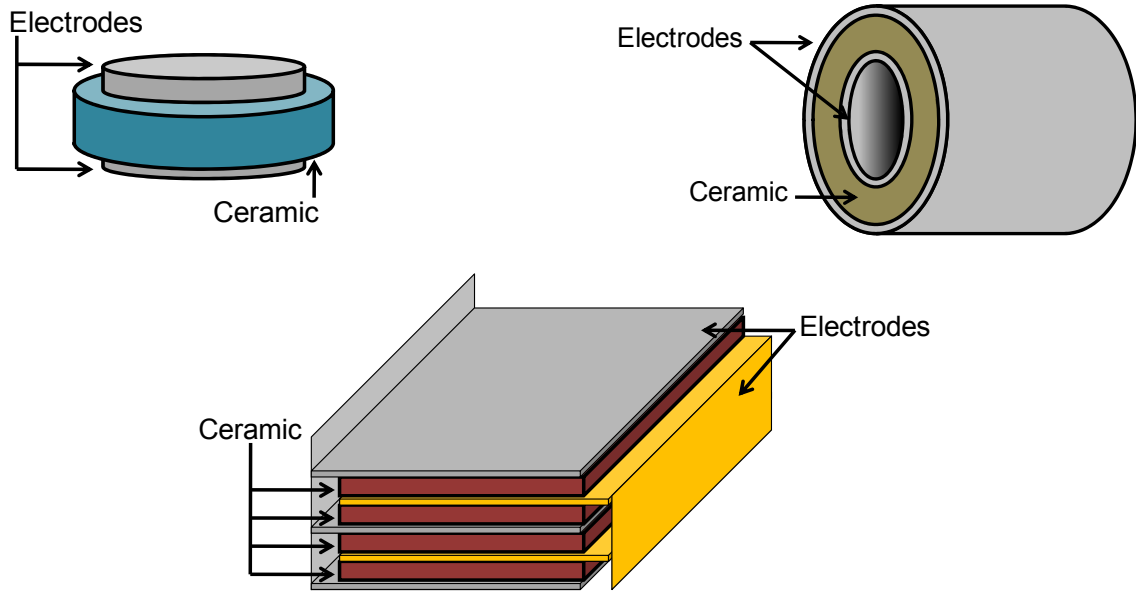


Figure 8 - Top left: Disk capacitor. Top right: Tube capacitor. Bottom: Multilayer capacitor.

Polarization in ceramic capacitors can originate from three sources and is solely an electrostatic device. In all ceramic dielectric materials, polarization comes from ionic and electronic mechanisms. In high permittivity materials, the polarization also has a ferroelectric contribution which increases the permittivity up to three orders of magnitude. Low permittivity ceramics have frequency responses into the gigahertz range while high permittivity materials only go up to the megahertz range before the ferroelectric contribution falls off. Most ceramic dielectrics have low losses due to their polarization mechanisms. These losses can increase as the ceramic degrades by water contamination, and the migration of oxygen vacancies and metal ion contaminants from electrodes through grains and grain boundaries. Degradation can be reduced by the incorporation of dopants that reduce oxygen vacancies and by proper encapsulation to prevent water based side reactions. Most ceramics capacitors have a wide operating temperature region due to the stability of the ceramic dielectric and its electrical

properties. This is not the case for high permittivity materials where the ferroelectric materials experience a Curie transition above which the material becomes paraelectric and the permittivity drops significantly. Ferroelectric materials also suffer from an aging effect where the permittivity will drift due to restrictions on the ferroelectric domain wall motion from defect build up at the boundaries.¹⁹ Heating above the Curie temperature usually reverses this phenomenon.

Applications for ceramic capacitors span a wide range. While energy densities of the capacitors may not be very high being limited by the breakdown field, ceramics do have very high power densities. Ceramic capacitors find use in high power transmitter capacitors and are especially useful for their low losses and negative temperature coefficients of permittivity which limit thermal runaway. They also find a lot of use in microelectronics where low loss, temperature stability, and withstanding high voltages are important design features.

Polymer Capacitors

Polymer capacitors are all based on thin films of polymer dielectrics usually less than 10 microns thick. Films are created from extrusion, solution casting, or evaporation deposition.²⁰ The permittivity of most polymers used in capacitor applications are small compared to the previously mentioned dielectrics ranging from 2.2 to 3.5.^{21,22,23,24} The most common polymers are listed in Table 1. Polymer capacitors are constructed in a parallel plate configuration with metal electrodes in contact with the dielectric. Evaporated aluminum is often the metal of choice, though metal foils or other evaporated or sputtered metals are also used. Occasionally, a double metalized polymer is used as an electrode where the polymer is not active in the actual capacitor. An example of this is

shown in Figure 9.²⁵ The application of the capacitor usually dictates the type of electrode. Since polymers are very flexible, they are typically rolled into cylinder configurations in actual devices. The rolled, metalized polymer films are inserted in cylindrical containers which are occasionally backfilled with insulating oils to reduce electrical discharge and improve heat dissipation.

Polymer	ϵ'	$\tan \delta$	T_{\max} (°C)
Polystyrene	2.8	0.00026	85
Polyimide	3.6	0.00200	200
Polypropylene	2.2	0.00042	105
Polyester	3.5	0.00170	125
Polycarbonate	2.9	0.00097	125
Polyphenylene-sulfide	3.0	0.00030	200
Polyphenylene oxide	2.6	0.00030	
Polyether etherketone	3.0	0.00350	240
Polytetrafluoroethylene	2.1	0.00020	260
Poly ethylene 2,6 naphthalate	3.2	0.00300	140

Table 1 - Permittivity, losses, and maximum operating temperatures of common polymer capacitor dielectrics. Permittivity and losses are measured at room temperature.

Polarization in polymers typically results from electronic and dipolar mechanisms. Ferroelectric polarization is also possible for some polymers which can increase the permittivity an order of magnitude. Outside of the ferroelectric polymers, the frequency responses of the dielectrics usually extend to the gigahertz range with low losses. Ferroelectric polymers have higher losses and only have frequency responses into the megahertz region. Permittivity and losses can be stable with temperature as long as no thermal transitions are approached. This is not the case for ferroelectric polymers which experience fluctuations around the Curie transition. The operating temperature range of polymers is fairly low compared to some ceramics due to low temperature thermal transitions.²⁶ The maximum operating temperatures are often around 100°C with

specialty polymers going to 200°C. One unique feature of metalized polymer films is a self-healing mechanism that occurs during electrical breakdown. In other capacitors electrical breakdown usually results in a short, or the creation of a conducting path between the electrodes, in the capacitor rendering the device useless. The self-healing mechanism during electrical breakdown causes a portion of the metalized film to evaporate around the failure point from the heat generated during breakdown. While a short may exist across the dielectric, it doesn't affect the rest of the device since it is isolated electrically. Many different factors affect self-healing such as polymer chemistry, applied voltage, electrode thickness, and pressure.²² Self-healing provides a mechanism for monitoring the lifetime of the capacitor through the capacitance decay with every event. Self-healing also reduces the need for extremely high quality films since defects are automatically cleared, though fewer defects would increase the lifetime of the devices. Power densities are very high in polymers, but energy densities are fairly low. The energy density values are similar to ceramic capacitors though ceramics rely on high permittivities or capacitances while polymers high voltages and dielectric strengths to achieve these values.

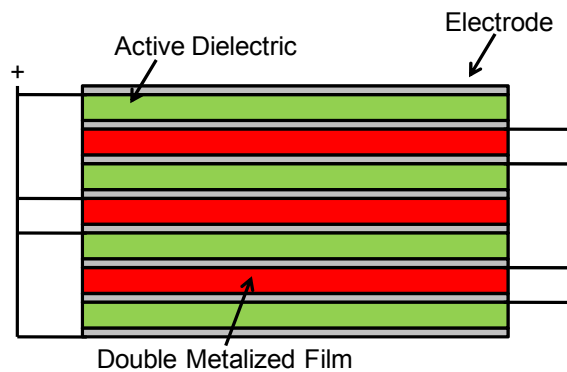


Figure 9 - Double metalized polymer layer structure.

The application of the polymer capacitor dictates the choice of the dielectric.²³ Polyester is used in applications where high capacitance densities are needed and loss drift with temperature and frequency is not an issue. Polycarbonate is used for higher temperature applications where higher losses are tolerable. Polypropylene, the most popular polymer due to excellent properties and low cost, has a reasonable upper temperature limit of 90°C and flat permittivity and loss with varying temperature and frequency. Specialty polymer dielectrics include polystyrene for its low loss and poly(phenylene sulfide), polyimide, and poly(tetra fluoride) for their high operating temperatures. Polymer capacitors find much use in pulse power applications since large capacitors can be fabricated with ease and the self-healing mechanism give long lifetimes.

Research Goals

Polymers are important capacitor dielectric materials and will continue to be so well into the future. In power applications, polymers are often the materials of choice for many reasons including low cost and ease of manufacturing. However, the demands for increased performance from polymer dielectrics have prompted recent research into searching for new polymers. For power applications, the ideal dielectric material must have a high power and energy density, low electrical loss, and good reliability. A Ragone plot illustrating the various energy storage technologies is shown in Figure 10.²⁷ The performance of 'Film Caps' in the figure can describe both ceramic and polymer dielectrics. No single storage technology covers the entire energy and power ranges necessitating careful selection for the application. The greatest limiting factor to polymer

capacitors is their low energy density which currently tops out at about 1 J/cm^3 for most of the commercially available polymers listed in Table 1.²² The theme to the research presented here is to explore new polymer dielectrics with potential energy densities an order of magnitude higher than the current state of the art. Such an increase in energy density would make polymers competitive with electrolytic and EDL capacitors for some applications.

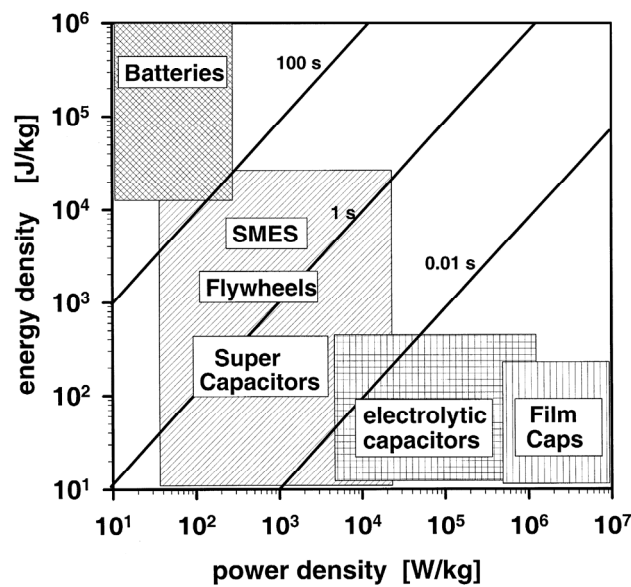


Figure 10 - Ragone plot of energy storage technologies. Source: Reference 27.

This research has three focus points which all revolve around creating new polymer dielectric materials and evaluating their properties. The first point is the synthesis of novel fluoropolymers based on vinylidene fluoride (VDF) as candidate dielectric with high power and energy densities. Copolymers containing VDF were made using a unique synthetic approach allowing for polymers with new compositions and properties to be created. Poly(vinylidene fluoride) (P(VDF)) has been the subject of research for use as a capacitor dielectric due to its high permittivity as shown in Table 2.^{21,22} Contrasted to the polymers shown in Table 1, P(VDF) has a significantly higher

permittivity. As shown in Equation 13, a high capacitance is essential for a high stored energy from the dielectric. The resulting electrical properties such as permittivity, as well as their various thermal and structural characteristics of these novel polymers were characterized in this work.

Polymer	ϵ'	$\tan \delta$	T_{\max} (°C)
Poly(vinylidene fluoride)	11	0.011	125

Table 2 - Permittivity, losses, and maximum operating temperatures of P(VDF).

The second focus point of the research here is to study the electrical breakdown properties of the synthesized polymers. The energy density of a linear dielectric material can be calculated according to

$$U = \frac{1}{2} \epsilon_0 \epsilon E^2$$

Equation 14 - Energy density for a linear dielectric material.

where U is the energy density per volume of the dielectric. The energy density is dependent on the permittivity of the dielectric and the applied electric field to the material. The applied electric field is limited by the electrical breakdown strength of the dielectric or the maximum field that can be applied before catastrophic degradation occurs. Since the energy density is proportional to the square of the electric field, any increase in this value leads to substantial increases in the energy density more so than an increase in permittivity. The electrical breakdown mechanisms of the novel fluoropolymers were studied and related to their thermal, mechanical, electrical, and microstructural properties.

Finally, the third focus point of this research combines the knowledge from the first two points to create a hybrid material of fluoropolymer and silicon dioxide. The hybrid material takes advantage of the properties of the inorganic and organic materials to create a well dispersed composite with promising energy storage results. In the following chapters, each of these focus points will be discussed in more detail and the collected results will be presented for the new polymeric materials.

CHAPTER 2 - SYNTHESIS AND CHARACTERIZATION OF P(VDF) BASED COPOLYMERS

Ferroelectric Fluoropolymer Review

Since the discovery of its piezoelectricity in 1969, poly(vinylidene fluoride) (P(VDF)) has been the subject of intense research to exploit this and its other unique electrical properties.²⁸ Of particular interest to capacitor applications is the high permittivity of P(VDF) which has a value of approximately 11, significantly higher than most polymeric dielectric materials.²¹ The high permittivity of P(VDF) originates from the strong dipole present in the polymer's backbone from the alternating carbon-fluorine and carbon-hydrogen bonds. The dipole moment of this repeat unit is 7.6×10^{-30} Cm or 2.3 Debye.²⁹

The presence of strong intramolecular forces gives P(VDF) its unique crystal structure which features one paraelectric phase and three ferroelectric phases.^{30,31} The presence of ferroelectricity also gives rise to piezoelectricity and pyroelectricity in the polymer. The paraelectric phase of P(VDF) is called the α phase and features alternating trans (T) and gauche (G) bonds, specifically TG^+TG^- where + and - signify left and right twists. The chain conformation and unit cell are presented in Figure 11. This form of P(VDF) is the most common and easily produced through most processing methods. While the overall chain conformation is polar, the arrangement of the dipoles facing each other in the unit cell cancels the overall polarization making it paraelectric.

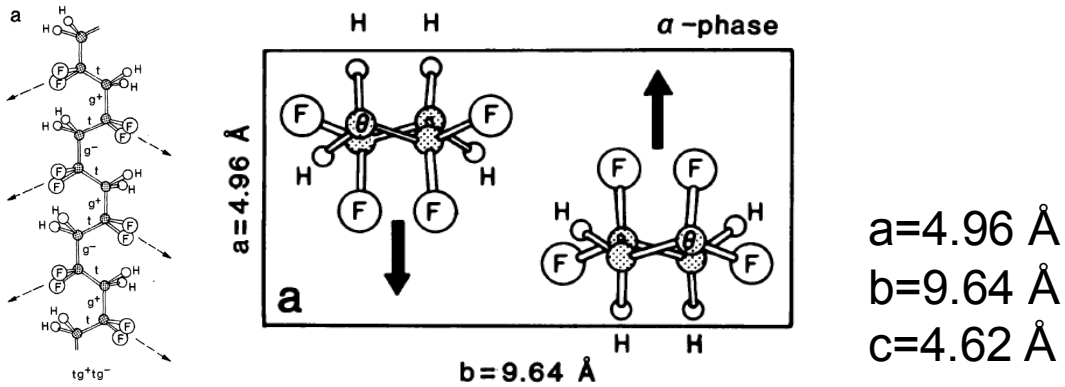


Figure 11 - The α crystal phase of P(VDF). Left: Chain conformation. Right: Unit cell. Source: Reference 30.

The highest polarity unit cell of P(VDF) is the β phase which is shown in Figure 12. The polarity of this unit cell is about twice that of the subsequent polar unit cells.³² The polymer chains are all in the extended, all-trans conformation so that they produce the highest overall chain dipole. The chains are arranged in the unit cell so that the dipole moments all point in the same direction giving rise to a high polarization and its ferroelectricity. The β phase is obtained through mechanical stretching of films containing the α phase, which elongates the polymer chains.

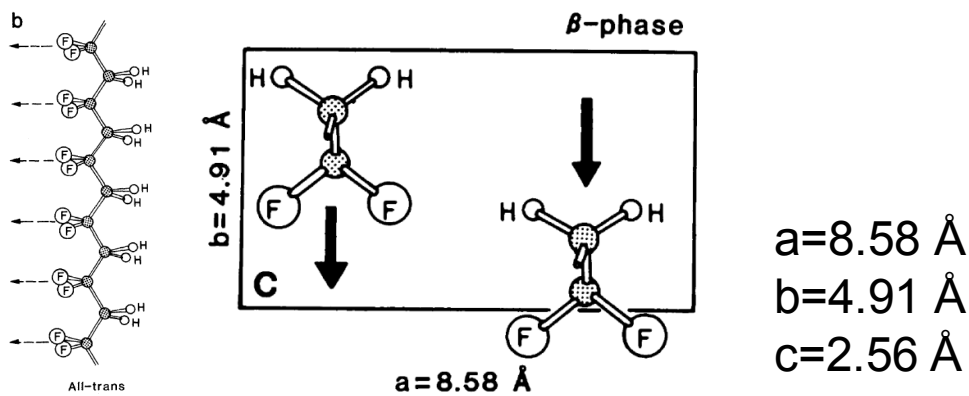


Figure 12 - The strongly polar β crystal phase of P(VDF). Left: Chain conformation. Right: Unit cell. Source: Reference 30.

The γ phase of P(VDF) is also a ferroelectric phase of P(VDF) whose conformation and unit cell are shown in Figure 13. The γ phase features a $\text{TTTG}^+\text{TTTG}^-$ chain conformation resulting in a weaker dipole than the β phase. The chains are arranged with the dipoles pointing in the same direction also giving a ferroelectric unit cell. While the α and β phases of P(VDF) were discovered fairly quickly, it took over a decade of debate before the structure of the γ phase was settled on. The difficulty in identifying the γ phase stemmed from two sources. The first source was the difficulty in producing a sample with a high amount of the crystal phase. The γ phase in P(VDF) is typically made from solution casting from specific organic solvents or crystallizing a melt at high pressure or temperature. However, the γ phase readily transforms to the β phase under mechanical stress necessitating careful handling of the sample. Pure samples of the gamma phase were produced by solution casting onto specific substrates.³³ The second reason for the difficulty in identifying the γ phase lies in its similar x-ray diffraction peaks to the α and β phases. Early reports of the γ were sometimes dismissed as mixtures of the α and β phases. Careful processing and collection of diffraction patterns eventually lead to the confirmation of the γ phase.

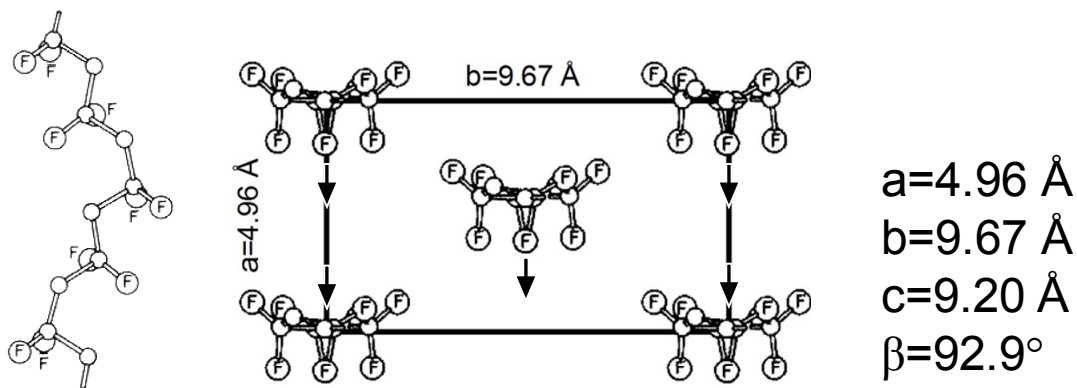


Figure 13 - The γ crystal phase of P(VDF). Left: Chain conformation. Right: Unit cell. Source: Reference 31.

The final phase of P(VDF) is the δ phase. This phase also takes on the TG^+TG^- chain conformation similar to the α phase as shown in Figure 14. In fact, the δ phase has identical diffraction peaks to the α phase, though differing in intensity.³¹ However, the chains in the unit cell of the δ form are arranged with the chain dipoles pointed in the same direction leading to a ferroelectric phase also shown in Figure 14. The δ phase is produced by poling the α phase in a high electric field.

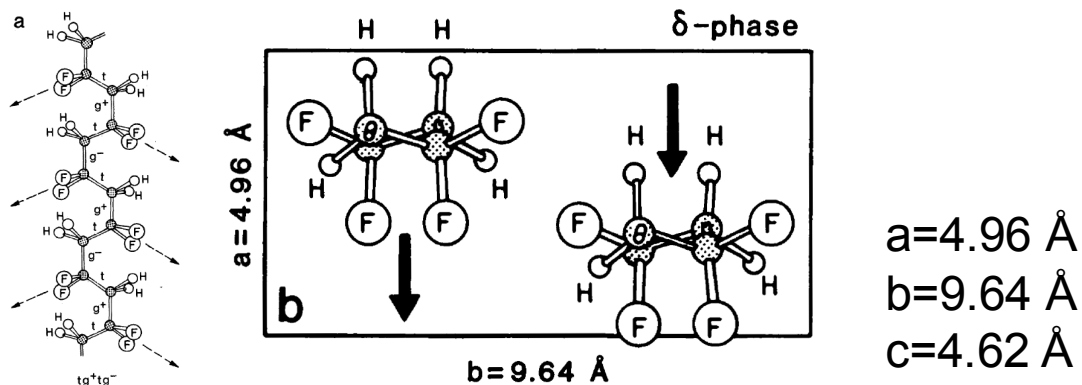


Figure 14 - The δ crystal phase of P(VDF). Left: Chain conformation. Right: Unit cell. Source: Reference 30.

All the interesting electrical properties of P(VDF) arise from its crystal phases and overall crystallinity. The dipoles and ferroelectric phases give it the potential to have a high permittivity from the combined polarization mechanisms. The challenge with P(VDF) is to crystallize the film with the ferroelectric phases and to keep those phases stable. Figure 15 illustrates the phases obtained in P(VDF) from various processing routes.³⁰ When changing between phases, it is often difficult to get a complete conversion resulting in a mixture of phases and resulting properties.

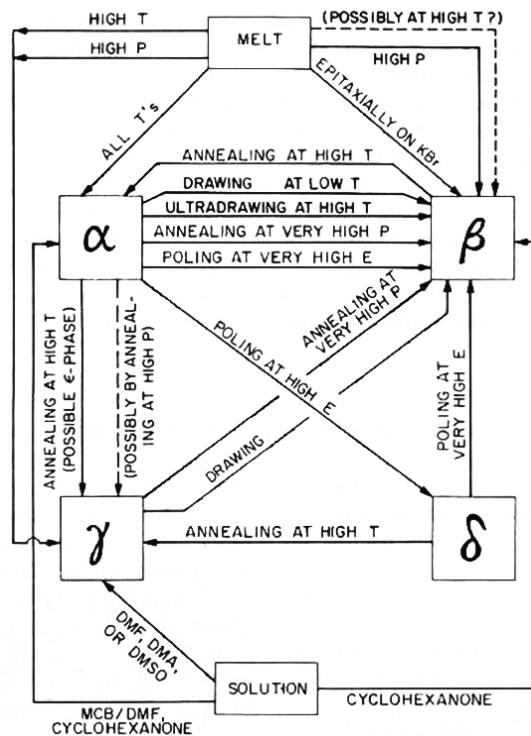


Figure 15 - P(VDF) crystal phases processing routes. Source: Reference 31.

To overcome the conversion limitation, copolymers containing trifluoroethylene (TrFE) were synthesized to examine their spontaneous crystal phases and electrical properties.³⁴ TrFE is virtually identical to VDF except for the substitution of a fluorine for a hydrogen. All ferroelectric materials experience a ferroelectric to paraelectric phase transition at the Curie temperature (T_c) where the material experiences a maximum in permittivity.³⁵ In P(VDF), the T_c occurs above the melting temperature of the polymer so this maximum is never reached. However, the copolymer poly(vinylidene fluoride-trifluoroethylene) (P(VDF-TrFE)) displays a ferroelectric to paraelectric transition at a temperature below the melt depending on the amount of TrFE. The addition of TrFE to the copolymer changes the electrostatic interaction between the monomer units and converts what would normally be an α phase material to one that spontaneously

crystallizes in the ferroelectric β phase. The smallest amount of TrFE needed for this to occur is roughly 22 mol%. At T_c , the phase change converts all the ferroelectric β phase to the paraelectric α phase over a small temperature range. In this temperature window, a large increase in permittivity is observed during the phase switch. Increasing the amount of TrFE in the copolymer above 22 mol% produces a material with a pseudo β phase that is arranged in a hexagonal structure, but still retains ferroelectric properties.³⁶ At a TrFE composition above 48 mol%, the copolymer loses its ferroelectric character and instead crystallizes in a mixture of disordered trans-planar and 3/1 helical phases arranged in a pseudo-hexagonal lattice.³⁷ However as more TrFE is added to the copolymer, a slight Curie transition is still observed in dielectric data down to about 87 mol% TrFE. Diffraction data does not observe this Curie transition behavior of the copolymers containing less than 48 mol% TrFE where below this threshold, the specific β to α phase peaks are not observed. The phase diagram for the ferroelectric-paraelectric transition in P(VDF-TrFE) is shown in Figure 16.³⁸ The observed T_c of the polymers ranges from 70-130°C and the maximum permittivity at T_c ranges from 10-100 depending on composition. The collective research showed that in order to get a high permittivity from P(VDF-TrFE), it is necessary to be around the T_c of the copolymer.

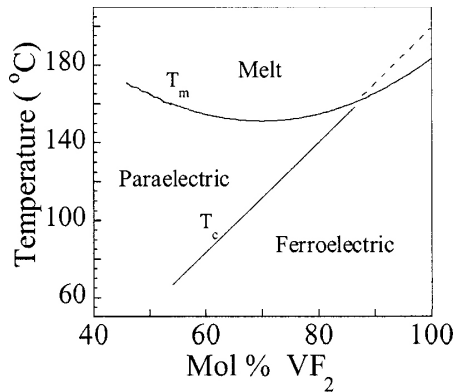


Figure 16 - P(VDF-TrFE) paraelectric-ferroelectric phase diagram. Source: Reference 38.

The next breakthrough in fluoropolymers came in the form of the demonstration of a relaxor ferroelectric in a P(VDF-TrFE) copolymer. P(VDF-TrFE) copolymers display normal ferroelectric behavior featuring large hysteresis loops in electric displacement measurements associated with ferroelectric domain switching.³⁹ Through electron irradiation, the copolymer is transformed into a relaxor ferroelectric material featuring a much slimmer hysteresis loop.⁴⁰ As an additional feature, the irradiation significantly increases the room temperature permittivity of the copolymer from 20 at 1 kHz to over 40 at the same frequency.^{34,40}

Seemingly the T_c of the irradiated copolymer is lowered to around room temperature, but the nature of the Curie transition seen in the irradiated copolymer changes. On a plot of permittivity versus temperature, the irradiated copolymer at first shows a wide range of T_c values as the frequency of the measurement is changed. This is in contrast to the non-irradiated copolymer which shows a narrow range of T_c values associated with a sharp phase transition. Strictly speaking, the relaxor materials do not have a Curie transition like the non-irradiated copolymers. Instead, the T_c for these materials used here refers loosely to the temperature where a maximum in permittivity is

observed. Microstructurally, the irradiation at moderate doses transforms the β phase of the copolymer into a paraelectric-like α phase material.⁴¹ Research performed on relaxor ferroelectric ceramics applied to the irradiated copolymers suggests that the irradiation creates nanosized domains of polar β phase in an α phase like matrix.^{18,40} The β domains are too small to be observed with the x-ray radiation leading to the solely observed α phase. However, upon application of an electric field, this α phase material can be readily transformed back to the β phase suggesting a mechanism for the high dielectric response of the material.⁴²

Interestingly, only ferroelectric P(VDF-TrFE) copolymers experience this change upon irradiation and not the ferroelectric β phase of the homopolymer P(VDF). This is due to the lattice spacing difference between β phase present in the homo and copolymer where the copolymer has a less dense packing between the chains as a result of the steric effects from the additional fluorine. This tighter packing in the homopolymer prevents the solid phase transition from the β to α phase. At high irradiation doses, the copolymers become amorphous due to high levels of crosslinking and chain scission. The irradiation work on the copolymers showed that the introduction of small defects in the polymer crystals changes their morphology and the resulting electrical properties making high permittivities accessible at lower temperatures than the non-irradiated copolymer.

The most recent work in modified P(VDF-TrFE) copolymers is based on introducing defects by chemical means instead of irradiation. This is accomplished through polymer synthesis by the addition of a third monomer to the polymerization resulting in a copolymer containing three monomer units. This is typically referred to as

a terpolymer and will be referred to as such in this dissertation. Several defect monomers have been used, but the most effective have been either chlorofluoroethylene (CFE) or chlorotrifluoroethylene (CTFE).⁴³ All the defects work by introducing bulky atoms to the polymer backbone that hinder the crystal packing. For the monomers mentioned, chlorine is the bulky unit having an atomic radius 170% and 40% bigger than hydrogen and fluorine respectively.⁴⁴ The chemical defect method is superior to the irradiation method in that it does not degrade the polymer by reducing the molecular weight by chain scission helping to maintain the overall mechanical properties. Similarly at high defect concentrations, the terpolymers become amorphous like the high radiation dose irradiated copolymers. In poly(vinylidene fluoride-chlorotrifluoroethylene-trifluoroethylene) (P(VDF-CTFE-TrFE)), high permittivities of 50 have been obtained at room temperature at 1 kHz.⁴³ The crystal structure of the terpolymers is complicated, containing a mixture of the α , β , and now γ crystal phases.⁴³ The γ phase is a signature phase present in most terpolymers. As with the irradiation method, controlling the defect levels in the terpolymers is the key towards optimizing the electrical properties. Additionally, the chemical defect method gives additional parameters for tuning the properties by controlling the amount and type of the defect monomer.

This chapter will focus on the electrical and structural characterization of copolymers created using a unique synthetic procedure. Typically, the ferroelectric copolymers based on VDF are synthesized using a direct method where all the monomers are reacted together.⁴³ While this produces high quality polymers, several difficulties exist with this method that makes it difficult to control the final electrical properties as well

as systematically control the composition. The new procedure described here solves these problems through a two step synthetic process.

Experimental Procedure

Materials

All chemicals were used as purchased without purification unless otherwise noted. Benzoyl peroxide (BPO), 2, 2'-azobis (2-methylpropionitrile) (AIBN), methanol, acetone, N, N-dimethylformamide (DMF), tetrahydrofuran (THF), acetonitrile, hexane, potassium fluoride, and tri-n-butyltin hydride were purchased from Aldrich. Benzoyl peroxide (BPO) was purified by recrystallization from methanol and acetone.

Tetrahydrofuran (THF) was dried and distilled over sodium benzophenone ketyl under nitrogen. Vinylidene fluoride (VDF) and chlorotrifluoroethylene (CTFE) were purchased from SynQuest Laboratory Inc. and purified by a freeze-thaw process.

Solution Polymerization of P(VDF-CTFE) Copolymer (Representative Experiment)

All manipulations of gas-condense transfer were carried out with rigorous exclusion of oxygen and moisture under 10^{-6} Torr high vacuum. A stainless steel autoclave with a magnetic stir bar was charged with 0.12 g of BPO and 30 ml of acetonitrile. The autoclave was cooled in liquid nitrogen and degassed on a vacuum line. 18.4 g of VDF and 7.3 g of CTFE were condensed in the autoclave at liquid nitrogen temperature before being warmed to ambient temperature. The autoclave was then heated for 6 hours at 80°C. After the reaction, the volatiles were vented and the polymer was precipitated in methanol and washed by hexane. After drying under vacuum, 9.4 g

of white powder identified as poly(vinylidene fluoride-chlorotrifluoroethylene) (P(VDF-CTFE)) was obtained.

Hydrogenation Reaction of P(VDF-CTFE) Copolymer (Representative Experiment)

3.0 g of P(VDF-CTFE) copolymer and 171 mg of AIBN were mixed in a 250 mL flask. The flask was attached to a high vacuum line, degassed with argon, and 170 mL of THF was added. After the mixture was stirred at 60°C for 30 min, 1.0 mL of tri-n-butyltin hydride was added by syringe. The solution was kept stirring for 24 hours at 60°C before it was terminated with methanol. The resulting terpolymer of P(VDF-CTFE-TrFE) was washed with hexane and dried in vacuum to get a white powder. Tin byproducts were removed by dissolving the polymers in THF and stirring the solution with aqueous potassium fluoride.

Film Preparation

All polymer films were prepared by solution casting from DMF onto glass slides. Polymers were dissolved overnight in DMF by gentle stirring. The polymer solutions were filtered through 0.45 μm poly(tetrafluoroethylene) syringe filters before casting to remove any particulates. The films were dried at 60°C overnight followed by heating at the same temperature under vacuum for 24 hours for complete solvent removal. Free-standing films were created by soaking coated glass slides in distilled water and carefully peeling off the films. The free-standing films were dried under vacuum for an additional 24 hours to remove any water. The final films were all approximately 20 μm thick.

Characterization

^1H and ^{19}F nuclear magnetic resonance (NMR) spectra were collected on a Bruker AM-300 spectrometer instrument for polymer chemical composition and chain tacticity. Molecular weight relative to a polystyrene standard was measured by size exclusion chromatography (SEC) using THF as the mobile phase with a Waters 1515 isocratic pump. Thermal property measurements by differential scanning calorimetry (DSC) were carried out with a TA Q100 instrument at a heating rate of $10^\circ\text{C}/\text{min}$ using data from second repeats scans. Wide-angle x-ray diffraction (WAXD) studies were performed using a Scintag Cu-K_α diffractometer with a x-ray wavelength of 1.54 \AA . Peak deconvolution was performed using a peak fitting program Pearson VII peaks. Infrared spectra (FTIR) were recorded using a Varian Digilab FTS-800 spectrometer from room temperature to 135°C . Sixty nanometer thick gold electrodes were sputtered onto the films for electrical testing. Dielectric testing was performed using a Hewlett Packard LCR meter (HP 4284A) at room temperature with a 1 V bias. For temperature varying dielectric measurements, the temperature was controlled with a Delta Design Oven model 2300 with liquid nitrogen cooling.

Results and Discussion

Chemical Synthesis of Polymers

The synthetic scheme for the producing the terpolymers is shown in Figure 17. The first step involves the free-radical, solution, polymerization of VDF and CTFE to obtain the copolymer P(VDF-CTFE). The second step involves the selective hydrogenation of the CTFE units in the copolymer to TrFE creating the final terpolymer

P(VDF-CTFE-TrFE). The conversion of the hydrogenation reaction can be precisely controlled from no conversion of the P(VDF-CTFE) to the 100% converted copolymer P(VDF-TrFE).

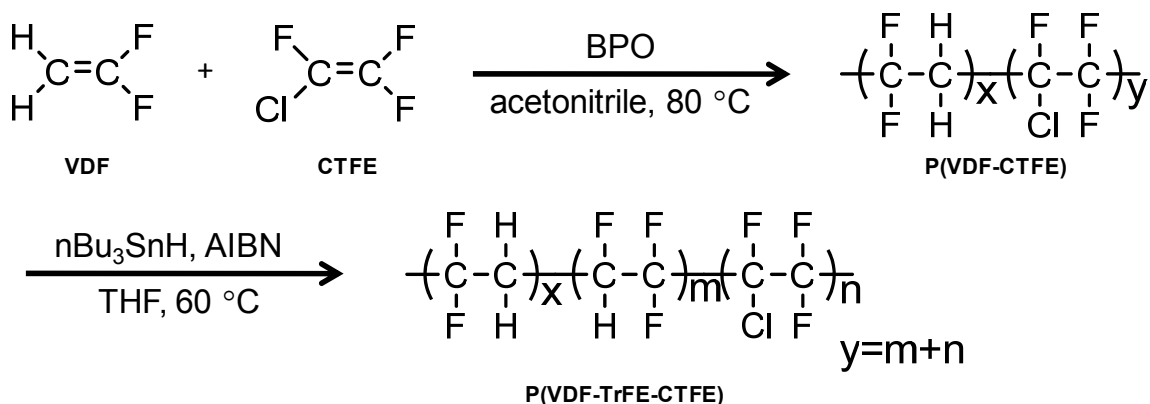


Figure 17 - Two step synthetic scheme for making the terpolymers.

This two step procedure for creating the terpolymer provides a way for systematically producing the terpolymers that is difficult to do using direct polymerization of the three monomers. While VDF and CTFE have similar reactivity ratios of 0.73 and 0.75 respectively, VDF and TrFE have different reactivity ratios of 0.70 and 0.50 respectively.^{45,46} Because of this difference, the consumption of monomers is not constant through the polymerization resulting in a drift in chemical composition as the chains grow. To overcome this problem, direct polymerizations are terminated at low conversions while the ratio of monomers is roughly constant resulting in lower yields. The variability of composition with conversion as well as with feed ratios makes it difficult to systematically synthesize the terpolymers. The two step process used here eliminates many of these problems. Polymerizing VDF and CTFE together ensures a uniform composition through a wide conversion range due to the similarities of their reactivity ratios. The subsequent hydrogenation reaction of the copolymer can be

controlled in a precise manner making composition control easier. Since all the terpolymers for a specific VDF amount are made from the same copolymer, this ensures that the terpolymers all have identical molecular weights and distributions avoiding any potential influence on the electrical properties. The same degree of control over molecular weight would be very difficult with direct polymerization. The two step method for making terpolymers offers the control necessary for systematically studying the polymers as a function of chemical composition.

For this section of work, approximately 50 copolymers of varying chemical composition were synthesized consisting of eight groups of P(VDF-CTFE) copolymers with VDF content ranging from 73.6 to 88.4 mol%. Within each of the groups of eight copolymers, about five terpolymers were made through the hydrogenation procedure which all included the fully hydrogenated P(VDF-TrFE) copolymer. The number average molecular weight for these polymers was approximately 60 kg/mol with a polydispersity index of 1.8.

Polymer Tacticity

¹⁹F NMR results showed that the P(VDF-CTFE) copolymer contains mostly tail to tail tacticity between the VDF and CTFE units.⁴⁷ Table 3 shows the percentage of each tacticity associated with the two monomers and their head to head, head to tail, and tail to tail linkages for a copolymer containing 81.2 mol% VDF and 18.8 mol% CTFE. While the VDF to VDF units are mostly head to head (26.40%), VDF to CTFE exists almost exclusively in tail to tail configurations. A small percentage (0.285%) of VDF to CTFE links are head to tail. These tacticity defects are carried over during the subsequent full hydrogenation reaction to P(VDF-TrFE) as shown in Table 4.

P(VDF-CTFE) 81.2/18.8 mol%		
Sequence	Designation^a	Percentage (%)
-CF ₂ CH ₂ CF ₂ CH ₂ CF ₂ -	VDF-VDF/H-T	26.40
-CFCICH ₂ CF ₂ CH ₂ CF ₂ -	CTFE-VDF/T-T	19.02
-CH ₂ CH ₂ CF ₂ CH ₂ CF ₂ -	VDF-VDF-VDF/T-T-H	6.203
-CF ₂ CFCICF ₂ CFCICF ₂ -	CTFE-CTFE/H-T	3.289
-CF ₂ CH ₂ CF ₂ CF ₂ CFCI-	VDF-CTFE/T-T	12.78
-CF ₂ CFCICF ₂ CFCICH ₂ -	CTFE-CTFE-VDF/H-T-T	2.579
-CF ₂ CH ₂ CF ₂ CF ₂ CH ₂ -	VDF-VDF/T-T	2.275
-CH ₂ CF ₂ CF ₂ CH ₂ CH ₂ -	VDF-VDF/T-T	2.336
-CH ₂ CF ₂ CF ₂ CFCICH ₂ -	VDF-CTFE/T-T	9.922
-CF ₂ CF ₂ CFCICH ₂ CF ₂ -	CTFE-VDF/T-T	10.30
-CF ₂ CH ₂ CF ₂ CFCICF ₂ CH ₂ -	VDF-CTFE-VDF/T-T-H	0.238
-CH ₂ CF ₂ CFCICF ₂ CH ₂ -	VDF-CTFE/H-T	0.285

^a The head (H) is designated as CF₂ while the tail (T) is CH₂ or CFCI

Table 3 - Tacticity of P(VDF-CTFE) 81.2/18.8 mol%. Source: Reference 47.

P(VDF-TrFE) 81.2/18.8 mol%		
Sequence	Designation^a	Percentage (%)
-CF ₂ -CH ₂ -CF ₂ -CH ₂ -CF ₂ -	VDF-VDF / H-T	26.67
-CHF-CH ₂ -CF ₂ -CH ₂ -CF ₂ -	TrFE-VDF / T-T	20.52
-CH ₂ -CH ₂ -CF ₂ -CH ₂ -CF ₂ -	VDF-VDF-VDF / T-T-H	5.118
-CF ₂ -CHF-CF ₂ -CH ₂ -CF ₂ -	VDF-TrFE / H-T	1.224
-CF ₂ -CH ₂ -CF ₂ -CF ₂ -CHF-	VDF-TrFE / T-T	11.67
-CF ₂ -CH ₂ -CF ₂ -CF ₂ -CH ₂ -	VDF-VDF / T-T	1.998
-CH ₂ -CF ₂ -CF ₂ -CH ₂ -CH ₂ -	VDF-VDF / T-T	2.430
-CF ₂ -CHF-CF ₂ -CHF-CF ₂ -	TrFE-TrFE-VDF / H-T-T	3.464
-CF ₂ -CHF-CF ₂ -CHF-CH ₂ -	TrFE-TrFE / H-T	4.822
-CH ₂ -CF ₂ -CF ₂ -CHF-CH ₂ -	VDF-TrFE-VDF / T-T-T	7.590
-CF ₂ -CF ₂ -CHF-CH ₂ -CF ₂ -	TrFE-VDF / T-T	7.340
-CH ₂ -CF ₂ -CHF-CF ₂ -CH ₂ -	VDF-TrFE / H-T	0.213

^a The head (H) is designated as CF₂ while the tail (T) is CH₂ or CFCI

Table 4 - Tacticity of P(VDF-TrFE) 81.2/18.8 mol%. Source: Reference 47.

For a comparison, nearly identical terpolymers were synthesized using both direct polymerization and the two step hydrogenation approach. The breakdown of the tacticities for the direct and two-step polymer approaches are shown in Table 5 and Table 6 respectively. The direct polymerized terpolymer contains 45.67% head to tail links for VDF to VDF compared to 27.25% for the hydrogenation terpolymer. The direct polymerized terpolymer also contains 8.9% of head to tail links for VDF to TrFE as well as 6.4% tail to tail links for VDF to TrFE. The hydrogenated terpolymer in contrast shows only 0.090 % head to tail links for VDF to TrFE implying that almost all the VDF to TrFE links exist as tail to tail. These results for the hydrogenated terpolymer echo the earlier P(VDF-CTFE) data showing a terpolymer that contains a high number of tacticity defects compared to the directly polymerized terpolymer. Given the strong dependence of the properties of ferroelectric fluoropolymers on the defect level, it is expected that terpolymers produced by the two polymerization methods will have different electrical, thermal, and microstructures at the same chemical composition.

P(VDF-CTFE-TrFE) 81.2/7.2/11.6 mol%		
Sequence	Designation ^a	Percentage (%)
-CF ₂ CH ₂ CF ₂ CH ₂ CF ₂ -	VDF-VDF/H-T	27.25
-CHFCH ₂ CF ₂ CH ₂ CF ₂ -	TrFE-VDF/T-T	19.40
-CCIFCH ₂ CF ₂ CH ₂ CF ₂ -	CTFE-VDF/T-T	
-CH ₂ CH ₂ CF ₂ CH ₂ CF ₂ -	VDF-VDF-VDF/T-T-H	5.646
-CF ₂ CCIFCF ₂ CCIFCF ₂ -	CTFE-CTFE/H-T	1.719
-CF ₂ CH ₂ CF ₂ CF ₂ CCIF-	VDF-CTFE/T-T	3.755
-CF ₂ CCIFCF ₂ CCIFCH ₂ -	CTFE-CTFE-VDF/H-T-T	1.956
-CF ₂ CH ₂ CF ₂ CF ₂ CHF-	VDF-TrFE/T-T	8.294
-CF ₂ CH ₂ CF ₂ CF ₂ CH ₂ -	VDF-VDF/T-T	2.117
-CH ₂ CF ₂ CF ₂ CH ₂ CH ₂ -	VDF-VDF/T-T	2.041
-CH ₂ CF ₂ CF ₂ CCIFCH ₂ -	VDF-CTFE/T-T	2.831
-CF ₂ CF ₂ CCIFCH ₂ CF ₂ -	CTFE-VDF/T-T	3.300
-CF ₂ CHF ₂ CF ₂ CHF ₂ CF ₂ -	TrFE-TrFE/H-T	2.940
-CF ₂ CHF ₂ CF ₂ CHF ₂ CH ₂ -	TrFE-TrFE-VDF/H-T-T	3.308
-CH ₂ CF ₂ CF ₂ CHF ₂ CH ₂ -	VDF-TrFE-VDF/T-T	2.842
-CF ₂ CFCICF ₂ CHF ₂ CH ₂ -	CTFE-TrFE-VDF/H-T-T	2.354
-CH ₂ CF ₂ CCIFCF ₂ CH ₂ -	VDF-CTFE-VDF/H-T-H	0.046
-CF ₂ CF ₂ CHF ₂ CH ₂ CF ₂ -	TrFE-VDF/T-T	5.063
-CH ₂ CF ₂ CHF ₂ CF ₂ CH ₂ -	VDF-TrFE/H-T	0.090

^a The head (H) is designated as CF₂ while the tail (T) is CH₂ or CFCI

Table 5 - Tacticity of P(VDF-CTFE-TrFE) 81.2/7.2/18.8 mol% produced by the two-step synthesis procedure. Source: Reference 47.

P(VDF-CTFE-TrFE) 81.0/8.3/10.7 mol%		
Sequence	Designation ^a	Percentage (%)
-CF ₂ CH ₂ CF ₂ CH ₂ CF ₂ -	VDF-VDF / H-T	45.67
-CHFCH ₂ CF ₂ CH ₂ CF ₂ -	TrFE-VDF / T-T	2.224
-CCIFCH ₂ CF ₂ CH ₂ CF ₂ -	CTFE-VDF / T-T	
-CH ₂ CH ₂ CF ₂ CH ₂ CF ₂ -	VDF-VDF-VDF / T-T-H	1.824
-CF ₂ CCIFCF ₂ CCIFCF ₂ -	CTFE-CTFE / H-T	0.973
-CF ₂ CHF ₂ CF ₂ CH ₂ CF ₂ -	TrFE-VDF / H-T	4.759
-CH ₂ CH ₂ CF ₂ CHF ₂ CF ₂ -	VDF-TrFE / H-T	4.160
-CF ₂ CH ₂ CF ₂ CF ₂ CCIF-	VDF-CTFE / T-T	2.570
-CFCICH ₂ CF ₂ CF ₂ CCIF-	VDF-CTFE / T-T	3.438
-CF ₂ CHF ₂ CF ₂ CF ₂ CCIF-	TrFE-CTFE / T-T	3.133
-CF ₂ CH ₂ CF ₂ CF ₂ CHF-	VDF-TrFE / T-T	2.808
-CF ₂ CH ₂ CF ₂ CF ₂ CH ₂ -	VDF-VDF / T-T	2.675
-CH ₂ CF ₂ CF ₂ CH ₂ CH ₂ -	VDF-VDF / T-T	2.418
-CH ₂ CF ₂ CF ₂ CCIFCH ₂ -	VDF-CTFE / T-T	3.011
-CHF ₂ CF ₂ CF ₂ CFCICH ₂ -	TrFE-CTFE-VDF/T-T-T	1.064
-CF ₂ CF ₂ CCIFCH ₂ CF ₂ -	CTFE-VDF / T-T	1.550
-CF ₂ CHF ₂ CF ₂ CHF ₂ CF ₂ -	TrFE-TrFE / H-T	2.737
-CHFCHF ₂ CF ₂ CF ₂ CHF-	TrFE-TrFE / T-T	1.570
-CHFCHF ₂ CF ₂ CHF ₂ CF ₂ -	TrFE-TrFE-TrFE / H-T-T	0.604
-CF ₂ CHF ₂ CF ₂ CF ₂ CHF	TrFE-TrFE / T-T	
-CF ₂ CHF ₂ CF ₂ CHFCH ₂ -	TrFE-TrFE-VDF / H-T-T	1.033
-CH ₂ CF ₂ CF ₂ CHFCH ₂ -	VDF-TrFE-VDF / T-T-T	0.828
-CF ₂ CFCICF ₂ CHFCH ₂ -	CTFE-TrFE-VDF/H-T-T	0.598
-CH ₂ CF ₂ CCIFCF ₂ CH ₂ -	VDF-CTFE / H-T	0.154
-CF ₂ CF ₂ CHFCH ₂ CF ₂ -	TrFE-VDF / T-T	1.306
-CH ₂ CF ₂ CHF ₂ CF ₂ CH ₂ -	VDF-TrFE / H-T	1.546

^a The head (H) is designated as CF₂ while the tail (T) is CH₂ or CFCI

Table 6 - Tacticity of P(VDF-CTFE-TrFE) 81.0/8.3/10.7 mol% produced by direct polymerization. Source: Reference 47.

Thermal Properties

The melting behavior of the polymers were measured with DSC as described in the experimental sections. Two complete temperature scans were taken from 0 to 200 to

0°C of which the first scan data was discarded. The purpose of the first scan was to erase any thermal history of the polymers before collecting the actual data. A plot of the melting temperatures (T_m) is shown in Figure 18 for the eight VDF compositions. Two trends are observed from the data. The first is a near linear dependence of the T_m with the amount of TrFE in the polymers. This dependence hints that the crystallinity of the polymers also has a linear dependence since the origin of the melting exotherms is crystal melting. The second trend is the increase in the T_m of the polymers as the amount of VDF increases or a shift of a curves up and to the left. This trend becomes a little muddled, but in general the T_m 's of a grouping of polymers with a fixed amount of VDF increases with the amount of VDF. This also hints that overall crystallinity increases with increasing VDF.

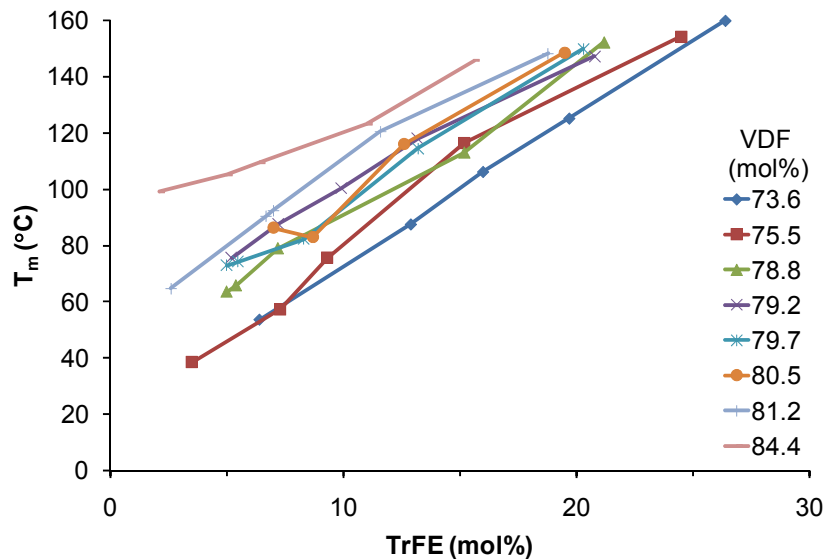


Figure 18 - Melting temperatures of all the polymers synthesized by two step synthesis procedure.

The individual heating and cooling DSC traces for the 79.2 mol% VDF group of polymers are shown in Figure 19 and Figure 20 respectively. Table 7 lists all the

transition temperatures and enthalpies (ΔH) for the polymers. All of the polymers show sharp endo and exotherms indicating a uniform crystal size distribution. As the amount of TrFE increases, the T_m of the terpolymers increases from 75°C for the sample with 15.6 mol% CTFE up to 146°C for the polymer with no CTFE. The enthalpies of melting and crystallization also increase with the amount of TrFE showing that the crystallinity increases. Apart from the strong endotherm peaks, each melting curve also shows a minor endothermic peak at lower temperatures associated with the ferroelectric to paraelectric phase change of the Curie transition.⁴⁸ Upon cooling, the polymers show sharp exotherms associated with the crystallization temperature (T_{cr}) at temperatures lower than T_m . The minor exotherms associated with the Curie transition are also present. As the CTFE is increased, the difference between the T_c for the same polymer upon heating and cooling increases from 3 to 12°C between the 20.8 to 5.2 mol% TrFE polymers indicating an increase in the hysteresis of the Curie transition. Absent from the figures is P(VDF-CTFE) copolymer which was a sticky, completely amorphous material with no peaks in the thermal scans illustrating how CTFE can disrupt crystallinity. In general, all the groupings of polymers show similar trends to the one presented here. The complete data for all the polymers is located in Appendix A.

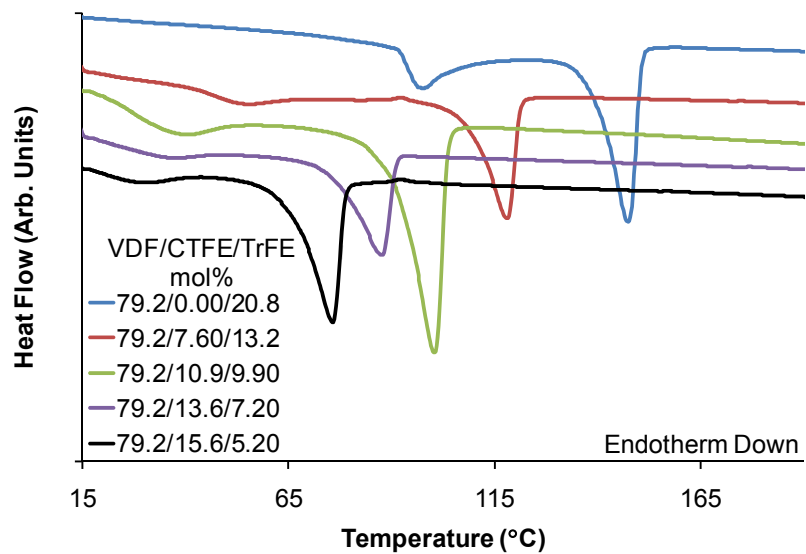


Figure 19 - DSC heating curves for 79.2 mol% VDF polymers.

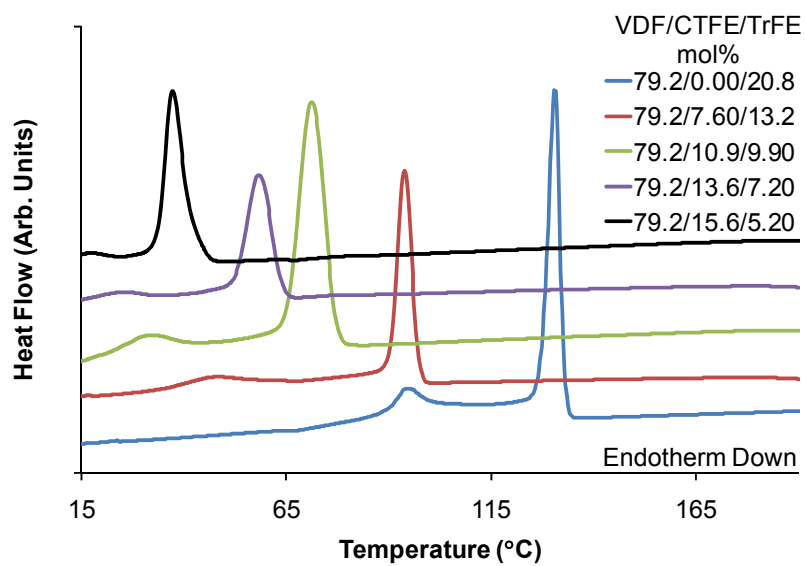


Figure 20 - DSC cooling curves for 79.2 mol% VDF polymers.

mol(%)			Heating				Cooling			
			°C		J/g		°C		J/g	
VDF	CTFE	TrFE	T _c	T _m	ΔH _c	ΔH _m	T _c	T _{cr}	ΔH _c	ΔH _{cr}
79.2	0.00	20.8	97	147	8.28	25.7	94	130	6.27	28.4
79.2	7.60	13.2	54	118	3.01	18.1	47	94	3.94	20.8
79.2	10.9	9.90	38	100	3.21	16.3	31	71	2.13	17.2
79.2	13.6	7.20	36	88	2.29	12.1	25	58	0.89	13.4
79.2	15.6	5.20	29	76	1.09	10.9	17	37		10.1

Table 7 - Transition temperatures and enthalpies for the 79.2 mol% VDF polymers.

Crystal Structure

WAXD and FTIR were both used to examine the crystal structure of the polymers. The overall crystallinity (χ_c) of the polymers was approximated by calculating the ratio of the crystalline peaks compared to the amorphous halo in the diffraction scans measured at 1°/min from 5° to 50°. The crystallinity, shown in Table 8, decreases as the amount of CTFE increases illustrating how the bulky chlorine defect disrupts crystal formation. This trend echoes the trend seen in the decreasing T_m and ΔH_m observed with increasing CTFE mol%. An optical microscope image of the polymer crystals is seen in Figure 21 for a P(VDF-TrFE) copolymer with 84.4 mol% VDF and 15.6 mol% TrFE. As the amount of CTFE increase, the size of the polymer crystals were observed to decrease.

mol%			χ_c (%)
VDF	CTFE	TrFE	
73.6	0.00	26.4	42.4
73.6	6.70	19.7	40.4
73.6	10.4	16.0	35.8
73.6	13.5	12.9	32.7
73.6	20.0	6.40	17.7
78.8	0.00	21.2	50.2
78.8	6.00	15.2	42.5
78.8	14.0	7.20	36.3
78.8	15.8	5.40	32.2
78.8	16.2	5.00	28.5
79.2	0.00	20.8	52.9
79.2	7.60	13.2	41.8
79.2	10.9	9.90	33.1
79.2	13.6	7.20	32.9
79.2	15.6	5.20	29.2
81.2	0.00	18.8	52.5
81.2	7.20	11.6	34.3
81.2	11.8	7.00	32.2
81.2	12.1	6.70	25.3

Table 8 - Crystallinity of hydrogenated polymers.

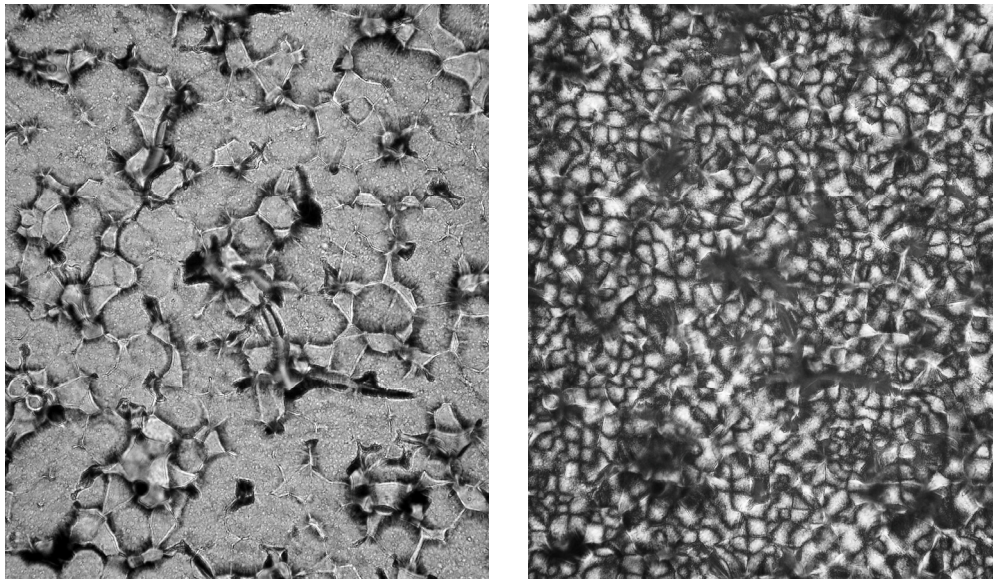


Figure 21 - Optical microscope image of P(VDF-TrFE) 84.8/15.6 mol% at 400x of the same area. Left: Unpolarized. Right: Crossed polarizers.

FTIR scans revealed the information about the individual crystal phases in the polymers by examining the vibrations associated with the different conformations of the chains.^{49,50} Two bands were used to identify trans sequences in the chains. The first was at 1290 cm^{-1} which is associated with asymmetric stretching, symmetric stretching, and bending modes of CF_2 , CC, CCC respectively and measures trans sequences greater than 4 ($T>4$). The second at 850 cm^{-1} identifies asymmetric stretching of the CF_2 of trans sequences greater than 3 ($T>3$). One band at 614 cm^{-1} of the bending mode of CF_2 and CCC was used to identify trans-gauche sequences (TG). The last band at 505 cm^{-1} is associated with the CF_2 bending mode of the $\text{TTTG}^+\text{TTTG}^-$ sequences. The FTIR spectra for the 78.8 mol% VDF family of polymers are shown in Figure 22. The two peaks of the trans sequences has a maximum peak with the P(VDF-TrFE) showing that the copolymer crystallizes in the β phase which is expected. These trans peaks disappear as CTFE is incorporated in the terpolymers. The $\text{TTTG}^+\text{TTTG}^-$ peak remain constant for the terpolymers indicating the γ phase is preferred for these materials. The TG peak remains fairly constant for all the polymers indicating that some amount of the α phase is retained no matter the chemical composition.

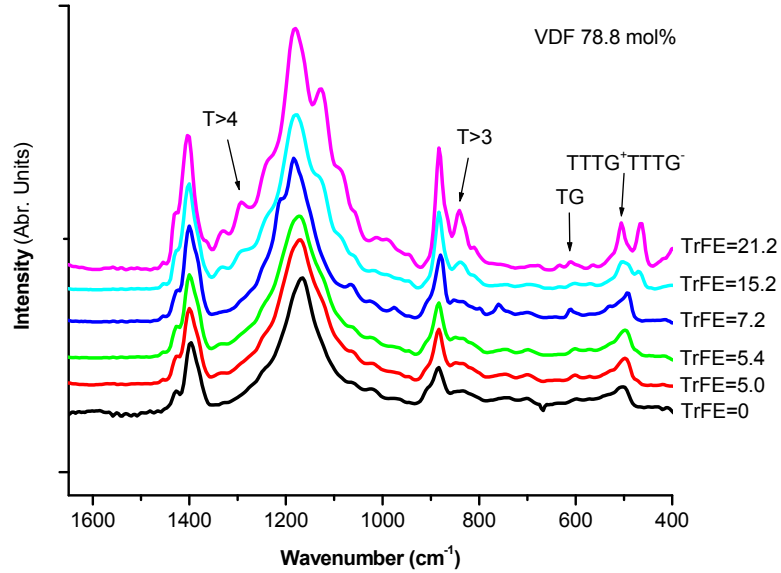


Figure 22 - FTIR spectra for the 78.8 mol% VDF grouping of polymers.

The conformation versus temperature for P(VDF-CTFE-TrFE) terpolymer of composition 81.2/7.2/11.6 mol% is shown in Figure 23 measured from FTIR spectra. At room temperature, the terpolymers starts with 60% and 40% of the trans and TTTG⁺TTTG⁻ segments associated with the β and γ phases respectively. Upon heating, the two amounts remain constant until about 60°C where the TTTG⁺TTTG⁻ sequences increase at the expense of the trans sequences. This temperature roughly matches the T_c of 68°C measured by DSC where the material is expected to become paraelectric. Above the melt temperature of 120°C, the trans sequences disappear with the appearance of a small amount of TG sequences. At these temperatures, these FTIR signals from the chain conformations most likely originate from small, ordered, sequences in a disordered melt and don't represent actual crystals.

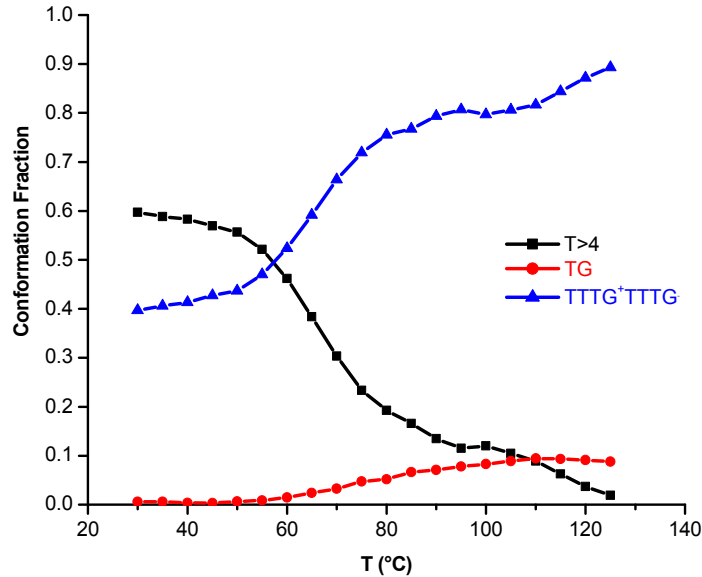


Figure 23 - Conformation as function of temperature for P(VDF-CTFE-TrFE) 81.2/7.2/11.6 mol%.

Dielectric Properties

The room temperature dielectric properties were measured for all the polymers as a function of frequency. The maximum electric field was approximately 0.05 MV/m. For each individual composition, at least three samples were measured and averaged for the final results. The permittivity of the 78.8 mol% VDF grouping is shown in Figure 24. The fully hydrogenated P(VDF-TrFE) copolymer shows the lowest permittivity across all the frequencies while the terpolymer with 7.2 mol% TrFE has over triple the permittivity in the same range. All the other terpolymers permittivities lie somewhere between these two extremes. For the TrFE copolymer, the permittivity is fairly constant with frequency indicating limited ferroelectric polarization by domain motion since its T_c is near 100 °C. The high crystallinity of this sample, implied from its high T_m and ΔH_m , is the most likely cause inhibiting domain motion. The 7.2 mol% TrFE terpolymer has drop off in permittivity around 100 kHz illustrating that the upper limit of the ferroelectric response

is being approached. This polymer's lower T_c around 23°C and lower crystallinity means that the ferroelectric domains have more mobility to contribute to the polarization. At a higher a CTFE composition for the 5.0 mol% TrFE polymer, the permittivity decreases about 20% since the CTFE lowers the crystallinity even further and reduces the number of ferroelectric domains. The data here shows that there exists an optimum amount of CTFE that both reduces crystallinity and T_c , and converts the β phase to the γ phase to achieve a high permittivity. The loss of all the polymers is flat until 10 kHz when it begins to rise for all the samples. This rise is greater for the high permittivity polymers due their high ferroelectric polarization contribution and coincides with their permittivity drop off. Most of the trends described here are duplicated across most of the VDF groupings. The complete room temperature data versus frequency for all the polymers is listed in Appendix B.

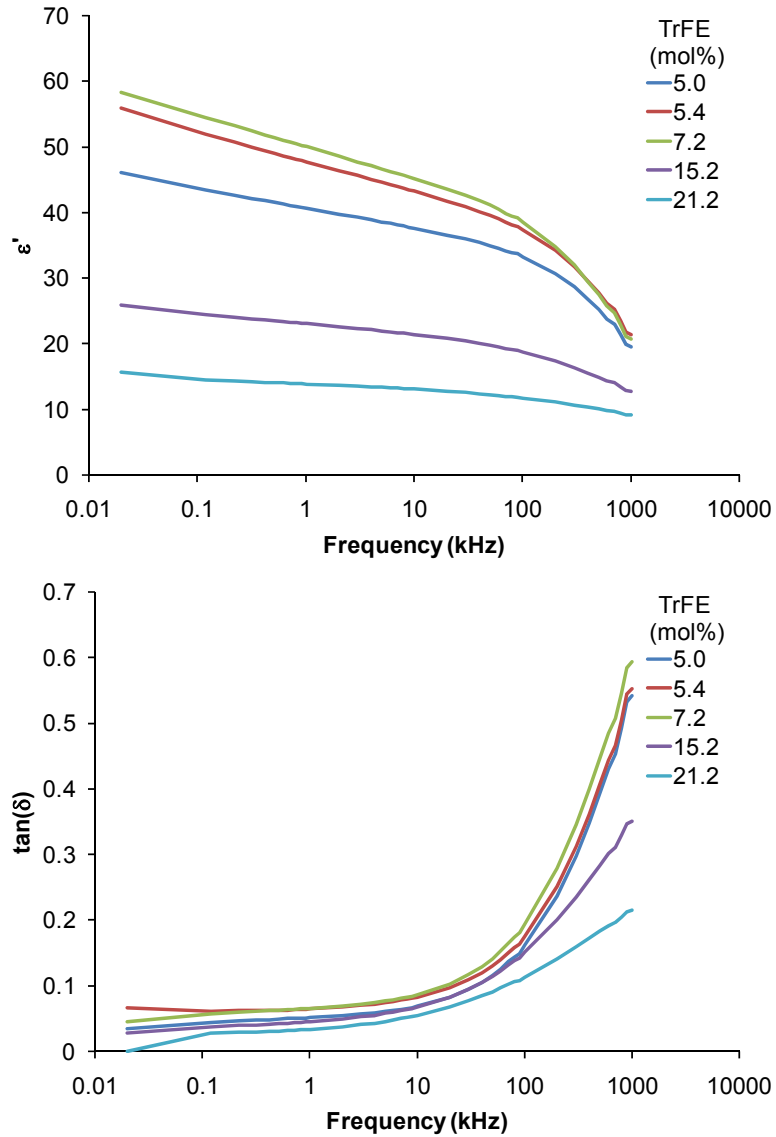


Figure 24 - Room temperature permittivity and loss tangent versus frequency for 78.8 VDF mol% polymers.

A comparison of all the permittivities of all the polymers measured at room temperature and 1 kHz is plotted in Figure 25. Each VDF grouping shows a maximum in permittivity at some intermediate terpolymer composition. At high CTFE amounts, the polymers are too amorphous for a high ferroelectric polarization. At high TrFE amounts, the polymers are too crystalline for significant ferroelectric motion for high polarizations. The maximum permittivity usually falls between compositions of 5 and 10 mol% TrFE

and overall permittivities range from 10 to 50. The losses of all the polymers at 1 kHz range from 3 to 8 % with larger values for the high permittivity polymers. A three dimensional surface was constructed from the permittivity data in Figure 25 and is shown in Appendix B.

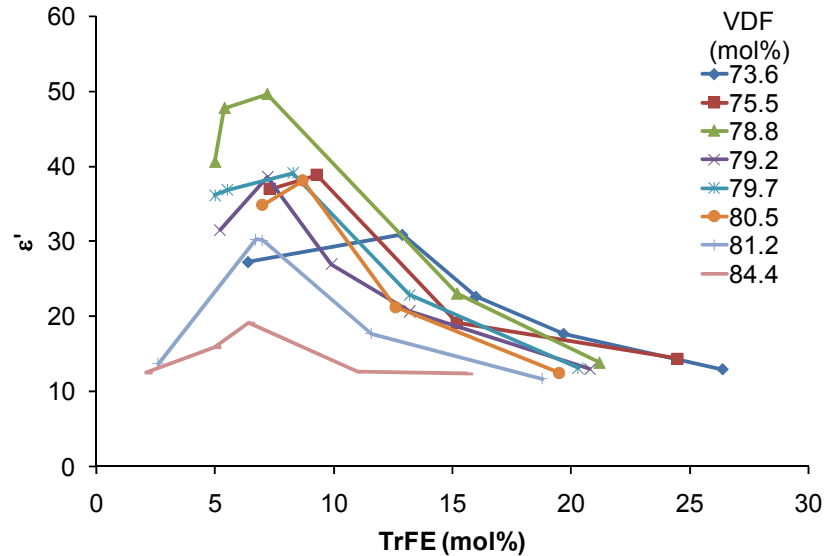


Figure 25 - Room temperature permittivities of the polymers at 1 kHz.

For the 78.8 VDF mol% grouping, the temperature varying dielectric properties were measured upon both heating and cooling at a rate of 2°C/min for a frequency range from 0.1 to 1000 kHz. The electric fields were approximately 0.05 MV/m. The complete spectra for this grouping is located in Appendix B. The ϵ' and ϵ'' spectra for the 21.2 mol% TrFE copolymer on heating is shown in Figure 26. The ϵ' plot shows one prominent peak for each frequency, labeled A, associated with the Curie transition where the permittivity balloons to almost 100 at low frequency. The ϵ'' plot at this zoom displays a single grouping of peaks, labeled α_c , that occurs in the same narrow temperature range of the Curie transition. This relaxation peak therefore is associated

with the Curie transition of the β to α ferroelectric to paraelectric phase change.³⁴ The dispersion of ϵ' peaks, which is about 10°C from high to low frequency, is due to the high tail to tail defect concentration influence on the crystals which prevents a sharp electrical phase transition.

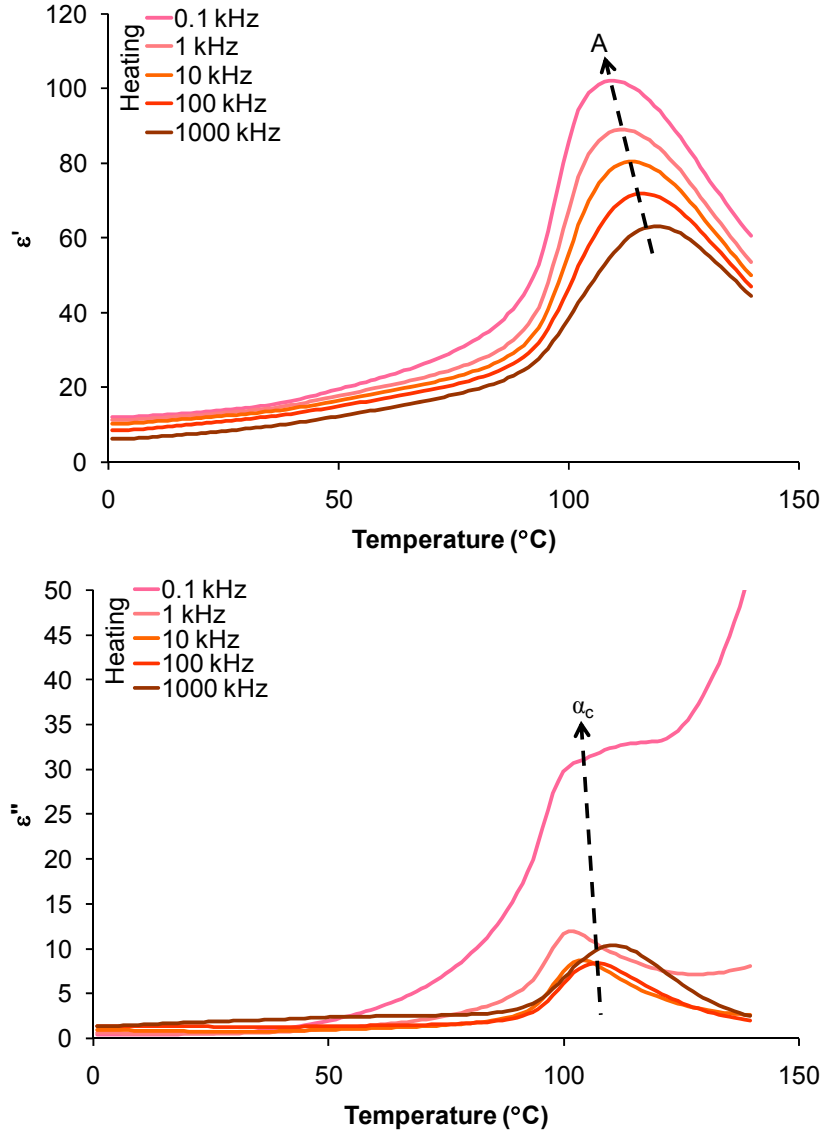


Figure 26 - Temperature varying dielectric properties on heating for P(VDF-CTFE-TrFE) 78.8/0.0/21.2 mol%.

Looking closer at the ϵ'' plot reveals two more relaxation peaks as shown in Figure 27. The first peak located at low temperature and labeled β_a is assigned to the relaxation of the amorphous regions of the polymer and is related to the glass transition. The location and intensity of the peaks are very similar to the relaxations seen in P(VDF).⁵¹ The second peak, label β_c , is assigned to a relaxation that may occur between the amorphous and crystalline interfaces.⁵² The exact mechanism of this relaxation is not well defined and still under debate. This relaxation is overtaken by the stronger α_c relaxation as T_c is approached and only observable at frequencies greater than 10 kHz in Figure 27.

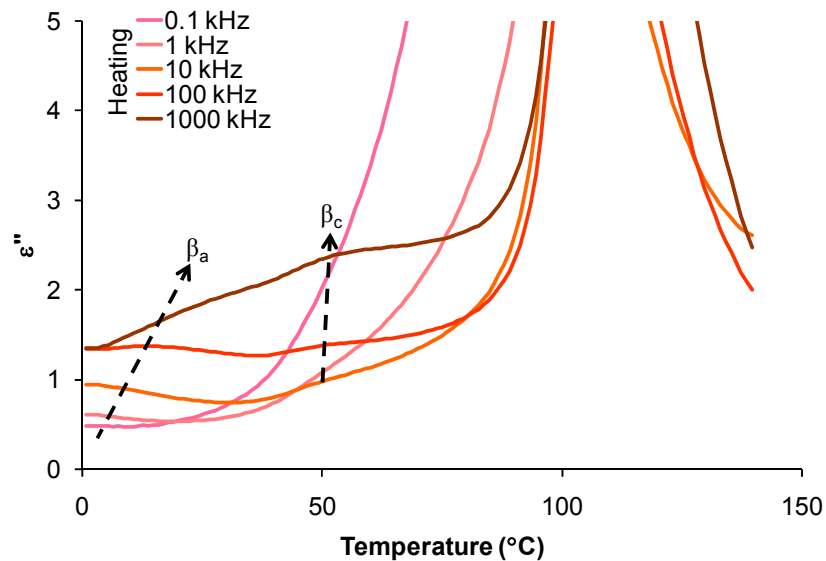


Figure 27 - Zoomed plot of temperature varying dielectric properties on heating for P(VDF-CTFE-TrFE) 78.8/0.0/21.2 mol%.

The dielectric behavior upon heating of the copolymer is contrasted to the terpolymer containing 7.2 mol% TrFE as shown in Figure 28. The ϵ' plot shows a strong dispersion of the peaks with frequency, a feature of relaxor ferroelectrics illustrated by the label B. However on the line labeled C, there is an additional set of peaks that

remains fixed with temperature, similar to the Curie transition seen on the P(VDF-TrFE) copolymer. Examining the ϵ'' spectra reveals a broad relaxation, labeled by β_r , that spreads over a temperature range of 60°C. This relaxation is a combination of amorphous relaxation β_a , as well as an additional relaxation originated from the polar domain motion associated with the γ phase of the polymer.⁵² The orientation of these polar domains with the electric field significantly increases the ϵ' response. The polar domain motion also significantly increases the ϵ'' an order of magnitude over just the β_a process when compared to previous copolymer and P(VDF).⁵¹ The peak labeled β_c is assigned to relaxation between the crystalline and amorphous region, but disappears in the β_r relaxation at higher frequencies.⁵² The last features are group of subtle peaks labeled α_c that reside in the same temperature region as label C on the ϵ' plot and are assigned to Curie transition. These peaks are slightly more prominent in the 5.0 and 5.4 mol% terpolymers whose spectra are in Appendix B. Thus, the terpolymer spectra presented here have features of both relaxor and normal ferroelectric behavior, though much more relaxor, suggesting some inhomogeneity in the crystal structure of the polymer. Nearly identical behavior is also observed 5.0 and 5.4 mol% terpolymers. The 15.2 mol% terpolymer also has evidence of this hybrid behavior, but its behavior is much more normal than relaxor ferroelectric. Its spectra are also shown in Appendix B. The data here shows that the transition from normal to relaxor ferroelectric behavior with decreasing TrFE is a gradual one.

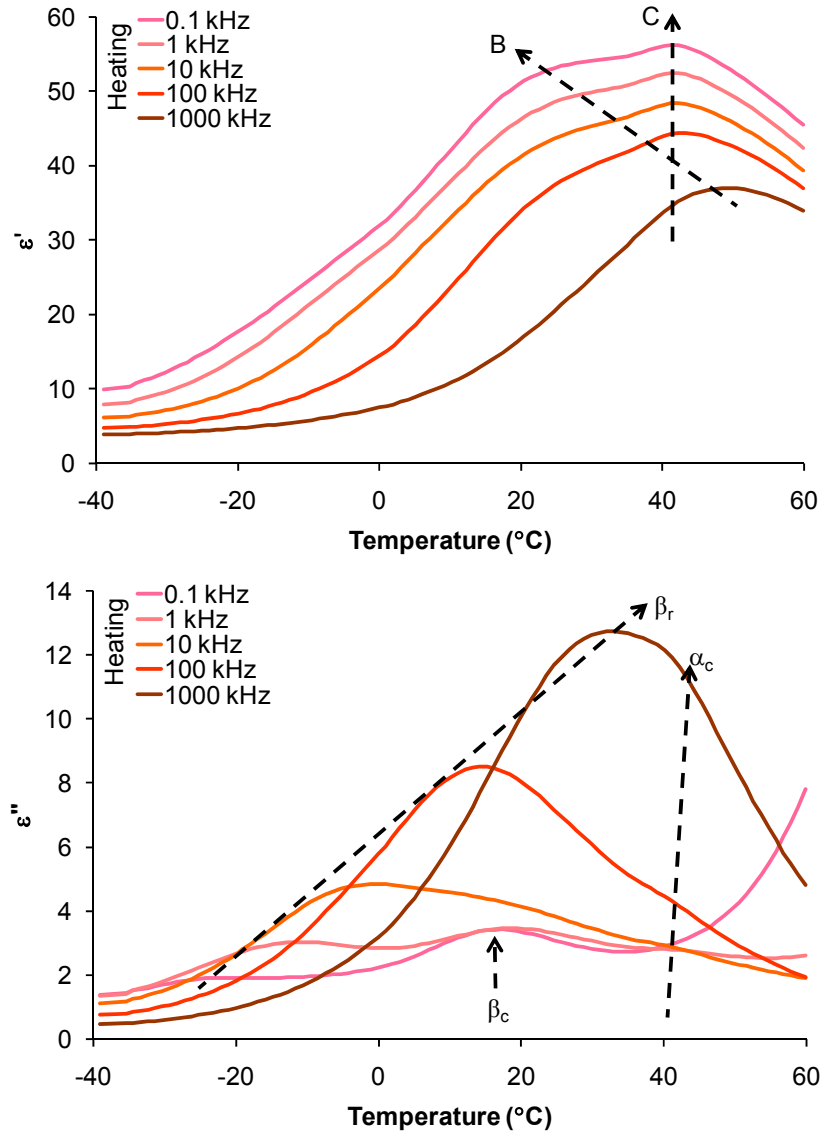


Figure 28 - Temperature varying dielectric properties on heating for P(VDF-CTFE-TrFE) 78.8/14.0/7.2 mol%.

Shown in Figure 29 is the corresponding cooling cycle of ϵ' and ϵ'' for the 7.2 TrFE mol% terpolymer. The ϵ' plot has smooth curves, labeled D, that shift with frequency displaying only relaxor behavior. The Curie transition peak, labeled C in Figure 28, observed on heating disappears along with the α_c relaxation in the ϵ'' plot. Instead only a relaxor-like ϵ' and ϵ'' curves are observed indicating the normal

ferroelectric phase doesn't have enough time to crystallize given the cooling rate of the experiment. The β_c relaxation is still present upon cooling.

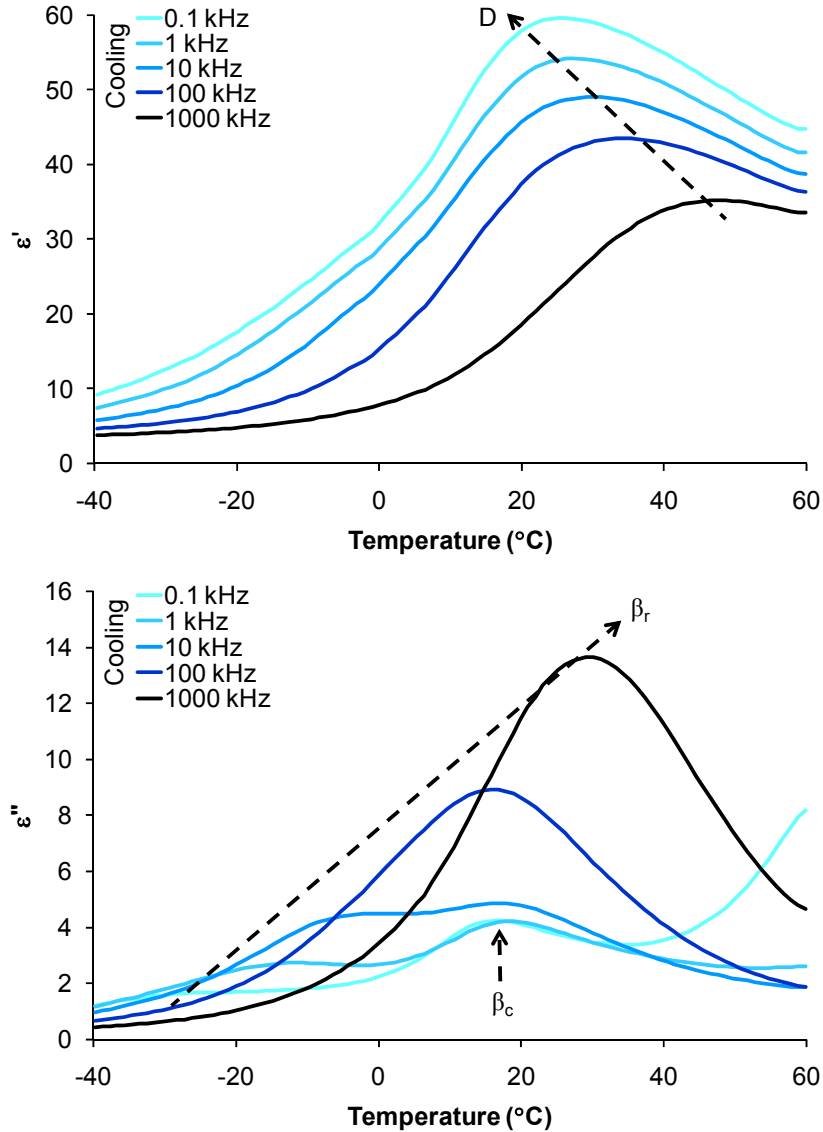


Figure 29 - Temperature varying dielectric properties on cooling for P(VDF-CTFE-TrFE) 78.8/14.0/7.2 mol%.

The T_c 's and T_m 's as a function of VDF composition of the measured hydrogenated copolymers are shown in Figure 30. The T_c 's were taken from the peak values of the permittivity versus temperature spectra measured at 1 kHz for the heating

cycle. In Figure 31, the peak permittivity at T_c is also plotted versus composition. The T_c 's of the copolymers decreases from 120°C to a minimum of 108°C and then rises to 112°C as the amount of VDF increases. The ϵ' shows an opposite trend of increasing from 49 to a maximum of 114 and back down to 82 with increasing VDF. The minimum in T_c corresponds exactly to a maximum in ϵ' . Comparing Figure 31 to a similar plot from reference 34 reveals that the ϵ' curve has a similar shape, though the maximum value occurs at 65 mol% VDF versus 79.7 for the hydrogenated polymers. The plot in reference 34 also shows that the T_c increases with VDF mol% in contrast to the minimum observed in Figure 30. The differences in these plots are due to the different microstructures from the hydrogenated polymers and the direct copolymerization used in the reference. While both copolymers crystallize in the β phase, the high amount of tail to tail defects in the polymers synthesized here lead to different crystal morphologies and dielectric properties. The hydrogenated copolymers have higher T_c 's and maximum ϵ' at a higher VDF mol% than the direct copolymerization copolymers. Figure 30 suggests a different phase diagram for these hydrogenated copolymers compared to the directly polymerized copolymers in Figure 16.

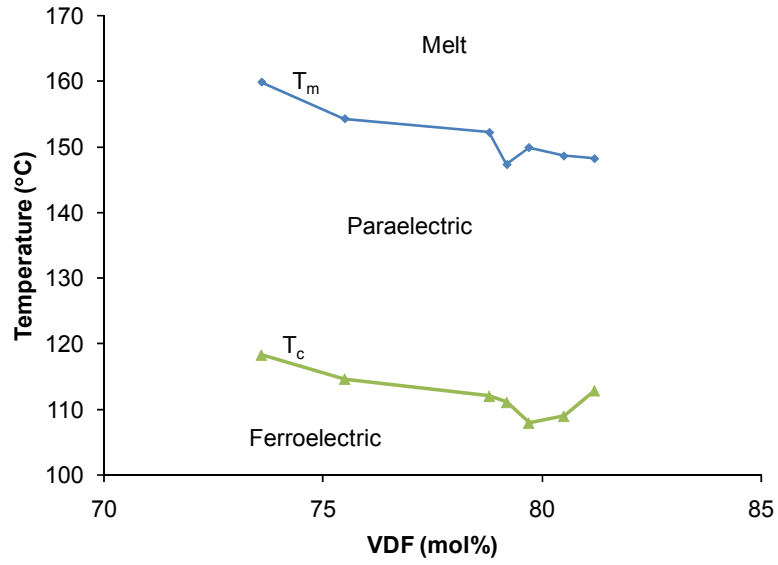


Figure 30 - Curie transition and melt temperatures for the dielectric data. T_c data collected for the dielectric heating cycles.

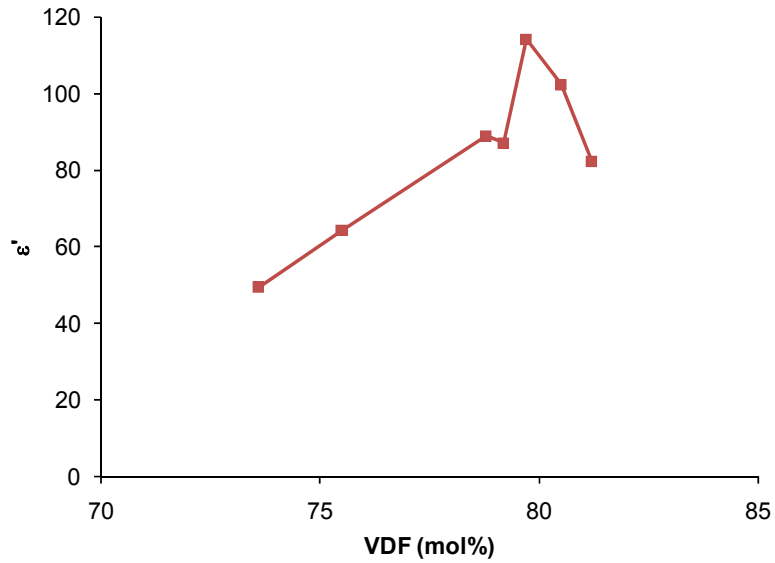


Figure 31 - Peak permittivity values from dielectric data measured at 1 kHz on the heating cycle.

CHAPTER 3 - ELECTRICAL BREAKDOWN IN P(VDF-CTFE) COPOLYMERS

Electrical Breakdown Review

Electrical breakdown is a complex phenomenon that occurs in insulating materials and is an important area of study for the performance of capacitor dielectrics. As mentioned in the introduction, the electric breakdown strength plays a big role in determining the energy density (Equation 14) of a capacitor necessitating research into its origin. Electrical breakdown is an irreversible, catastrophic event which, despite its initiation causes, ends in the creation of a conducting path through the dielectric material. Along the conducting path exists broken chemical bonds and thermally degraded materials resulting from the large amount of energy that passes through a small cross sectional area of the conduction path. For hydrocarbon based polymers, conductive forms of carbon, like graphite, are likely the conductive material. Electrical breakdown in a capacitor usually renders the device inoperative since any applied voltage will result in conduction and the device then performs more like a resistor. Electrical breakdown is a short time phenomenon, typically occurring at high electric fields and on time scales of less than 0.001 second.⁵³ This is in contrast to electrical degradation which is a process that typically occurs at lower electric fields on time scales greater than 1000 seconds and associated more with the long term performance of a material. The main mechanisms of electric degradation are the slow formation of conductive paths across the insulating material called electrical and water trees that have structures that resemble the branch structures of trees.

The mechanisms of electrical breakdown can be broadly put into four categories of electronic, thermal, electromechanical, and partial discharge and free volume breakdown. Electrical breakdown usually initiates in a material once it passes from a stable to unstable equilibrium. Under an applied electric field, the dielectric material will resist the stress placed on it through a negative feedback mechanism to maintain equilibrium. For example, current will flow through a dielectric to reduce the electric field placed across it. However at a certain field threshold, this negative feedback turns positive resulting in electrical breakdown. Returning to the conduction example, at high enough fields the conducting species will begin to degrade the material resulting in a higher conduction and faster degradation until breakdown. Predicting the field where the instability will occur is the focus of the study of electrical breakdown phenomenon.

Electronic electrical breakdown initiates from the destruction of chemical bonds from high energy electrons conducting through a dielectric.⁵⁴ Electronic breakdown occurs by either an intrinsic or an avalanche mechanism. In intrinsic breakdown, the energy that an electron gains in the electric field is balanced by that energy being dissipated through collisions as it travels through the dielectric and can be generally represented by the equation

$$A(E, T, \varphi) = B(T, \varphi)$$

Equation 15 - Energy dissipation in electronic breakdown.

where A is the rate at which an electron gains energy as a function of electric field (E), temperature (T), and φ which here represents any additional parameters. This is balanced by B which is the rate at which energy can be dissipated, which is also a function of temperature and φ . Energy loss in the dielectric occurs through interactions of the

electrons with the lattice of the material which can result in trapped states, phonon generation, or scission of the chemical bonds to name a few of them. Breakdown occurs at an electric field where the energy gained from the field isn't fully dissipated in the interaction resulting in electrons that can reach an even higher energy level before their next interaction. Eventually, these high energy electrons degrade the material resulting in breakdown. Avalanche breakdown occurs by a similar mechanism, except it relies on a chain reaction that results in the generation of many runaway electrons. At the breakdown field, a single high electron collides with a bound electron creating two free electrons. These two electrons in turn are accelerated and collide with two more electrons repeating this process until a large amount of free electrons cascade through the dielectric causing damage. Electronic breakdown represents the highest breakdown strength that can be measured in a material.⁵⁵ This mechanism has been verified through careful measurements for inorganic salts and polyethylene at low temperatures.^{54,55} However difficulty in sample preparation and breakdown at lower fields by the other mechanisms that will be discussed has prevented this mechanism from being widely observed. Thus, electronic breakdown is rarely observed.

Like electronic breakdown, thermal breakdown also begins with a power balance which can be represented by

$$\sigma(T, E)E^2 = CD\left(\frac{dT}{dt}\right) - \text{div}(\kappa\nabla T)$$

Equation 16 - Thermal breakdown power balance.

where σ is the conductivity, C is the heat capacity of the material, D is the density, T is the temperature, and κ is the thermal conductivity.⁵⁶ The left hand side of the equation

represents the power dissipation from electrical conduction that occurs whenever an electric field is applied to an insulating material. This is balanced on the right hand side of the equation by two terms. The first term represents the power absorbed by the dielectric and the temperature rise associated with it. The second term represents the power dissipated by thermal conduction to the surroundings outside of the dielectric. At fields below the breakdown threshold, the power dissipated from conduction causes the temperature to rise in the dielectric, but eventually stabilizes as the excess power is conducted away to the surroundings as heat. At fields higher than the breakdown threshold, thermal runaway occurs where the amount of heat conducted away from the material saturates causing the temperature of the dielectric to rise without control. Typically, this occurs in a positive feedback fashion where increased dielectric temperature increases the conductivity which increases the dielectric's temperature and so on. Thermal breakdown is typically sensitive to temperature since conductivity usually has a strong dependence on it and believed to be a fairly common breakdown mechanism in polymers. Thermal breakdown occurs at fields lower than electronic breakdown. A variety of models can be used to analyze and predict thermal breakdown.⁵⁶

Electromechanical breakdown is another breakdown mechanism believed to be common in polymeric materials since they are relatively soft materials and can encounter high electrostatic stresses at high electric fields. Electromechanical breakdown can be represented generally by the equation

$$\sigma_{EM} = \sigma_r$$

Equation 17 - Electromechanical stress balance.

where σ_{EM} is the electromechanical stress and σ_r is the repulsive stress in the dielectric. Whenever a capacitor is charged, an attractive force is generated from the oppositely charged electrodes which creates the electromechanical compressive stress on the dielectric. The only thing resisting this stress is the dielectric which generates an opposing stress from an elastic response. At the electrical breakdown field, the electromechanical stress exceeds yield stress of the dielectric causing it to deform plastically. At this point, the dielectric collapses in on itself with minimal resistance leading to breakdown. Electromechanical breakdown is common for rubbery materials above the glass transition temperature since a large drop in modulus is associated with this thermal transition making the rubbery polymers prone to deformation from the electromechanical stress.⁵⁵ Electromechanical breakdown occurs at fields lower than electronic breakdown. Like thermal breakdown, many different models exist for predicting electromechanical breakdown.⁵⁷

Partial discharge and free volume breakdown both revolve around discharge in voids in the dielectric material.⁵⁸ Partial discharge refers to discharge in larger sized pores on the order of a micrometer that usually result from improper processing. The permittivity of the pores is lower than the surrounding dielectric causing the electric field to be concentrated in that area leading to small scale breakdowns that cause damage and accumulate to larger breakdowns. Free volume breakdown refers to discharge that occurs on a smaller scale in the amorphous regions of a polymer. Electrons are able to accelerate through the nanometer sized spaces in the glassy regions leading to local damage and eventual breakdown. The free volume in the polymers is related to the chemical structure, temperature, as well and the intermolecular binding forces.

Breakdown for these two mechanisms occur at fields below electronic breakdown with partial discharge occurring at even lower fields based on the low breakdown strength of voids. Partial discharge and free volume breakdown can have long times to breakdown and straddle the barrier between short-time breakdown and long-time degradation.⁵³ In thin films where voids are on the size scale as the thickness, failure is by electrical breakdown. In thicker films, the slower degradation process dominates since it takes some time for a percolating conducting path to form.

This chapter will focus on studying the electrical breakdown mechanisms of a series of P(VDF-CTFE) copolymers with the same chemical composition, but varied molecular weights. As stated before, the electrical breakdown strength plays a strong role in determining the energy density of a dielectric material as shown by Equation 14. Understanding the mechanisms of breakdown is the first step towards increasing breakdown strength and energy density. Recently, an energy density of over 17 J/cm^3 at 575 MV/m was reported in a P(VDF-CTFE) copolymer illustrating that high energy densities can be reached provided that the dielectric can resist electrical breakdown.⁵⁹ The P(VDF-CTFE) chosen for this study had a high amount of CTFE that significantly reduced the crystallinity, but did not eliminate it, to create materials as isotropic as possible minus the intended molecular weight differences. While a wealth of literature exists on the subject of electrical breakdown in polymers, very little exists for fluoropolymers like P(VDF) and is virtually nonexistent for copolymers which have the potential to become important capacitor dielectric materials.

Experimental Procedure

Materials

All chemicals were used as purchased without purification unless otherwise noted. Hydrogen peroxide (30 wt% aqueous solution) was purchased from Alfa Aesar. Diethyl carbonate, methanol, acetone, and N, N-dimethylformamide (DMF) were purchased from Aldrich. Tetrahydrofuran (THF) was also purchased from Aldrich and distilled over sodium. Ethyl hydroxyethyl cellulose was purchased from Polysciences Inc.. Vinylidene fluoride (VDF) and chlorotrifluoroethylene (CTFE) were purchased from SynQuest Laboratory Inc. and purified by a freeze-thaw process.

Emulsion Polymerization of P(VDF-CTFE) Copolymer (Representative Experiment)

P(VDF-CTFE) copolymers were made by a free-radical emulsion polymerization. A steel, high pressure autoclave was filled with hydrogen peroxide as the initiator, cellulose as the surfactant, diethyl carbonate as a chain transfer agent, and distilled water as the continuous phase and degassed by repeated freeze-degass-thaw cycles. The autoclave was then cooled with liquid nitrogen to approximately -200°C where VDF and CTFE monomer were separately condensed. After adding the monomer, the autoclave was sealed and heated at 130°C for 24 hrs for polymerization. The end product was a white polymer which was rinsed with methanol and distilled water and dried under vacuum at 60°C for 24 hours to remove any liquid.

Film Preparation

P(VDF-CTFE) films approximately 20 micrometers thick were created by solution casting with DMF solvent. The polymer was dissolved in DMF and filtered

through a 0.45 micrometer Teflon filter to remove any particulates before casting onto a glass slide. The films were dried at 70°C overnight to remove the majority of the DMF. The films were released from the glass substrate by soaking in distilled water overnight and carefully peeling them from the substrate to create freestanding films. A final drying under high vacuum for 24 hrs was done for complete solvent removal.

Characterization

Sixty nanometer thick gold electrodes were sputtered onto the films for electrical testing. Room temperature dielectric measurements were made using an Agilent E4980A LCR Meter. Temperature varying dielectric properties were made using a Hewlett Packard 4284A LCR meter in conjunction with a Delta Design Oven model 2300. Thermal properties were measured on TA Instruments DSC Q100 differential scanning calorimeter (DSC). Mechanical properties were measured on a TA Instruments DMA 2980 dynamic mechanical analyzer (DMA). A Trek Model 30/20 ±30 kV High Voltage Amplifier System was used for electrical breakdown testing. All high voltage testing was performed in a highly insulating, perfluorinated polyether liquid called Galden HT fluid. The temperature for electrical breakdown testing was controlled with a NESLAB RTE Series bath circulator. Conduction measurements were made using a Hewlett Packard 4140B pA meter / DC voltage source with a Delta Design oven. Wide-angle x-ray diffraction (WAXD) studies were performed using a Scintag Cu-K_α diffractometer with a x-ray wavelength of 1.54 Å. Absolute molecular weight measurements were made using size exclusion chromatography (SEC) on a Viscotek model 302 Triple Detector System. Electrical displacement measurements were made using a Sawyer-Tower circuit at 10 Hz with a bipolar field.⁶⁰

Results and Discussion

Molecular Weight Characterization

Three different molecular weights of P(VDF-CTFE) were characterized with SEC with the data being shown in Table 9. The triple detector incorporated a refractive index, light scattering, and viscometer for the absolute values of the molecular weight. The number, weight, and z average molecular weights are represented by M_n , M_w , and M_z respectively. The M_n values range from 136 kg/mol to 294 kg/mol and will be used for referring to the individual polymer samples. The use of an emulsion polymerization method over the previously used solution method significantly increased the maximum achievable M_n of the polymers. The highest M_n possible with the solution method was 60 kg/mol versus 294 kg/mol with the emulsion method. This represents a near five-fold increase which will be shown to have a significant improvement in the mechanical properties of the polymer films. In order to control the M_n for this study, diethyl carbonate was used as a chain transfer agent during the polymerization to reduce the molecular weight. Increasing the amount of diethyl carbonate during the polymerization not only decreased M_n , but also decreased the polydispersity (PDI) of the polymers. The 294k sample without any chain transfer agent had the highest PDI at 1.72 which is still a relatively low value for a free-radical polymerization.⁶¹ On the other end, the 136k sample with the highest amount of chain transfer agent had a low value of 1.10 which is an especially low value for such a high molecular weight polymer produced by a free-radical process. Typically low PDI values like 1.10 are only seen in living polymerizations where there is much more control over the polymerization reaction.⁶¹

Overall, the chain transfer agent in the polymerization both lowered the molecular weight and narrowed the distribution of weights of the end polymer.

VDF-CTFE (mol %)	kg/mol			PDI (M_w/M_n)
	M_n	M_w	M_z	
78.4-21.6	136	150	188	1.10
78.6-21.4	164	217	533	1.32
78.4-21.6	294	504	2930	1.72

Table 9 - Absolute molecular weights of the P(VDF-CTFE) copolymers.

The relative degree of branching was also measured using SEC. The Mark-Houwink plots of the log of intrinsic viscosity versus the log of molecular weight were all linear with a Mark-Houwink exponent of approximately 0.60. These data indicate that the polymers are all linear and similar in structure. The addition of diethyl carbonate during polymerization does not cause any branching.

Thermal Properties

The thermal properties measured by DSC are summarized in Table 10. Again, the data reported is taken from second scan so that all the copolymers have the same thermal history. The heating and cooling scans are shown in Figure 32 and Figure 33 respectively. All the copolymers had broad melting endotherms around 100°C, strong glass transitions steps around -25°C, and small enthalpies of melting indicating that the copolymers are mostly amorphous. The 294k sample had a slightly larger T_m and ΔH_m possibly due to larger or better formed crystals in the sample from longer sequences of VDF. The cooling curves display sharper crystallization transitions, but require a large undercooling. The glass transition and enthalpies of crystallization are identical to those in the melting process.

M_n (kg/mol)	T_g ($^{\circ}\text{C}$)	T_m ($^{\circ}\text{C}$)	ΔH_m (J/g)	T_{cr} ($^{\circ}\text{C}$)	ΔH_{cr} (J/g)
136	25	110	4	50	3.0
164	25	100	3	40	3.0
294	25	120	5	70	5.0

Table 10 - Thermal properties of the P(VDF-CTFE) 78.4-21.6 mol% copolymers.

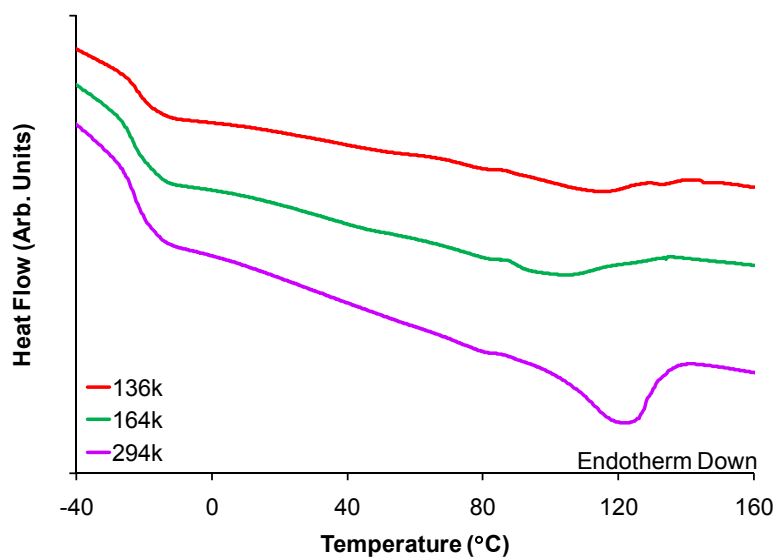


Figure 32 - DSC heating curves of the P(VDF-CTFE) 78.4-21.6 mol% copolymers.

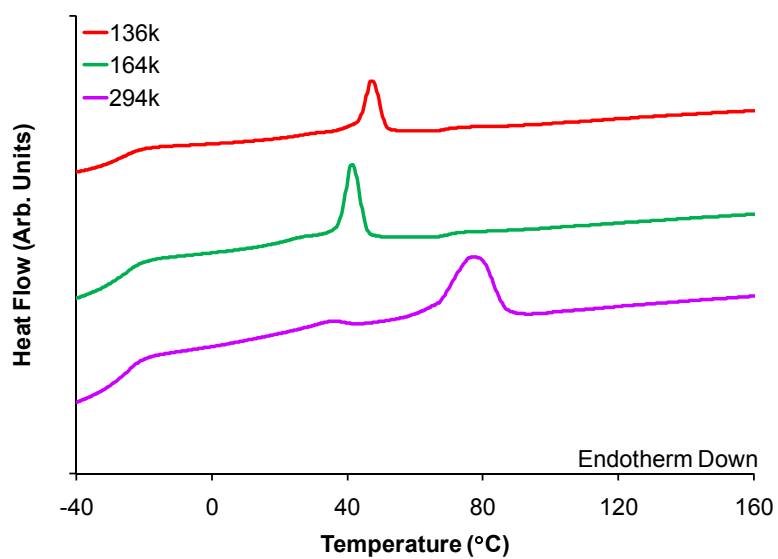


Figure 33 - DSC cooling curves of the P(VDF-CTFE) 78.4-21.6 mol% copolymers.

Crystal Structure

Structural characterization done with wide angle x-ray diffraction revealed a single, broad peak centered around a 2θ angle of 18.4° with a slight shoulder at 20.2° which indicates the presence of α phase crystals as shown in Figure 34.³¹ Crystallinity calculations on the diffraction patterns give χ_c of 18.4%, 15.0%, and 11.6% for the 136k, 164k, and 294k copolymers respectively. These crystallinity calculations are qualitative since a known standard was not available. As the molecular weight increases, the crystallinity of the copolymers decreases. Increasing the molecular weight frustrates the crystallization process through the creation of inter and intra chain entanglements which acts as defects to crystal formation. Despite the presence of some crystals, the polymers are almost completely amorphous which is demonstrated by the broad diffraction patterns, the previous DSC data, and following dielectric data. Additionally, optical microscope images under crossed polarizers revealed dark images with no indication of crystals.

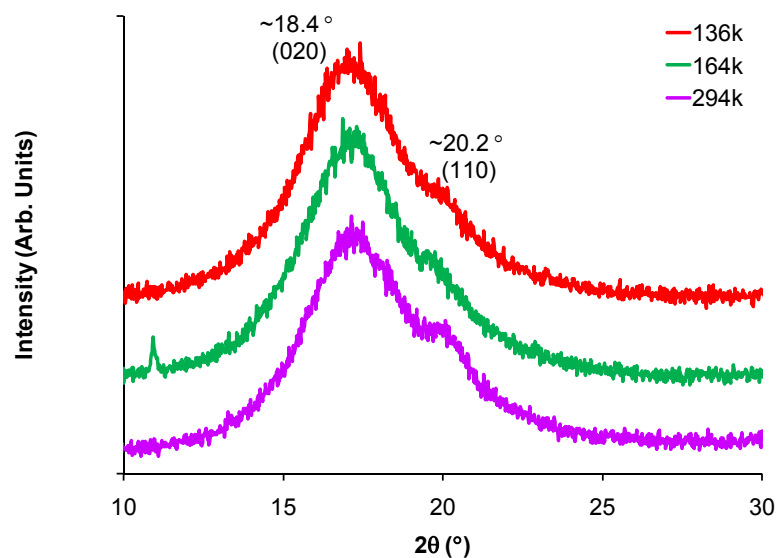


Figure 34 - Diffraction patterns for the P(VDF-CTFE) 78.4-21.6 mol% copolymers.

Dielectric Properties

The low field dielectric properties were measured to examine any effect that molecular weight might play. The maximum electric field was approximately 0.05 MV/m. The dielectric properties at 25°C are shown in Figure 35 and shows that all the copolymers have a similar ϵ' responses across the frequencies measured. The permittivity increases very slightly with M_n , but isn't significant. The copolymers ϵ' response is flat ranging from 10 to 9.7 from 100 Hz to 10 kHz and begins to fall above 10 kHz. The low overall ϵ' is due mostly to an amorphous structure and high amount of the paraelectric crystal phase. The loss of the polymers remains low below 0.08 between 10 Hz and 10 kHz and increases below and above this range. Below 100 Hz, the increased loss for the 136k and 164k sample may be related to the early onset of melting in the copolymers as seen in the DSC data. Above 10 kHz, the increase in loss is similar for all the samples and is linked to the dipole relaxation. As the frequency increases, the dipolar contribution to permittivity is reduced which corresponds to a decrease in the overall permittivity.

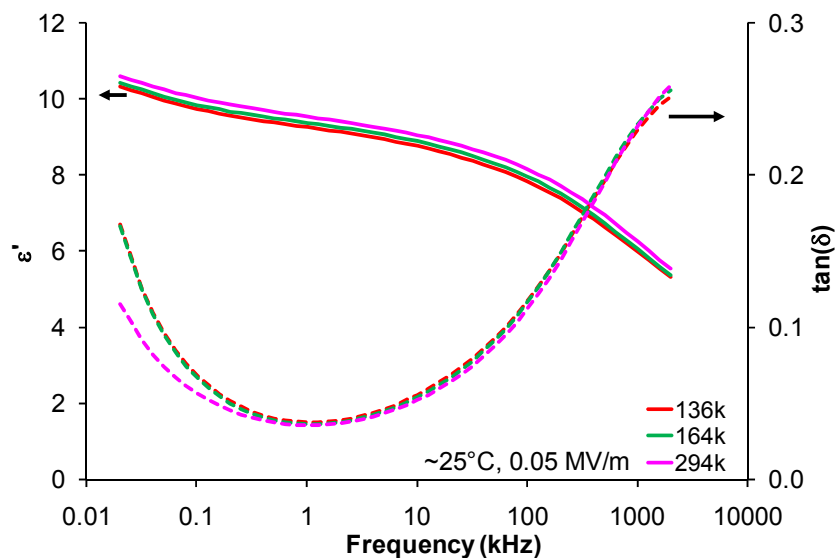


Figure 35 - Permittivity versus frequency measured at 25°C for the P(VDF-CTFE) 78.4-21.6 mol% copolymers.

The dielectric properties measured versus temperature for the 294k sample are shown in Figure 36. The permittivity at 1 kHz of the sample begins to fall from 9 around 0°C and settles around a value of 3.5 as it passes through the glass transition temperature (T_g) seen in the DSC data around -24°C. It's interesting to note that the polymer still retains approximately 30% of its room temperature permittivity below the T_g showing that not all of the dipolar response has been quenched in the glassy state. The ϵ'' of the sample features several peaks that shift to higher temperature with increasing frequency and represent the β_a relaxation process in the amorphous region of the polymer also seen in the hydrogenated polymers of the last chapter. The magnitude of this relaxation is similar to the hydrogenated P(VDF-TrFE) copolymers. The lack of any other peaks in the loss spectra also indicates an amorphous structure in the sample. The cooling spectra of the 294k sample traces almost exactly over the heating spectra showing that there is little thermal hysteresis in the dielectric properties. All of the samples had similar spectra

versus temperature. The measurements made at 25°C and at varying temperature confirm that all the samples share nearly identical dielectric properties which is important in the breakdown study to eliminate any effects from electronic differences.⁵⁴

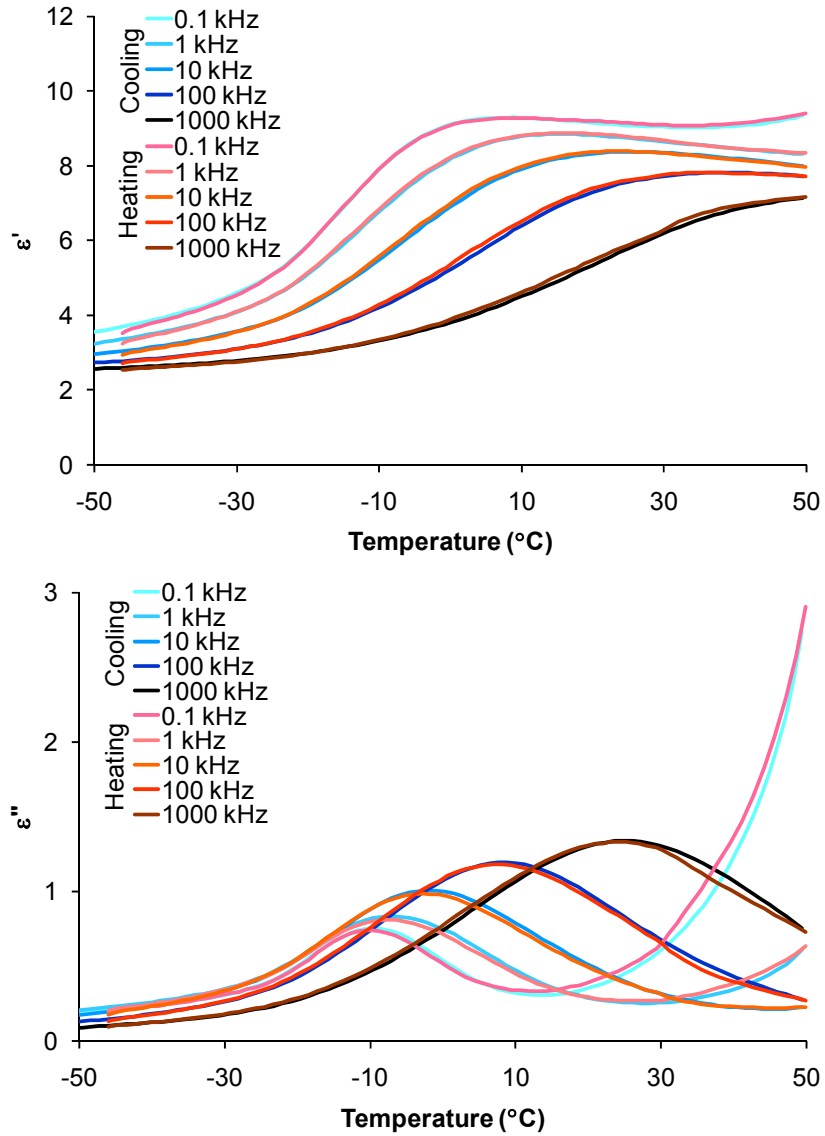


Figure 36 - Permittivity versus temperature upon heating for the 294k P(VDF-CTFE) 78.4/21.6 mol% copolymer.

Mechanical Properties

The low strain mechanical properties of the copolymers were measured with DMA with the data for the 294k copolymer shown in Figure 37. The polymers were measured to a maximum strain of about 0.30% where the complex modulus was recorded. The complex modulus is represented by

$$G = G' + iG''$$

Equation 18 - Complex modulus.

where G is the complex modulus, G' is the storage modulus, and G'' is the loss modulus.⁶² This expression is the mechanical analogy to Equation 7 for the application of a sinusoidal strain. The mechanical G' spectra showed a decrease in storage modulus of about two orders of magnitude from 1 GPa to 0.01 GPa as the temperature was increased. The corresponding G'' spectra show a single peak around -24°C which coincides with the drop in G' and is associated with glass transition in the copolymer. The lack of any other relaxations also shows the amorphous nature of the copolymers. The 136k and 164k copolymers showed the same behavior.

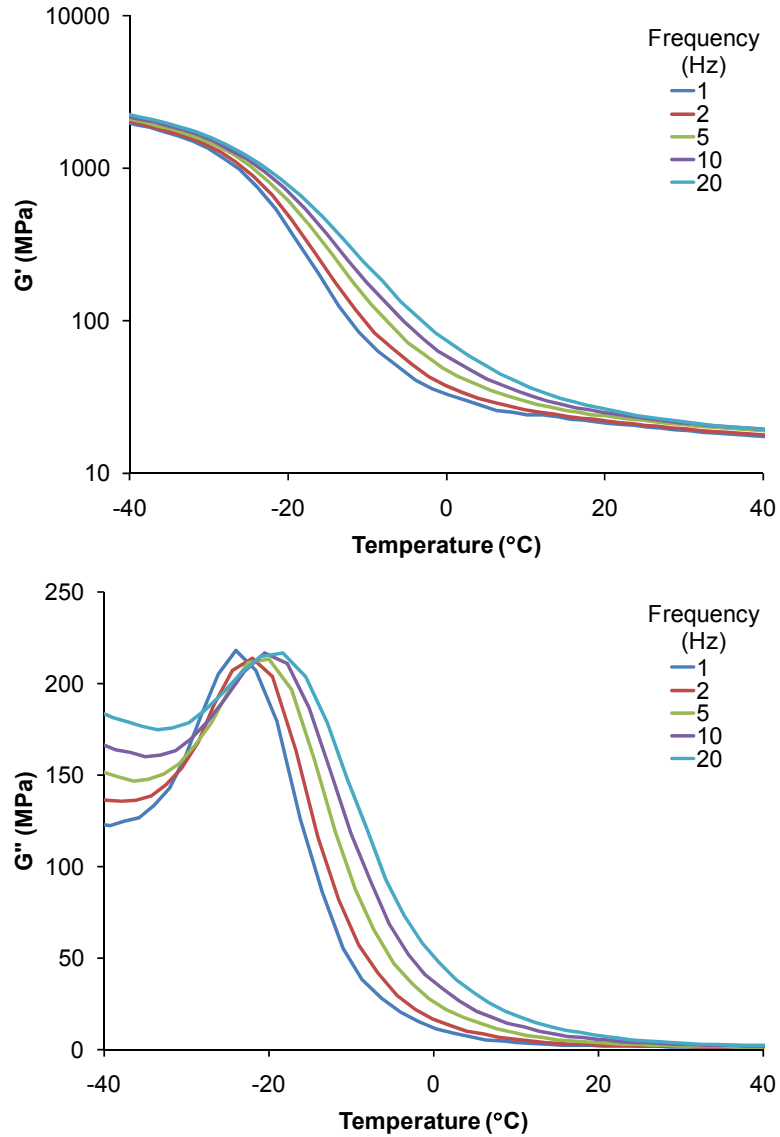


Figure 37 - Complex mechanical properties of the 294k P(VDF-CTFE) 78.4-21.6 mol% copolymer.

The summarized DMA results for the three copolymers measured at 1Hz are shown in Figure 38. At low temperatures, all the copolymers have identical storage moduli in the glassy state. As they are heated through the glass transition, the moduli begin separate and begin to show a trend where as the molecular weight increases, so does the storage moduli. Three different zones can be distinguished in Figure 38. The first is below the glass transition temperature in the glassy state where the polymers all

have identical G' . The second is slightly below the T_g where the G' value begin to separate and drop an order of magnitude. The final zone is around 25°C where the G' values separate and plateau to higher temperatures. Table 11 lists example values from each of these zones for the copolymers. The mechanical properties are the first area where there are distinct differences between the copolymers and why the electrical breakdown was tested in these three zones to see the effect of temperature on breakdown strength.

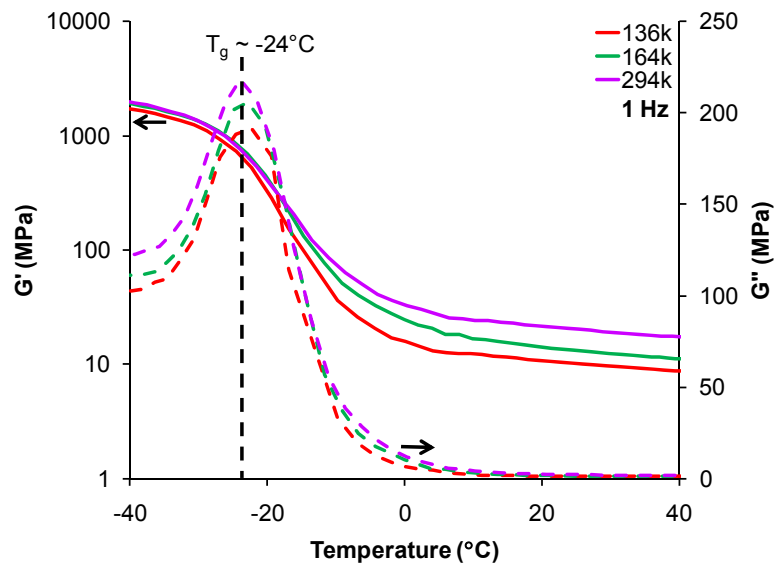


Figure 38 - Summarized complex moduli for the P(VDF-CTFE) 78.4-21.6 mol% copolymers.

M_n (kg/mol)	Storage Modulus (MPa)		
	-35°C	-15°C	25°C
136	1460	150	10.3
164	1640	133	13.7
294	1740	203	20.0

Table 11 - Storage moduli of the P(VDF-CTFE) 78.4-21.6 mol% copolymers.

To further explore the mechanical properties of the copolymers, the high strain mechanical properties were also measured with DMA. The tensile yield stress of the

samples were measured using a controlled force ramp through DMA at 25°C, -15°C, and -35°C to generate stress versus strain plots. At least four samples were measured and averaged for each copolymer at each of the temperatures. Since the yield behaviors of the copolymers were not sharp transitions, the individual yield stress was calculated from the intersection of two lines drawn tangent to the elastic and inelastic regions of the curve. The modulus was the slope of the elastic tangent line. An example of the plots, which were similar for all the copolymers, is shown in Figure 39 for the 294k sample.

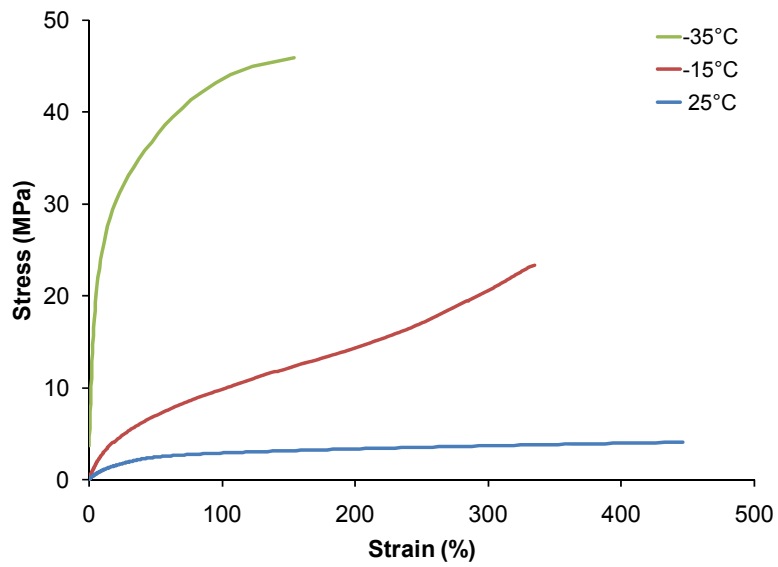


Figure 39 - Stress versus strain plot for the 294k P(VDF-CTFE) 78.4-21.6 mol% copolymer.

The calculated results for the high strain testing are listed in Table 12. The high strain modulus shows similar trends to the low strain storage modulus in Table 11. The discrepancies between the values can be attributed to the different frequencies of each test since the high strain test was performed at a frequency about an order of magnitude slower than the low strain test. Additionally, the high strain behavior of the copolymers changed significantly with temperature that wasn't observed at low strains. As shown in

Figure 39, the 294k sample shows simple yield behavior at 25°C, but at -15°C, strain hardening is observed near the failure strain.⁶³ At -35°C, brittle fracture occurs at the failure strain. Also of notice is the in Table 12 is the improvement in strain at break with increasing molecular weight attributable to an increase in chain entanglements and physical crosslinks.

Temperature	M_n (kg/mol)	136	164	294
-35°C	Modulus (MPa)	1640	1350	2300
	Yield Stress (MPa)	25.9	22.4	29.7
	Yield Strain (%)	2	2	1
	Strain at Break (%)	120	159	160
-15°C	Modulus (MPa)	21.9	28.7	36.3
	Yield Stress (MPa)	3.46	3.52	6.21
	Yield Strain (%)	16	12	17
	Strain at Break (%)	261	301	323
25°C	Modulus (MPa)	7.40	9.46	13.5
	Yield Stress (MPa)	1.31	1.94	2.75
	Yield Strain (%)	18	21	21
	Strain at Break (%)	228	265	No Break

Table 12 - Summarized high strain behavior in the P(VDF-CTFE) 78.4-21.6 mol% copolymers.

Electrical Breakdown

Electrical breakdown testing was performed using an electrostatic pull-down method. A 7 mm in diameter rounded brass button was used as an electrode. During testing, a 500 V/s ramp was applied between the button and a polymer film which was coated on only one side with gold. A diagram of the setup is shown in Figure 40. Pull-down between the uncoated polymer film side and the brass button typically happened at an electrical field of 10 MV/m and was maintained until breakdown occurred over the test area. The pull-down method was chosen over a point-contact method to avoid any mechanical force that might cause premature breakdown at the contact point.

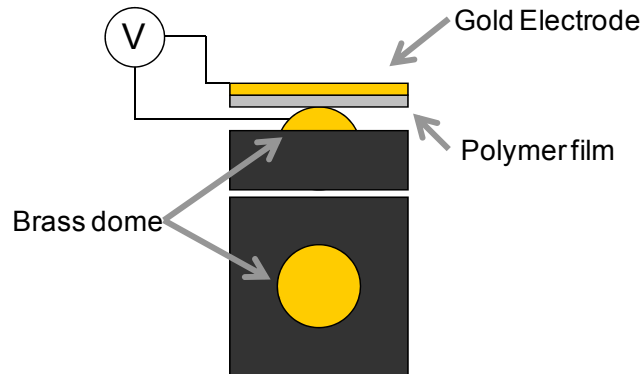


Figure 40 - Diagram of the electrostatic pull-down electrical breakdown strength testing method.

The breakdown measurements were fitted to a two-parameter Weibull distribution

$$P(E) = 1 - \exp\left[-\left(\frac{E}{\alpha}\right)^\beta\right]$$

Equation 19 - Weibull probability distribution.

where P is cumulative probability of breakdown, E is the breakdown electrical field, α is the characteristic breakdown strength which corresponds to a ~63% probability of failure, and β is the slope parameter.⁶⁴ At least 30 measurements were made for each Weibull fitting. The cumulative probability was calculated using a median ranks method for the Weibull prediction.⁶⁵

The α electrical breakdown results performed at -35°C, -15°C, and 25°C are summarized in Figure 41. The error bars represent the 90% confidence interval for the α parameter. All the Weibull plots and associated constants are listed in Appendix C. At all three temperatures, the samples' breakdown strengths increase with increasing molecular weight. Additionally, the general breakdown strengths of the samples increases with decreasing temperature. At 25°C, the primary breakdown mechanism is

hypothesized to be electromechanical and can be accurately predicted using the simple model based off a modified equation taken from Stark and Garton

$$E = \left(\frac{2\sigma_y}{\epsilon\epsilon_o} \right)^{\frac{1}{2}}$$

Equation 20 - Electromechanical breakdown equation.

where E is the electrical breakdown field, σ_y is the yield stress, ϵ is the permittivity, and ϵ_o is the permittivity of vacuum.⁶⁶ In their paper, Stark and Garton define their failure criterion from an instability that occurs when the thickness ratio, t/t_o , equals 0.6 where any increase in voltage collapses the dielectric. This term has been replaced by the yield stress of copolymers to more accurately represent the failure point since the yield strains and stresses will differ between materials. Since the force of the electrodes is compressive, the measured tensile yield stress was assumed to be directly related to the compressive yield stress for small yield strains in the elastic regime of the mechanical behavior.⁶⁷

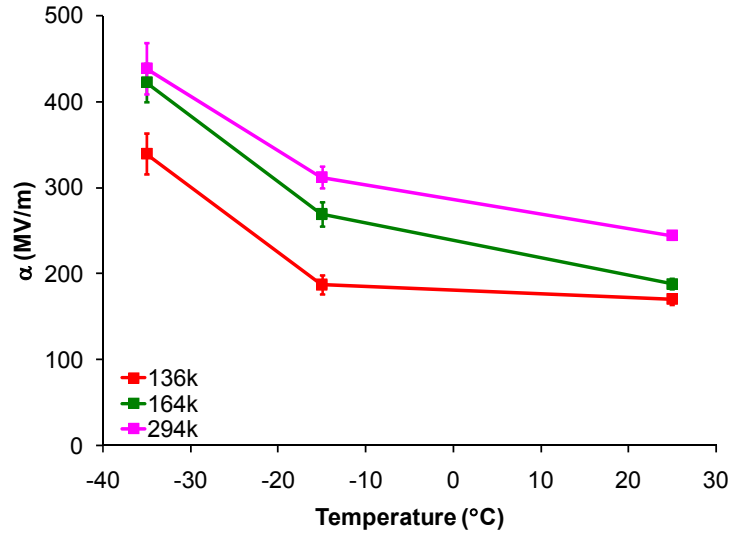


Figure 41 - Summarized α breakdown results for the P(VDF-CTFE) 78.4/21.6 mol% copolymers.

The predicted values of 180, 213, and 253 MV/m for the 136k, 164, and 294k copolymers respectively predict the actual measurements to within 13% in the worst case. The summarized calculations are shown in Table 13. The elastic modulus of the polymers at 25°C is low at ~10 MPa which makes deforming the films easy and is reflected in the observed stretching of the films during the breakdown testing. By increasing the molecular weight, the polymer's toughness and yield stress increase through physical cross-links which makes the films more resistant to the electrostatic compressive force. This increased resistance can be directly observed in the data as an increase in breakdown strength.

25°C

M_n (kg/mol)	136	164	294
ϵ_0	8.85E-12	8.85E-12	8.85E-12
ϵ	9.1	9.7	9.7
σ_y (Pa)	1.31E+06	1.94E+06	2.75E+06
Calc. E (MV/m)	180	213	253
Meas. E (MV/m)	170	188	244

Table 13 - Summarized predicted breakdown strengths based on the electromechanical model of Equation 20 at 25°C.

As the temperature is lowered further to -15°C, the simple electromechanical model no longer accurately predicts the breakdown. The model does an even worse job at the lowest test temperature of -35°C where the predicted values are an order of magnitude greater than those measured. Both of these calculations are shown in Table 14. As the polymers are cooled from 25°C to -35°C, the elastic modulus of the polymers increases from ~10 MPa to ~30 MPa to ~1500 MPa at 25°C, -15°C, and -35°C respectively. The corresponding yield stresses also increase as the temperature is lowered, though at slower rate. The increase in modulus originates from the stiffening of the chains as the polymers approach and pass through the glass transition temperature of -24°C as measured by various methods. Essentially, the samples stiffen to a point at low temperatures where the breakdown occurs before sufficient electrostatic force can yield the samples. This is also confirmed in images of the films after testing that do not show any deformation at the lower temperatures as shown in Figure 42 for the 294k copolymer.

-15°C

M_n (kg/mol)	136	164	294
ϵ_0	8.85E-12	8.85E-12	8.85E-12
ϵ	6.7	7.3	7.2
σ_y (Pa)	3.46E+06	3.52E+06	6.21E+06
Calc. E (MV/m)	342	330	441
Meas. E (MV/m)	187	269	312

-35°C

M_n (kg/mol)	136	164	294
ϵ_0	8.85E-12	8.85E-12	8.85E-12
ϵ	4.2	4.4	4.5
σ_y (Pa)	2.59E+07	2.24E+07	2.97E+07
Calc. E (MV/m)	1180	1073	1221
Meas. E (MV/m)	339	422	438

Table 14 - Summarized predicted breakdown strengths based on the electromechanical model of Equation 20 at -15°C and -35°C.

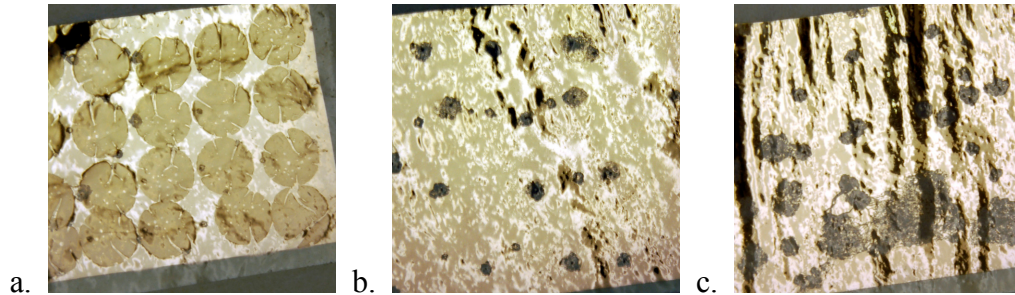


Figure 42 - Images of 294k copolymer after breakdown testing. Image dimensions are approximately 5 by 5 cm. a. 25°C; b. -15°C; c. -35°C.

The inconsistency of the electromechanical model at lower temperatures suggests the presence of another breakdown mechanism at -15°C and -35°C and is hypothesized to be thermal breakdown related, specifically impulse thermal breakdown. Impulse thermal breakdown occurs when the electrical power dissipation heats dielectric to some critical breakdown temperature and follows the heat balance

$$\sigma(T, E)E^2 = CD\left(\frac{dT}{dt}\right)$$

Equation 21 - Impulse thermal breakdown.

where the term responsible for heat dissipation to the surroundings has been set to zero for the impulse conditions from Equation 16.⁵⁶ This means that all of the generated heat is absorbed by the polymer. The conductivity of the polymers films were measured as function of temperature between -50°C to 20°C and electric fields between 0.01 MV/m to 10 MV/m. At each temperature and electric field, the sample was grounded for 10 seconds, had the electric field applied for 10 seconds, and finally grounded for 10 seconds. At least a two order of magnitude difference in the absolute measured current between these last two steps was verified before continuing with the next measurement. The currents recorded from the end of the application step were fitted to the equation

$$\sigma = \sigma_o \exp[gE + a(T - T_o)]$$

Equation 22 - Conductivity of an insulating material.

where σ is the conductivity, E is the electric field, T is the temperature, T_o is the ambient temperature, and g, a, and σ_o are constants.⁶⁸ The conductivity of the copolymers decreases as the molecular weight increases. At 0°C, the conductivities of the copolymers were 5.26, 4.06, and 2.71 pS/m for the 136k, 164k, and 294k samples respectively. The drop in conductivity with increasing molecular weight may be related to the decreasing crystallinity with increasing molecular weight where the amorphous regions are less conductive than crystalline ones. By substituting Equation 22 into Equation 21 and knowing that the voltage increases linearly with time, the resulting differential can be solved by direct integration which is shown in Appendix D. Plotting

the temperature versus electric field for the solved equation shows that the temperature remains nearly constant until a critical field where the temperature rises sharply as shown in Figure 43. This critical field was used as the thermal breakdown strength. The summarized predicted thermal breakdown values are shown in Table 15.

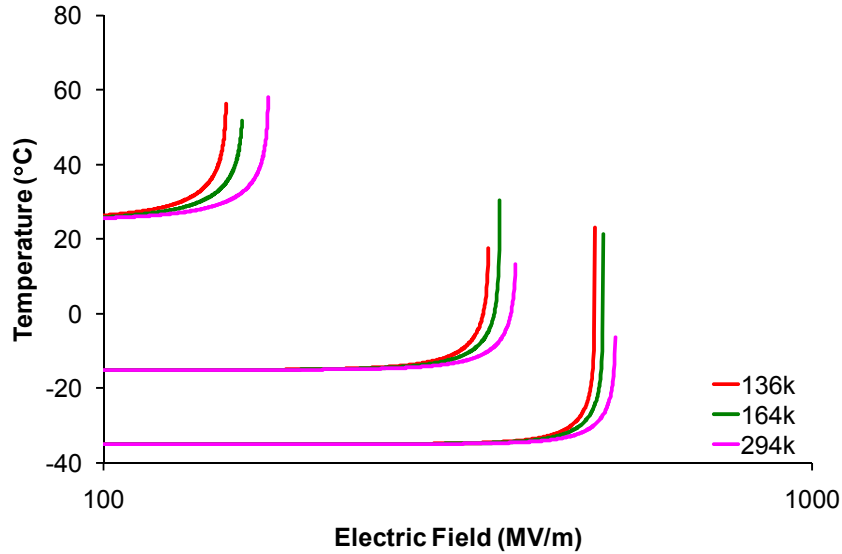


Figure 43 - Temperature versus electric field for thermal impulse breakdown.

M_n (kg/mol)	Breakdown Field (MV/m)		
	-35°C	-15°C	25°C
136k	493	349	149
164k	507	362	157
294k	528	381	171

Table 15 - Predicted values for the thermal breakdown strengths for the P(VDF-CTFE) 78.4-21.6 mol% copolymers.

Figure 44 shows the combination of all the modeled and measured data for the 294k copolymer that mirrors the other copolymers. The error bars on the experimental points represent 5th to 95th percentile of values calculated from Equation 19 using the fitted α and β parameters. The thermal model does a better job at predicting the breakdown at -35°C suggesting that breakdown is from a thermal mechanism. The

overall thermal predictions overestimate the breakdown strengths by an average of 28% compared to a 200% overestimation by the electromechanical model. At -15°C, the thermal and electromechanical breakdown models both over predict the overall measured values by an average of 50%. This could indicate that both mechanisms might be operating at this temperature where one mechanism initiates the other to produce a lower actual breakdown value. For example, thermal heating could soften the polymer which causes electromechanical failure at a field lower than expected. At -35°C, the thermal model predicts the breakdown much more accurately than the electromechanical model, but it still slightly over predicts the measured values. This discrepancy could be due to local defects in the films that could cause localized heating and lead to lower measured breakdown strengths. Finally at 25°C, the thermal model under predicts the experimental values by an overall average of 20% and falls just outside of the errors bars. The electromechanical model in comparison over predicts the breakdown by an overall average of 7% and fall within the error bars. The reason behind the low predictions for the thermal model is not fully understood and may be related to a change in the conduction behavior of the material at that starting temperature.

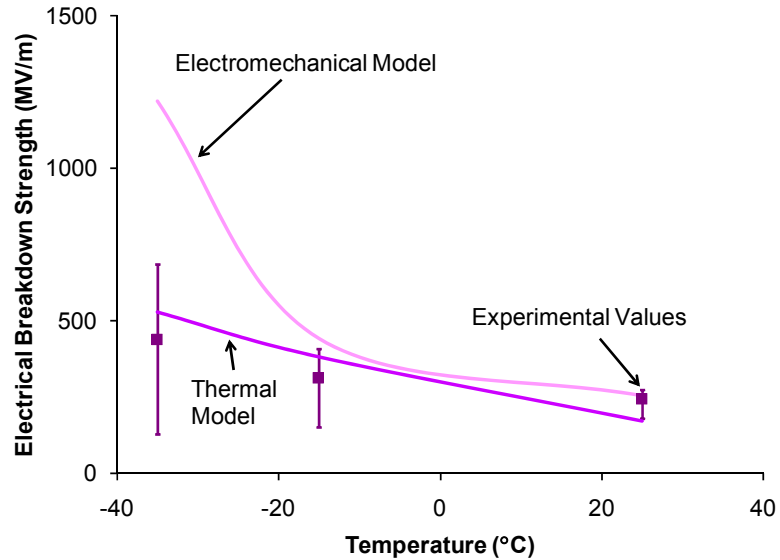


Figure 44 - Combined experimental and predicted values for the 294k copolymer.

Increasing the molecular weight of the copolymers increases the electrical breakdown strength at all the temperatures tested. At 25°C, electromechanical breakdown is the primary cause of electrical breakdown and is improved by increasing the polymers' yield stress. As the polymers are cooled to -15°C, thermal breakdown appears to also contribute the breakdown process in addition to electromechanical breakdown. At -35°C below the glass transition temperature of the polymers, thermal breakdown becomes the dominant failure mechanism and improves with lowering values of conductivity.

Energy Densities of the Copolymers

Polarization measurements on the copolymer films revealed that they behave like linear dielectric materials at high electric fields greater than 100 MV/m allowing the energy density to be calculated with Equation 14. Table 16 shows the calculated energy densities of the polymers based on the α breakdown strengths. Energy density increases

an average of 123% across all the temperatures as the molecular weight increases from 136k to 294k. Across all the molecular weights, the energy density increases an average of 77% as the temperature is lowered from 25°C to -35°C. It is interesting to note that the energy density continues to increase at lower temperatures despite the reduction in permittivity. This confirms the pivotal role that breakdown strength plays in determining the energy density.

M_n (kg/mol)	-35°C		-15°C		25°C	
	ε (1 kHz)	U (J/cm³)	ε (1 kHz)	U (J/cm³)	ε (1 kHz)	U (J/cm³)
136	3.74	1.90	5.79	0.90	8.54	1.09
164	4.27	3.36	6.66	2.13	9.86	1.54
294	3.80	3.23	6.02	2.59	8.76	2.31

Table 16 - Calculated energy densities of the P(VDF-CTFE) 78.4-21.6 mol% copolymers.

CHAPTER 4 - ELECTRICAL BREAKDOWN IN P(VDF-CTFE-TRFE) TERPOLYMERS

Introduction

Terpolymers based on vinylidene fluoride are unique materials with many potential electronic applications. Terpolymers emulate the electrical behavior of irradiated P(VDF-TrFE) copolymer by utilizing chemically bulky termonomer units to disrupt the crystallinity the same way that irradiation does without the damaging effects. Chlorine is usually the choice atom for introducing the defects into the polymers and has been shown here in this work to be very effective at changing not only the crystallinity, but also the crystal phases present in the polymer. The electrical properties of the terpolymers are equally as sensitive to the amount defects present transforming the polymers from paraelectric to ferroelectric forms and introducing non-linear electrical behavior. For linear dielectric materials, the energy density in the materials can be calculated according to Equation 13. This becomes more complicated for non-linear materials requiring the use of Equation 12 and specific details about the non-linear behavior.

In this chapter, the electrical breakdown behavior of terpolymers synthesized using the two step approach is explored. The high permittivities and breakdown strengths offer the potential for high energy densities in these materials. However, these same high permittivity materials tend to behave as non-linear dielectrics necessitating a more complicated approach towards examining the breakdown behavior, especially at high electric fields. Several terpolymers as well as a fully hydrogenated P(VDF-TrFE) copolymer were examined in order to pinpoint the origin of electrical breakdown. These

particular compositions were chosen for the electrical changes that occur at the varying hydrogenation levels in the polymers. As with the P(VDF-CTFE) in the last chapter, very little research exists on the breakdown behavior of these terpolymers. The work here seeks to add to this research by systematically studying the terpolymers as a function of their chemical composition and resulting electric properties.

Experimental Procedure

Materials

All chemicals were used as purchased without purification unless otherwise noted. Hydrogen peroxide (30 wt% aqueous solution) was purchased from Alfa Aesar. 2, 2'-azobis (2-methylpropionitrile) (AIBN), diethyl carbonate, methanol, acetone, N, N-dimethylformamide (DMF), and tri-n-butyltin hydride were purchased from Aldrich. Tetrahydrofuran (THF) was also purchased from Aldrich and dried and distilled over sodium. Ethyl hydroxyethyl cellulose was purchased from Polysciences Inc. Vinylidene fluoride (VDF) and chlorotrifluoroethylene (CTFE) were purchased from SynQuest Laboratory Inc. and purified by a freeze-thaw process.

Emulsion Polymerization of P(VDF-CTFE) Copolymer

All manipulations of gas-condense transfer were carried out with rigorous exclusion of oxygen and moisture under 10^{-6} Torr high vacuum. A 300 mL stainless steel Parr autoclave equipped with a mechanical stirrer was charged with 0.27 g of hydrogen peroxide, 0.16 g of ethyl hydroxyethyl cellulose, 0.05 mL of diethyl carbonate, and 150 mL of degassed distilled water before it was degassed further by repeated freeze-degass-thaw cycles. The reactor was then cooled and 33 g of VDF and 15 g of CTFE were

condensed into the reactor. The reactor was heated to 110°C for 3.7 hours. The unreacted monomer gases were vented and the resultant copolymer (20 g) was recovered, washed with methanol and distilled water, and dried in vacuum at 60°C for 24 hours. The resulting copolymer had a VDF content of 73.6 mol%.

Hydrogenation Reaction of the P(VDF-CTFE) Copolymer (Representative Experiment)

3.0 g of P(VDF-CTFE) copolymer and 171 mg of AIBN were mixed in a 250 mL flask. The flask was attached to a high vacuum line, degassed, and 170 mL of THF was added. After the mixture was stirred at 60°C for 30 min, 1.0 mL of tri-n-butyltin hydride was added by syringe. The solution was kept stirring for 24 hours at 60°C before it was terminated with methanol. The resulting terpolymer of P(VDF-CTFE-TrFE) was washed with methanol and distilled water, and dried in vacuum at 60°C for 24 hours. Further purification was performed by Soxhlet extraction with hexane. There was no signal from tri-n-butyltin hybrid or similar compounds in the ¹H NMR spectra after purification. The composition of the resulting terpolymer was determined by ¹H NMR to be P(VDF-CTFE-TrFE) 73.6/9.2/17.2 mol%.

Film Preparation

All polymer films were prepared by solution casting from DMF onto glass slides. The polymer solutions were filtered through 0.45 μm poly(tetrafluoroethylene) syringe filters before casting to remove any particulates. The films were dried at 60°C overnight followed by heating at the same temperature under vacuum for 24 hours for complete solvent removal. Free-standing films were created by soaking coated glass slides in distilled water and carefully peeling off the films which were 20 μm thick.

Characterization

Sixty nanometer thick gold electrodes were sputtered onto the films for electrical testing. Dielectric testing was performed using an Agilent LCR meter (E4980A). A Trek Model 30/20 \pm 30 kV High Voltage Amplifier System was used for electrical breakdown testing with a 500V/s ramp rate. All high voltage testing was performed in Galden HT which is a highly insulating, perfluorinated polyether fluid. Electrical displacement measurements were made using a Sawyer-Tower circuit at 10 Hz with a bipolar field.⁶⁰ Mechanical properties were measured on a TA Instruments DMA 2980 dynamic mechanical analyzer (DMA) using a linear force ramp. Thermal property measurements were carried out with a TA Q100 instrument at a heating rate of 10°C/min. Infrared spectra were recorded using a Nicolet FT-IR spectrometer with 64 scans averaged at a resolution of 2 cm⁻¹. Wide-angle x-ray diffraction (WAXD) studies were performed using a Scintag Cu-K _{α} diffractometer with a x-ray wavelength of 1.54 Å. Absolute molecular weight was measured by size exclusion chromatography using DMF as the mobile phase on a Viscotek TDA 302 triple detector. NMR was performed on a Bruker AM-300 spectrometer instrument.

Results and Discussion

Dielectric Properties

Figure 45 shows the permittivities of the polymers measured at 25°C from 20 Hz to 2 MHz. All of the polymers display the same decreasing trend of permittivity with increasing frequency that is related to the relaxation of the dipolar contribution at higher frequencies. Even with the decreasing trend, all the samples' permittivities remain

relatively flat through 100 kHz before decreasing significantly. The polymers with higher permittivities have a sharper drop-off at high frequencies because of the larger contribution of ferroelectric and dipolar polarization to the overall permittivity. For fixed frequencies, the terpolymers have higher permittivities than the copolymer with the 9.2 and 11.9 mol% TrFE samples having the highest overall values. At these compositions, the polymers behave like relaxor ferroelectrics which is the origin of their high permittivities.⁴⁰ The large chlorine atom on the CTFE monomer serves as a crystal defect which disrupts the formation of large polar crystals in favor of smaller, nanosized ones surrounded by an amorphous matrix. The resulting smaller polar crystals are more mobile and increase the polarization response and overall permittivity. The 3.9 mol% TrFE polymer's low permittivity is due to a low amount of ferroelectric crystals from its small crystallinity. On the opposite end, the 18.3, 19.3, and 26.4 mol% TrFE polymers low permittivities are due to their high crystallinities and the restricted mobility of the dipolar crystals to the electric field. This restricts the total polarization of the polymers.

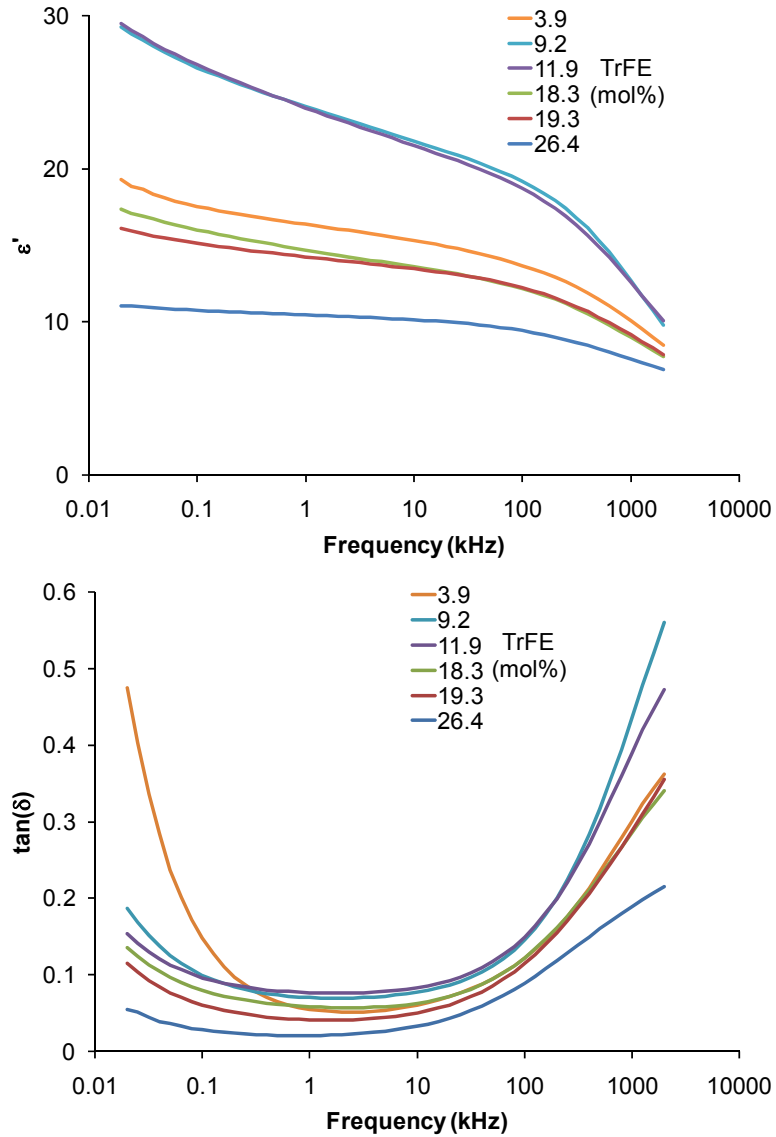


Figure 45 - Low electric field dielectric properties of the 73.6 mol% polymers.

The corresponding loss tangents of the polymers remain flat between 100 Hz and 10 kHz with sharp increases above and below this range. The increase above 10 kHz is related to the ferroelectric and dipolar relaxation where the slope of the line is greater for the higher permittivity samples. The increase at low frequencies is most likely related to the relaxations associated with melting in the polymers and decreases as the melting temperature of the polymers increases.

Crystal Structure

Wide-angle x-ray diffraction measurements were carried out to examine the evolution of the crystalline structures of the polymers with varying chemical composition. By substituting the hydrogen with bulky chlorine atoms, the crystal phases of the polymers changes from the β phase for the 26.4 TrFE mol% copolymer, to a mixture of α and γ phases for the compositions between 9.2 and 19.3 TrFE mol%, and finally to the α phase for the 3.9 and below TrFE mol% terpolymer as shown in Figure 46. Also shown in Table 17 is the quantitative degree of crystallinity (χ_c), assessed from the area of the diffraction peaks and the amorphous halo, which decreases from 35.4% to 7.2% between TrFE and CTFE copolymers respectively. This illustrates the structural defect role that CTFE plays in disrupting the overall crystal structure as its amount is increased in the polymers.

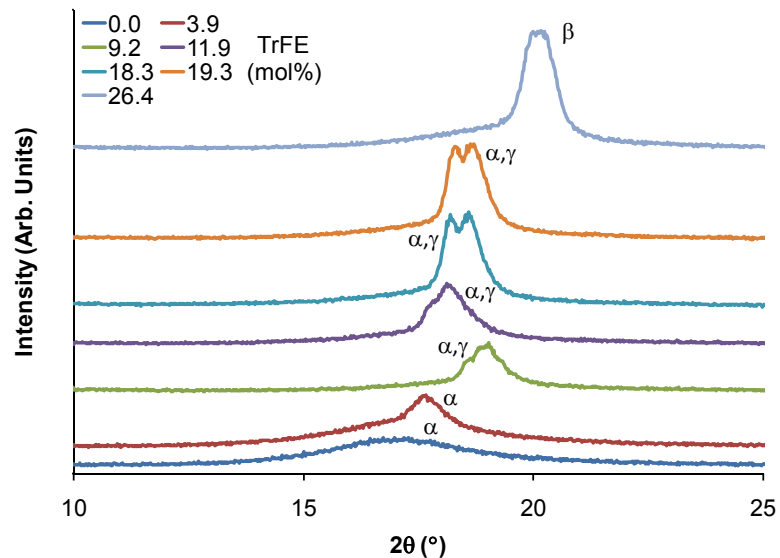


Figure 46 - Diffraction pattern of the 73.6 mol% VDF polymers with varying hydrogenation levels.

VDF	CTFE (mol%)	TrFE	χ_c (%)	Crystal Phase, 2θ ($^\circ$), Plane Reflection
73.6	26.4	0.00	0.0	α , ~ 17 , (100) almost completely amorphous
73.6	22.5	3.90	14.4	α , 17.7, (100)
73.6	17.2	9.20	17.1	α , 18.5, (020); γ , 19.0, (002)
73.6	14.5	11.9	18.0	α , 17.8, (100); γ , 18.1, (020)
73.6	8.10	18.3	24.2	α , 18.7, (020); γ , 18.2, (020)
73.6	7.10	19.3	28.6	α , 18.7, (020); γ , 18.2, (020)
73.6	0.00	26.4	35.4	β , 20.2, (200, 110)

Table 17 - Crystallinity and crystal phase peaks for the 73.6 mol% VDF polymers.

The role of the CTFE unit in modifying the crystal phases was further clarified by Fourier transform infrared (FTIR) spectroscopy. The characteristic absorbance bands at 1290 cm^{-1} and 614 cm^{-1} are associated with the trans conformation sequences greater than 4 ($T>4$) in length and trans gauche sequences (TG) respectively. The bands at 505 cm^{-1} are also associated with trans gauche sequences, but the trans sequences are repeated three times before the gauche twist ($TTTG^+TTTG^-$). The three bands, 1290 , 614 , and 505 cm^{-1} are used to calculate the relative fractions of the β , α , and γ crystal phases respectively in the polymers as a function of composition. As presented in Figure 47, the $TTTG^+TTTG^-$ and TG conformations in the γ and α phases are steadily converted to the all-trans conformation of the β -phase as more TrFE is incorporated into the polymer. These changes in crystal phase and overall crystallinity influences the dielectric properties of the polymers. The lower permittivity of the polymer with 3.9 mol% TrFE is attributed to both the low crystallinity and presence of the non-polar α phase. On the opposite end of composition, the lower permittivities of the 19.3 and 26.4 mol% TrFE copolymers is attributed to a high crystallinity which restricts dipole movement and its contribution to polarization despite the presence of polar γ and β phases. At an intermediate amount of TrFE and CTFE for the polymers with 9.2 and 11.9 mol% TrFE,

the right combination of crystallinity and polar crystal phases gives these materials high permittivities due the presences of small polar domains that respond readily to the applied electric field.

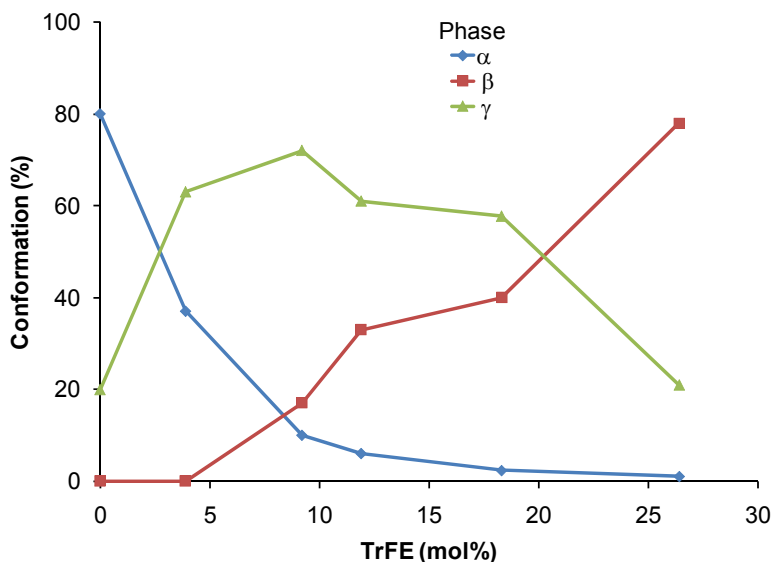


Figure 47 - Conformation as measured by FTIR for the 73.6 mol% VDF polymers.

Thermal Properties

Differential scanning calorimetry (DSC) studies also confirmed the crystallinity trend seen in the WAXD crystal data. Table 18 lists the melting temperatures and enthalpies of the polymers along with the crystallinity calculated from the WAXD data. As the amount of TrFE increases in the polymers, the melt temperatures increase from 37.8 to 163°C for the 3.9 and 26.4 mol% TrFE polymers respectively. Enthalpies also increase from 1.9 to 23.6 J/g for the 3.9 and 26.4 mol% TrFE polymers respectively. This again illustrates the defect nature of CTFE on the crystal formation in the polymers.

VDF	CTFE (mol%)	TrFE	χ_c (%)	T_m (°C)	ΔH_m (J/g)
73.6	22.5	3.9	14.4	37.8	1.9
73.6	17.2	9.2	17.1	72.5	6.6
73.6	14.5	11.9	18.0	86.7	8.9
73.6	8.1	18.3	24.2	121	13.6
73.6	7.1	19.3	28.6	127	12.6
73.6	0.0	26.4	35.4	163	23.6

Table 18 - Thermal properties of the 73.6 mol% VDF polymers.

Mechanical Properties

The stress versus strain relationships for select polymers were measured with the yield stress (σ_y) and modulus (Y) values shown in Table 19. The modulus of the polymers was calculated from the slope of the elastic regime while the yield stress was calculated from the intersection of the tangent lines of the elastic and inelastic regimes. The yield stress increases with the amount of TrFE and peaks with the 19.3 mol% sample before slightly decreasing with the fully hydrogenated sample. This same trend is observed with the modulus with a peak value obtained for the 19.3 mol% TrFE sample. All the polymers were synthesized using the emulsion method in order to obtain a high molecular weight and optimal mechanical properties. The polymers' absolute weight average molecular weight was 240 kg/mol with a polydispersity of 3.40. Despite having a higher overall crystallinity, the 26.4 mol% TrFE sample consistently had a lower yield stress and modulus than the 19.3 mol% polymer. Optical microscope images with and without crossed-polarizers of the two polymers revealed different microstructures between them and are shown in Figure 48. Both samples have a random arrangement of crystals, but the crystals are noticeably larger in the 26.4 mol% sample which has a large grained appearance. This microstructure change could be the origin of the different high

strain mechanical properties where the smaller grained sample requires more force for deformation.

VDF	CTFE (mol %)	TrFE	Y (MPa)	σ_y
73.6	22.5	3.9	8.62	1.10
73.6	17.2	9.2	58.0	3.40
73.6	7.1	19.3	414	14.7
73.6	0.0	26.4	207	10.5

Table 19 - Summarized mechanical properties of the 73.6 mol% VDF polymers.

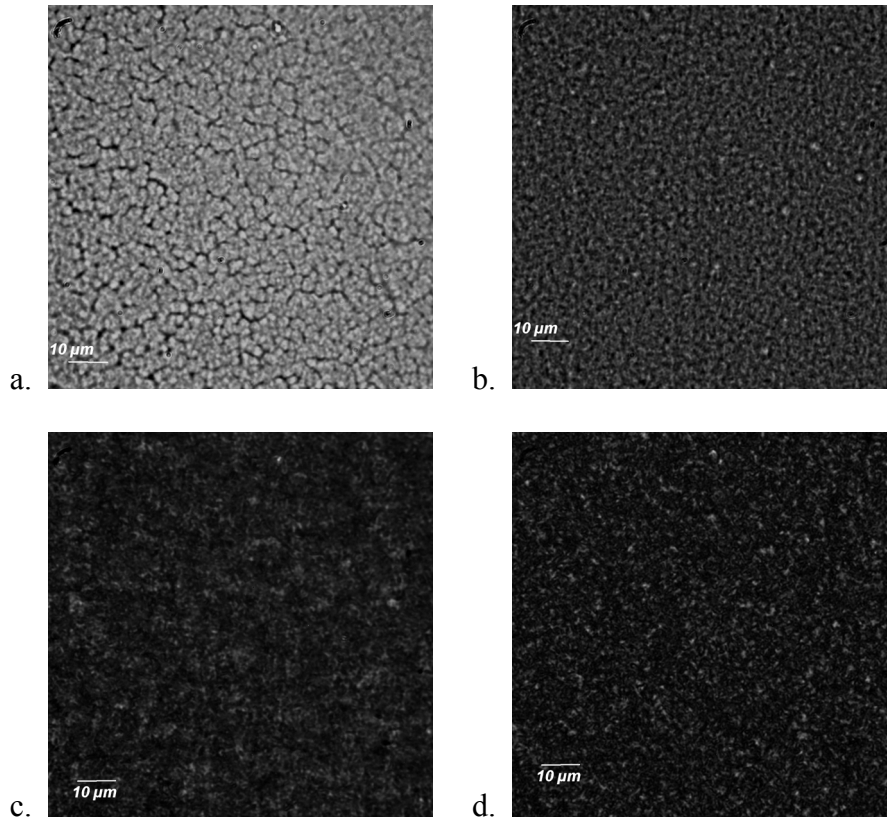


Figure 48 - Optical microscope images of polymers from the 73.6 mol% polymers. a, c - 26.4 mol% TrFE without and with crossed polarizers respectively. b, d - 19.3 mol% TrFE without and with crossed polarizers respectively.

Electrical Breakdown

An electrostatic pull-down method was used for electrical breakdown testing in order to minimize the contact force on the polymer samples. A two-parameter Weibull

distribution was used to analyze the electrical breakdown results.⁶⁴ At least fifteen data points were collected for each sample from which the characteristic breakdown strength (α) and the slope parameter (β) were calculated according to Equation 19. The complete Weibull plots and values are shown in Appendix E. The measured electrical breakdown strengths of the polymers tested at 25°C and a ramp rate of 500 V/s are shown in Figure 49 where the breakdown strengths increase with the amount of TrFE in the polymers. The error bars represent the 5th through 95th percentile of values calculated according to Equation 19 from α and β . The data for the CTFE copolymer was left out due to irregular data most likely due to its amorphous nature. The β of the samples also increases with the mol% of TrFE showing that the distribution of breakdown values become more narrowly distributed about α .

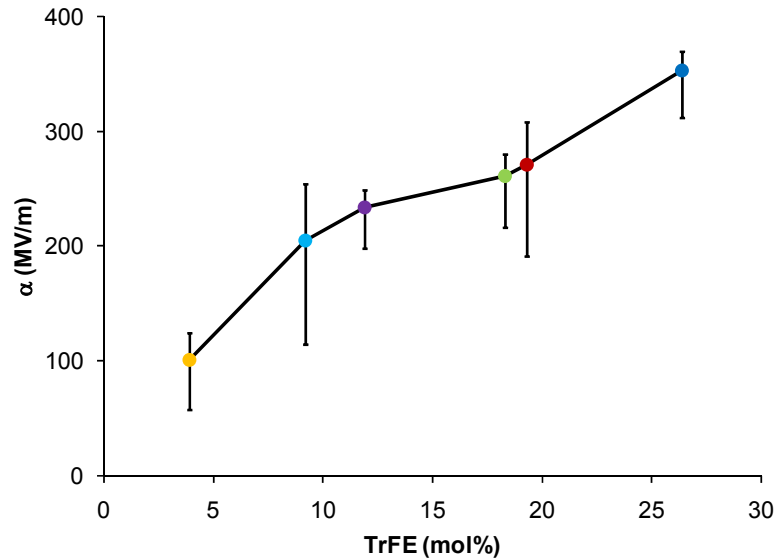


Figure 49 - Measured electrical breakdown strengths of the 73.6 mol% VDF polymers at 25°C.

The breakdown is hypothesized to be electromechanical for the polymers.

Electromechanical breakdown occurs when the electromechanical stress placed on the

film exceeds the polymers' yield stress causing a rapid collapse of the electrodes inward and electrical discharge.⁵⁷ The criterion for breakdown can be represented by

$$\sigma_y = \sigma_{EM}$$

Equation 23 - Electromechanical breakdown criterion.

where σ_y is the polymer yield stress and σ_{EM} is the total electromechanical stress. The electromechanical stress is composed of two components and is represented by

$$\sigma_{EM} = \sigma_{MW} + \sigma_E$$

Equation 24 - Component stresses of the electromechanical stress.

where σ_{EM} is the electromechanical stress, σ_{MW} is the Maxwell stress, and σ_E is the electrostrictive stress. The Maxwell stress originates from the Columbic attraction of the electrodes and is present for all capacitors. For the polymers used here, it can be calculated from the equation

$$\sigma_{MW} = \int \frac{q dE}{A}$$

Equation 25 - Electrostatic Maxwell stress.

where σ_{MW} is the Maxwell stress, q is charge, E is electric field, and A is area. The full derivation of Equation 25 is shown in Appendix F. Since some of polymers used here have non-linear polarization responses at high electric fields, it was necessary to measure the electric displacement for all the samples to make this calculation accurately.

The electrostrictive stress defined here is simply the sum of all the electrostriction in the material outside the Maxwell stress which can include contributions from the converse piezoelectric effect. The strain from this latter effect is usually less than 0.1%

and only relevant on electrically poled materials and will be ignored here.⁶⁹ The electrostrictive stress of P(VDF-TrFE) and P(VDF-CTFE-TrFE) polymers is a materials response that originates from a crystal phase change under an electric field where the unit cell changes dimension.^{70,71} This dimension change usually coincides with a crystal phase change such as a paraelectric to ferroelectric transition and is always a compressive force. Table 20 illustrates the density change between the α , γ , and β crystal forms that can occur under high electric fields. The electrostrictive strain responses of P(VDF-TrFE) and P(VDF-CTFE-TrFE) polymers have been previously explored and been found to follow the relationship

$$S_{EM} = QD^2$$

Equation 26 - Electromechanical strain response.

where S_{EM} is the electromechanical strain, Q is the electrostrictive coefficient, and D is the electric displacement.^{69,72,73} Typically in the literature, Equation 26 is referred to as the electrostrictive strain and includes both the Maxwell and electrostrictive strain components related to Equation 24. To stay consistent with the definition presented here, it will be called the electromechanical stress and represented by

$$\sigma_{EM} = YQD^2$$

Equation 27 - Electromechanical stress.

where σ_{EM} is the electromechanical stress and Y is the modulus. In order to simplify the analysis of this quantity, the effects of remnant polarization and the resulting remnant strain and stress were ignored and assumed to be negligible. The electric displacement measurements used for this calculation are shown in Figure 50 and set initially to zero.

The relationship becomes non-linear for 19.3 and 26.4 mol% TrFE polymers above electric fields of 100 and 75 MV/m respectively. In these non-linear regions, a logarithmic fit was used to estimate the displacement at higher fields.

	α	γ	β
a	4.96	4.96	8.58
(Å) b	9.64	9.67	4.91
c	4.62	9.20	2.56
Density Relative to α	-	+0.212	+2.33

Table 20 - Density change between the α , γ , and β crystal unit cells.

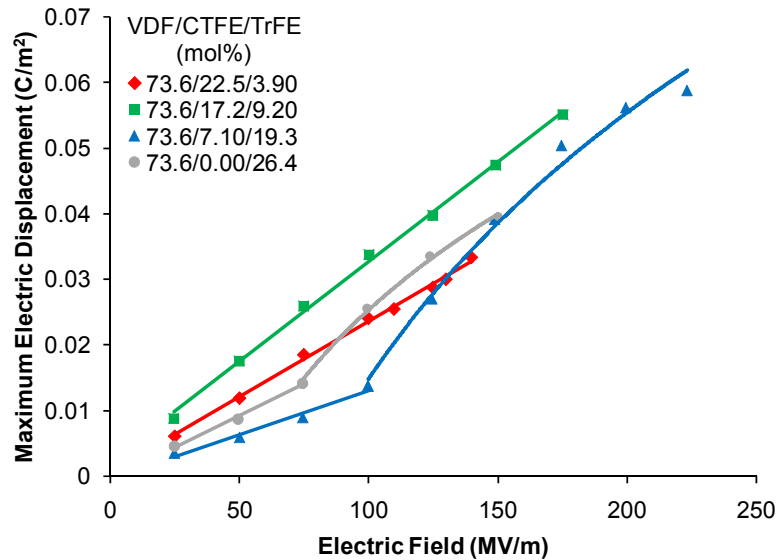


Figure 50 - Electric displacement versus electric field for the 73.6 mol% VDF polymers.

Table 21 shows the calculated breakdown strengths, which have good agreement to the measured values with an average error of 14%. In the 3.9 mol% TrFE sample, only the Maxwell stress was used to calculate the breakdown strength. Since the polymer has a low crystallinity and a low modulus, it is expected that the electrostrictive contribution to the electromechanical stress will be minimal. This is illustrated by the accuracy of the prediction calculated from only Equation 25. As the TrFE is increased to 9.2 mol%, the

Maxwell contribution alone underestimates the breakdown strength resulting in the least accurate of all the predictions. It is suspected that at this composition, the electrostrictive contribution begins to have a noticeable effect as the sample becomes more crystalline and ferroelectrically active. Unfortunately, an estimate for this electrostrictive contribution was not possible due to a lack of an electrostriction coefficient in the literature for that particular chemical composition.

VDF (mol %)	CTFE (mol %)	TrFE (mol %)	E_b (MV/m)		σ_y (MPa)	σ_E (MPa)	σ_{MW} (MPa)
			Measured	Calculated			
73.6	22.5	3.9	101 (± 3.14)	93.9	1.10	-	1.10
73.6	17.2	9.2	205 (± 6.65)	148	3.40	-	3.40
73.6	7.1	19.3	271 (± 5.22)	249	14.7	7.83	6.87
73.6	0.0	26.4	353 (± 2.41)	406	10.5	3.61	6.89

Table 21 - Experimental and calculated electric breakdown field for the 73.6 mol% VDF polymers.

For the 19.3 and 26.4 mol% TrFE samples, the predicted strengths match very well to the measured values by solving for the electric field in Equation 27 since D is a function of E and substituting the yield stress and the appropriate values from the literature.^{73,74} The exact values that were used are listed in Appendix G. It's interesting to note that predictions remain accurate despite the differences in yield stresses between the polymers. Both have identical Maxwell stresses illustrating that the electric displacements of the samples are similar despite the different breakdown fields. The high displacement and therefore Maxwell stress in the 19.3 mol% sample is typical of relaxor ferroelectrics which tend to polarize easily at lower electric fields.⁵⁹ However, the 19.3 mol% sample has nearly twice the electrostrictive response than the 26.4 mol% sample. The small amount of CTFE in the 19.3 mol% sample breaks up large ferroelectric domains resulting in a mixture of paraelectric and ferroelectric domains as shown by the

earlier WAXD and FTIR measurements. Under an electric field, the paraelectric domains as well as chains in the amorphous regions transform to ferroelectric domains which gives the relaxor its large electrostriction. The 26.4 mol% sample contains a much lower paraelectric and amorphous content limiting its electrostriction. Thus for relaxor ferroelectric polymers, the electrostrictive component produces a significant contribution to the electromechanical stress over normal ferroelectric polymers. In the case of the 19.3 mol% sample, this increased stress lowered its breakdown strength despite its favorable mechanical properties.

Energy Density

The measured energy densities (U) of the polymers at their α breakdown strengths are shown in Figure 51. Energy density increases from 1.10 to 6.89 J/cm³ for the 3.9 to 26.4 mol% TrFE polymers respectively as TrFE is increased. Between the 3.9 to 19.3 mol% TrFE polymers, a 170% increase in breakdown strength translates to a 600% increase in energy density. The 19.3 and 26.4 mol% TrFE polymers have identical energy densities despite a 30% higher breakdown strength in the TrFE copolymer. The reason for the similarity in energy densities despite the breakdown strength differences lies in the high polarization response and resulting electric displacement of the 19.3 mol% TrFE terpolymer at lower electric fields. As seen in Figure 50, the displacement of the terpolymer overtakes the TrFE copolymer at a field of 150MV/m. Extrapolated to their breakdown strengths, the two polymers have similar electric displacements which results in a similar energy density.

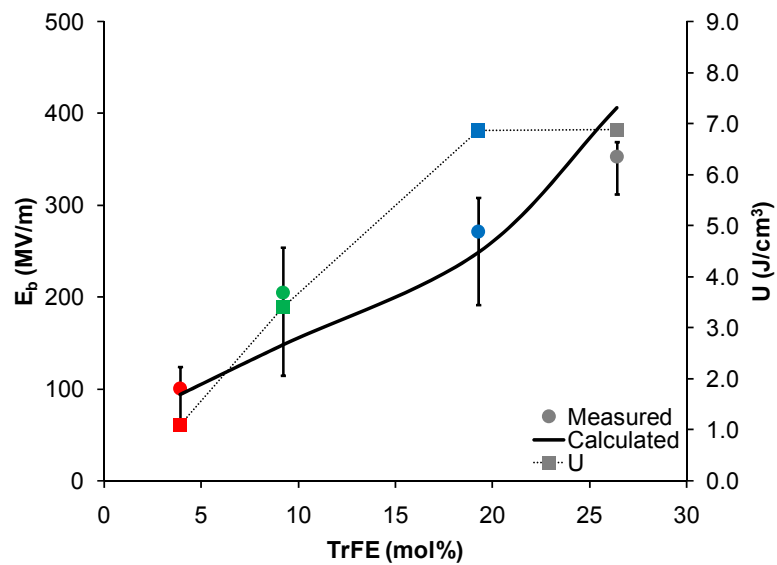


Figure 51 - Energy density, and experimental and measured breakdown strengths for the 73.6 mol% VDF polymers.

CHAPTER 5 - ELECTRICAL ENERGY STORAGE IN SiO_2 -P(VDF-CTFE) HYBRID MATERIALS

Polymer Composite Dielectrics Review

Composite materials attempt to improve the properties of the overall material by exploiting the best properties of the individual components. This approach has been applied to dielectrics to produce superior performance for various properties. A significant amount of research in this area has focused on the application of dielectrics as electrical insulation for high voltage applications.⁷⁵ Polyethylene is the choice material for this application and is typically blended with different additives to improve properties like ultraviolet light resistance while maintaining similar electrical breakdown resistance.⁷⁶ The additives in this case are usually titanium dioxide or carbon black. Two strategies can be identified for enhancing the polarization and energy density of polymer composite capacitor dielectrics. The first increases the permittivity of the composites by incorporating high permittivity particles into the low permittivity polymer while attempting to maintain an electrical breakdown strength similar to the neat polymer.⁷⁷ The second strategy increases the breakdown strength of the composite material while at least maintaining the permittivity of the neat polymer through the incorporation of low permittivity particles.⁷⁸ According to Equation 14, both strategies potentially could lead to improvements in the energy density by increasing the permittivity or electric field.

Increasing the permittivity of a polymer composite is a relatively easy task and has been accomplished in a variety of ways. Incorporation of high permittivity particles, either on the micro or nanometer size scale is a popular method. A number of mixing rules can be used to approximate the composite permittivity based on the individual

components.^{79,80} As mentioned before, most polymers are low permittivity materials with values ranging from 2-4 as shown in Table 1 for a variety of popular capacitor dielectrics making increasing the permittivity fairly easy with most other materials. Ceramic particles, especially ferroelectric particles, are good choices since their permittivities are typically several orders of magnitude greater than polymers. Reports on the addition of barium titanate, titanium dioxide, aluminum oxide, and zirconium oxide demonstrate composite permittivity increases up to two orders of magnitude greater than the matrix polymer as a function of fill volume.^{77,81,82,83} Metallo-organic molecules containing a transition metal coordinated with organic groups have also been used to produce similar increases in permittivity.⁸⁴ This latter strategy allows the composite to maintain mechanical properties closer to the matrix polymer compared to using a ceramic filler.

However, these gains in the composites' permittivity are usually accompanied by decreases in electrical breakdown strength compared to the neat matrix which negates any potential increase in energy density. When high permittivity inclusions are added to a low permittivity matrix, distortions in the local electric fields around the particles occur in composite.^{85,86,87} The average electric field applied between the two electrodes of the material can be significantly enhanced locally resulting in a heterogeneous field distribution. If the enhancement occurs over a region of the composite where either the particle or matrix has a low breakdown strength, local breakdown can occur which will eventually cascade to complete electrical breakdown. Thus a competing effect occurs in the composite. Increasing the contrast in permittivity between the particle and matrix increases composite permittivity, but it also enhances the local electric field distortions which reduces breakdown strength. Alternatively, the distortions can be reduced by

decreasing the permittivity contrast and increasing the fill amount of particles in the composite to compensate for the lower permittivity particles. However, this route also results in a lowering of breakdown strength as the percolation threshold is approached.⁸⁸ Breakdown strength decreases due to the formation of channels where conduction can occur between the electrodes. In summary, using high permittivity composites for increasing energy density has not been successful, limiting these materials to low electric fields applications.

Polymer composites can also show increases in breakdown strength over the neat matrix polymer as another way of increasing the energy density. This is new area of research where the origins of these increases are not well understood. As stated before, composites typically are made from inorganic particles of micro and nanometer dimensions with various geometries. Composites containing micrometer sized particles almost always show decreases in electrical breakdown strength compared to the neat matrix polymer.^{89,90} Breakdown is usually attributed to partial discharge and free volume breakdown in these materials where the matrix and particles don't create homogeneous interfaces. The large particles can also readily form percolation channels if the thickness of the dielectric is on the same size scale as the particles. Other electrical properties such as electrical resistivity are found to increase in the microcomposites and can be linked to thermal breakdown mechanisms as the particles create conduction paths in the material. Changing the particles to nanometer sizes can alter the breakdown strength over the neat matrix polymer in either direction. Reports of nanoparticle composites decreasing, increasing, or maintaining breakdown strength all have been reported in the literature

necessitating careful examinations of these papers and the mechanisms behind the behavior in order to exploit the breakdown enhancing properties.^{89,91,92}

In examining nanocomposites, common themes become apparent towards enhancing breakdown strength. The first is creating a good dispersion of particles which determines whether the composites are true nanocomposites. Aggregation of the nanoparticles can turn them into microparticles and bring with them the same problems of microcomposites. Dispersal of nanoparticles can be enhanced by modification of the particle surface with ligands that create steric repulsion.⁹³

Controlling the nature of the interface between the nanoparticles and matrix is also an important variable. As the size of the particles decreases from the micro to nanoscale, the surface area for a constant volume loading of particles can increase two orders of magnitude.⁷⁸ The interface is the critical feature of the nanocomposites which has a large influence over its properties. It is believed that the interface around a nanoparticle can affect the surrounding matrix material up to a distance on the order of the diameter of the particle. This is basis of a ‘multi-core’ model which has been theorized by several authors in various ways for describing these extended effects.^{85,94} The models consist of at least two layers which start at the particle surface and extend into the matrix. The first layer is a bonded or bound layer depending on the chemical nature at the interface where the matrix polymer can be tightly bound to the particle and takes on certain properties different from the bulk matrix. Polymer conformations in this region can be altered through manipulation of the particle surface where variables such as surface energy and affinity come into play. The second layer is a loose layer where the matrix polymer still feels some effect of the interface to have its properties changed, but

is more similar to the matrix than the previous layer. The third layer is superimposed over the first two layers and consists of an electric double layer that results from charge exchange that can occur depending on the surface nature of the particle. This is controlled through the surface chemistry of the particles. The first layer is considered to have a thickness around a nanometer or a few atoms thick. The second layers' thickness is slightly larger at several nanometers thick while the third electric double layer can exert an influence up to several tens of nanometers away depending on its strength. While the nanoparticles are physically small, they can behave as though they were much larger particles and change the properties of the composite at lower loadings than their size would suggest.

Returning back to breakdown strength, small loadings of well dispersed nanoparticles both increase and decrease this value depending on the modification. Simple treatments such as thorough drying to remove bound water can improve a nanocomposites' breakdown strength to that of the neat polymer.⁹⁰ More exotic treatments involving surface modification by covalently bonding surface groups can increase the breakdown strength as a function of the group.⁷⁸ While breakdown strength isn't always improved for nanocomposites, other related phenomenon such as voltage endurance which is related to electrical degradation can be improved orders of magnitude which is important from a reliability standpoint. Improvements for breakdown strength and endurance have been linked to increases in crystallinity due to a crystal nucleation effect, increased resistivity due to the creation of more torturous paths for conducting species, and reduced space charge formation from the creation of trap sites. Controlling

the nature of conduction and the charged species seems to be the key for improving electrical breakdown strength in composites.

In this chapter, the electrical breakdown properties of hybrid materials based on silica dioxide and P(VDF-CTFE) are presented and the nature of the breakdown mechanisms are explored. While traditional nanocomposites are created by physically blending the particles into the matrix, an unconventional approach will be presented where the particles are created in-situ within the matrix. As will be shown, this procedure produces well dispersed composites with interesting electrical breakdown behavior and high energy densities.

Experimental

Materials

All reagents were purchased from Aldrich and used without further purification unless otherwise noted. Tetrahydrofuran (THF) was distilled from sodium benzophenone ketyl under nitrogen. Vinylidene fluoride (VDF) and chlorotrifluoroethylene (CTFE) were purchased from SynQuest Laboratory Inc. and purified by a freeze-thaw process prior to use.

Solution Polymerization of Triethoxysilyl Terminated P(VDF-co-CTFE) Copolymer

All manipulations of gas-condense transfer were carried out with rigorous exclusion of oxygen and moisture on a dual-manifold Schlenk line with 10^{-6} Torr high vacuum. Triethoxysilyl-benzoyl peroxide (400 mg, 0.71 mmol), produced using a procedure similar to a previously published method, and 30 mL of anhydrous acetonitrile were added into a 70 mL Parr reactor with a magnetic stirrer.⁹⁵ Vinylidene fluoride (27.5

mL, 0.29 mol) and chlorotrifluoroethylene (2 mL, 0.024 mol) were transferred and condensed at liquid nitrogen temperatures through a high vacuum line with a vacuum level of 1 millitorr. The Parr reactor was submerged in an oil bath and heated to 90°C for 6 hours. The reaction was stopped and the residual gases were discharged. The acetonitrile was removed under reduced pressure. The P(VDF-CTFE) copolymer was washed by 2 × 20 mL of anhydrous CH₂Cl₂ and dried under vacuum to give 3.5 g P(VDF-CTFE) copolymer as a white powder. The final copolymer had a VDF and CTFE content of 88.0 and 12.0 mol% respectively. The number average molecular weight calculated from NMR data was 50 kg/mol.

Film Preparation

Cleaned glass slides that were used for casting were immersed in a 0.02 M octyltrichlorosilane (OTS) toluene solution for 10 min at room temperature under dry argon. The physically adsorbed octyltrichlorosilane molecules and the oligimers resulting from the autocondensation of octyltrichlorosilane molecules were removed by washing using methanol. The modified glass slides were dried under argon flow and stored in a desiccator. 200 mg of copolymer was dissolved in anhydrous DMF solution and stirred for 24 hours. Tetraethyl orthosilicate (TEOS), acetic acid, and water were then added to the solution and stirred for 48 hours. The solution was casted on the OTS modified glass slide and dried at 55°C for 24 hours. The films were released from the substrates by soaking in distilled water overnight. Under vacuum, the released films were heated on Teflon sheets at 70°C for 12 hours, 90°C for 4 hours, 110°C for 4 hours, 130°C for 4 hours, and 150°C for 48 hours and cooled to room temperature in that order

to produce the final films. The final films were transparent with a film thickness of approximately 20 micrometers.

Characterization

Sixty nanometer thick gold electrodes were sputtered onto the films for electrical testing. Dielectric testing was performed using an Agilent E4980A LCR meter. Temperature varying dielectric properties were made using a Hewlett Packard 4284A LCR meter in conjunction with a Delta Design Oven model 2300. Thermally stimulated discharge current (TSDC) measurements were made with a Hewlett Packard 4140B pA meter / DC voltage source with a Delta Design oven and a Kepco Model BOP 1000M high voltage source. Electrical breakdown was performed using a Trek Model 30/20 \pm 30 kV high voltage amplifier system with a 500 V/s ramp rate. Breakdown testing was conducted in Galden HT which is a highly insulating, perfluorinated polyether fluid. Electrical displacement measurements were made using a Sawyer-Tower circuit at 10 Hz with a unipolar field.⁶⁰ Mechanical properties were measured on a TA Instruments DMA 2980 dynamic mechanical analyzer (DMA) using a linear force ramp. Thermal property measurements were carried out with a TA Q100 instrument at a heating rate of 10°C/min. Wide-angle x-ray diffraction (WAXD) studies were performed using a Scintag Cu-K α diffractometer with a x-ray wavelength of 1.54 Å. NMR was performed on a Bruker AM-300 spectrometer instrument. Transmission electron microscopy (TEM) was performed on a JEOL EM-2010F. Elemental analysis was performed on FEI-Philips XL-20 scanning electron microscope (SEM) equipped with an energy dispersive spectrometer.

Results and Discussion

Synthesis of SiO₂-P(VDF-CTFE) Hybrid Materials

The silica in the hybrid materials presented in this chapter were produced through an in-situ process where the particles were formed within the film during processing rather than separate discrete mixing of particles. The center piece of the process is the functionalized copolymer whose synthetic scheme is shown in Figure 52. The polymerization utilizes a functionalized initiator of triethoxysilyl-benzoyl peroxide where the triethoxysilyl groups become the terminating end groups due to a radical coupling reaction that occurs in the copolymer synthesis termination step.⁹⁵

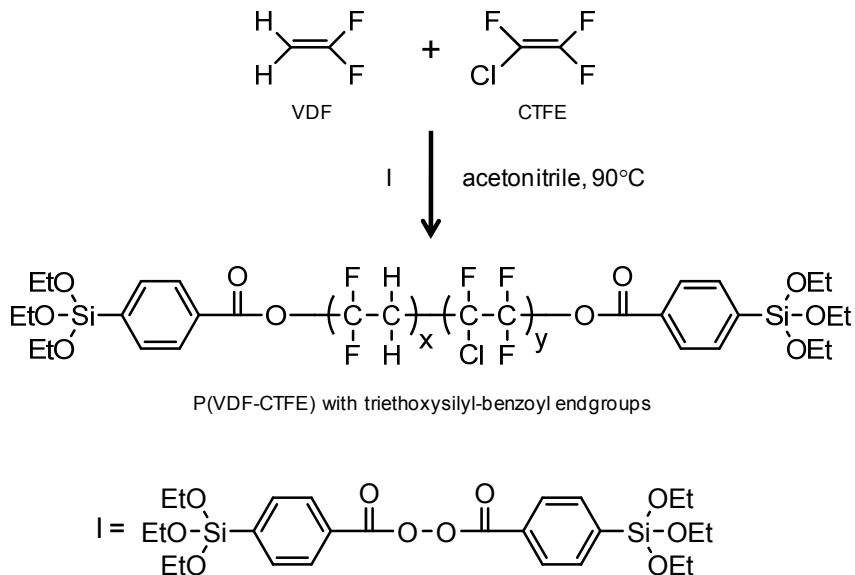


Figure 52 - Synthetic scheme for the triethoxysilyl-benzoyl functionalized copolymer.

To produce the SiO₂ particles in the material, a sol-gel process was used which contained two steps.⁹⁶ The first step was a hydrolysis step where ethoxy groups reacted with water to create hydroxyl terminations with alcohol as a byproduct. The second step was a polycondensation step where the hydroxyl groups combined to form siloxane

SiO ₂ wt. %
0.00
0.24
0.34
0.43
0.56
0.88
1.52
3.38

Table 22 - Summarized list of the SiO₂- P(VDF-CTFE) hybrids.

Structure of Hybrids

The microstructure of the polymers were examined with WAXD and TEM to probe the crystal structure of the matrix and the dispersal of the SiO₂ particles respectively. The diffraction pattern, shown in Figure 54, features a sharp peak at 18.2° with less defined shoulders around 17.7° and 19.8°. The location of the peaks in increasing order of 17.7°, 18.2°, 19.8° and are similar to the location expected for the (100), (020), and (110) planes of the α phase respectively. All of the curves are nearly identical no matter the concentration of SiO₂ indicating that neither the crystal phase nor the crystallinity of the hybrids are sensitive to that parameter. Reports on crystallinity trends in silica-polyethylene nanocomposites report similar trends except in the case where the nanoparticles are covalently functionalized with a vinyl silane.^{90,92} In that case, a 36% increase in crystallinity was reported over using the bare nanoparticles.

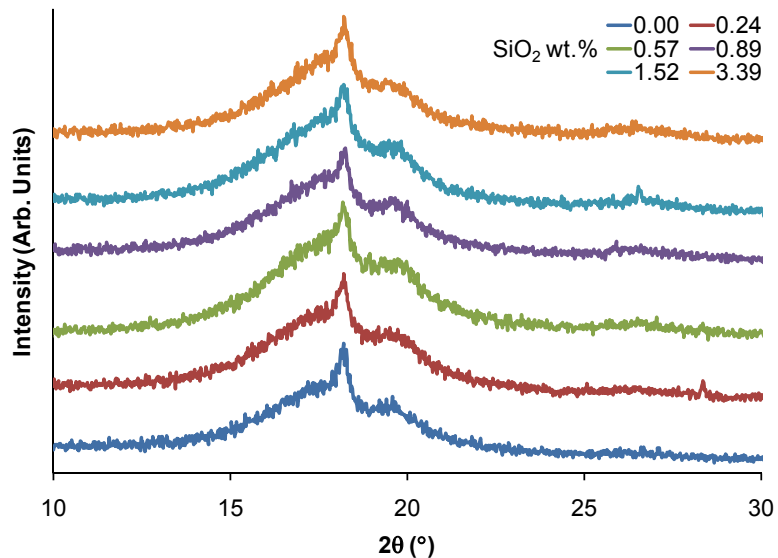


Figure 54 - WAXD of the SiO₂-P(VDF-CTFE) hybrids.

Particle dispersion was first examined by simply looking at the films.

Photographs of two representative films are shown in Figure 55. Both films are nearly identical in appearance and completely transparent with no signs of aggregation of the particles. All the hybrid films shared similar visual appearances.



Figure 55 - Photographs of the SiO₂-P(VDF-CTFE) hybrids. Left - 0.00 wt. %. Right - 3.38 wt. %.

The hybrids were further probed with TEM to examine the SiO₂ dispersion. An example of the 3.38 wt. % hybrid is shown in Figure 56 which doesn't show any evidence of SiO₂ particles. The presence of silicon was confirmed through the use of energy dispersive spectrometry (EDS) to identify the element. The elemental map shown in Figure 56 shows the silicon rich regions, identified by the light squares, to be dispersed homogenously throughout the film. Elemental maps for chlorine and fluorine shows similar images.

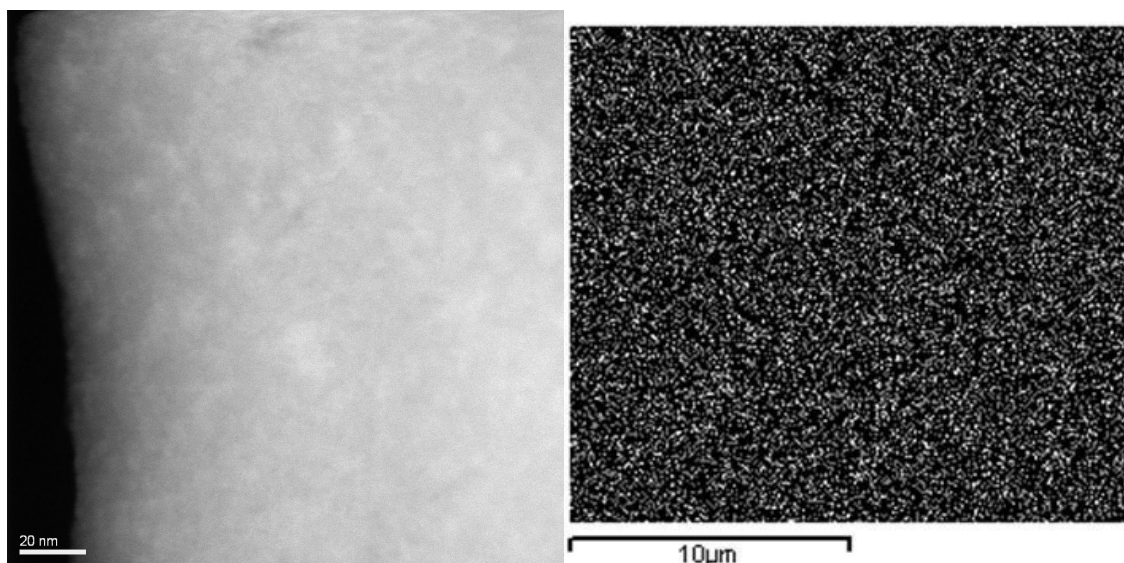


Figure 56 - Left: TEM image of the SiO₂-P(VDF-CTFE) hybrid with 3.38% SiO₂. Right: Silicon elemental EDS image of hybrid.

The lack of larger discrete particles seems to suggest that any particles formed remain as a sol and have not gelled into larger particles. The evolution of the sol-gel process is a complicated one and difficult to judge in the organic reaction conditions used here. Adding acid tends to lower pH and to promote the polycondensation reaction in aqueous conditions.⁹⁷ At the same time, formamide has been shown to inhibit the hydrolysis reaction in aqueous systems.⁹⁶ Seemingly the presence of DMF, which is

chemically similar to formamide, should stunt the hydrolysis in this system making polycondensation and particle formation not likely. However, the hybrid polymers become insoluble after processing indicating that crosslinking is present which is only possible if hydrolysis and polycondensation occur. It may be possible that extremely small particles are forming in the hybrids and are so well dispersed that they give homogenous TEM images.

Thermal Properties

The thermal properties measured by DSC are shown in Table 23. All of the values shown are taken from a second heating and cooling cycle so that all the samples had the same prior thermal history. All of the materials show similar melt and crystallization temperatures around 104°C and 70°C respectively and similar associated enthalpies. The thermal behavior echoes the WAXD data indicating that the materials are all similar in crystallinity. The complete DSC traces can be found in Appendix H.

SiO₂ wt. %	T_m (°C)	ΔH_m (J/g)	T_{cr} (°C)	ΔH_{cr} (J/g)
0.00	105	11.8	69.3	16.3
0.24	104	11.0	68.3	14.2
0.34	105	11.4	71.7	15.4
0.43	104	10.4	69.2	15.0
0.56	101	12.5	66.4	18.0
0.88	105	12.5	72.9	15.9
1.52	102	13.4	71.0	17.4

Table 23 - Thermal properties of the SiO₂-P(VDF-CTE) hybrids.

Dielectric Properties

The low electric field dielectric properties for the hybrid materials are shown in Figure 57. The maximum electric field was approximately 0.05 MV/m. At least four

samples were measured and averaged to produce the curves shown. All of the hybrids containing SiO₂ showed a higher permittivity than the base polymer containing the ethoxy terminated silicon groups. It is interesting to note a 25% increase in the low frequency permittivity of the hybrids despite the lower permittivity of SiO₂ at 3.9 than the matrix copolymer.⁹⁸ According to traditional mixing rules, the permittivity of the hybrids should decrease when adding a lower permittivity inclusion. The increase in low frequency permittivity would indicate an enhanced dipolar or interfacial polarization mechanism. At low electric fields and the lack of charged species in the hybrids, it is unlikely that interfacial polarization is responsible for the permittivity increase. The presence of terminal polar hydroxyl groups in clusters of SiO₂ is more likely for the increase by a dipolar contribution.

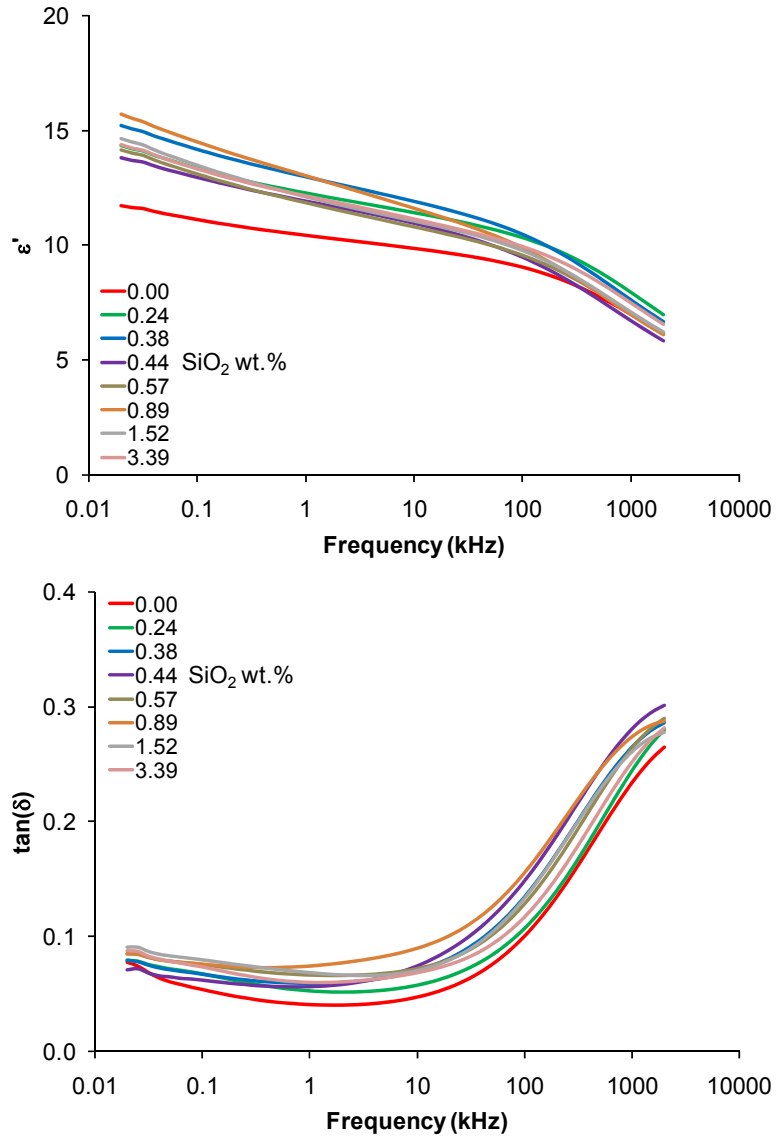


Figure 57 - Low electric field dielectric properties of the SiO₂-P(VDF-CTFE) hybrids.

The temperature varying dielectric properties for the 0.34 wt. % hybrid is shown in Figure 58. The permittivity versus temperature plot shows an increase in permittivity as the material is heated through its glass transition temperature. Even in the frozen state, the material still has a fairly high permittivity at around 3 at -100°C. Above 25°C, the permittivities level off and remain constant through 90°C for all the frequencies measured. A notch in the permittivity is observed at the arrow labeled A on the heating

curve, but not in the subsequent cooling curve. This notch is associated with some early crystallite melting observed in the DSC data on a first scan run. The imaginary permittivity versus temperature plot shows two relaxations previously discussed in Chapter 3. The amorphous relaxation, β_a , begins to appear at 0.1 kHz around -23°C which is consistent with other measurements of the glass transition temperature of other vinylidene fluoropolymers. The β_c relaxation between the crystalline and amorphous regions appears around 25°C at 0.1 kHz. The low frequency imaginary permittivities begin to increase quickly above 50°C and is associated with melting in the hybrid. All of the hybrids showed nearly identical behavior independent of the SiO_2 loading.

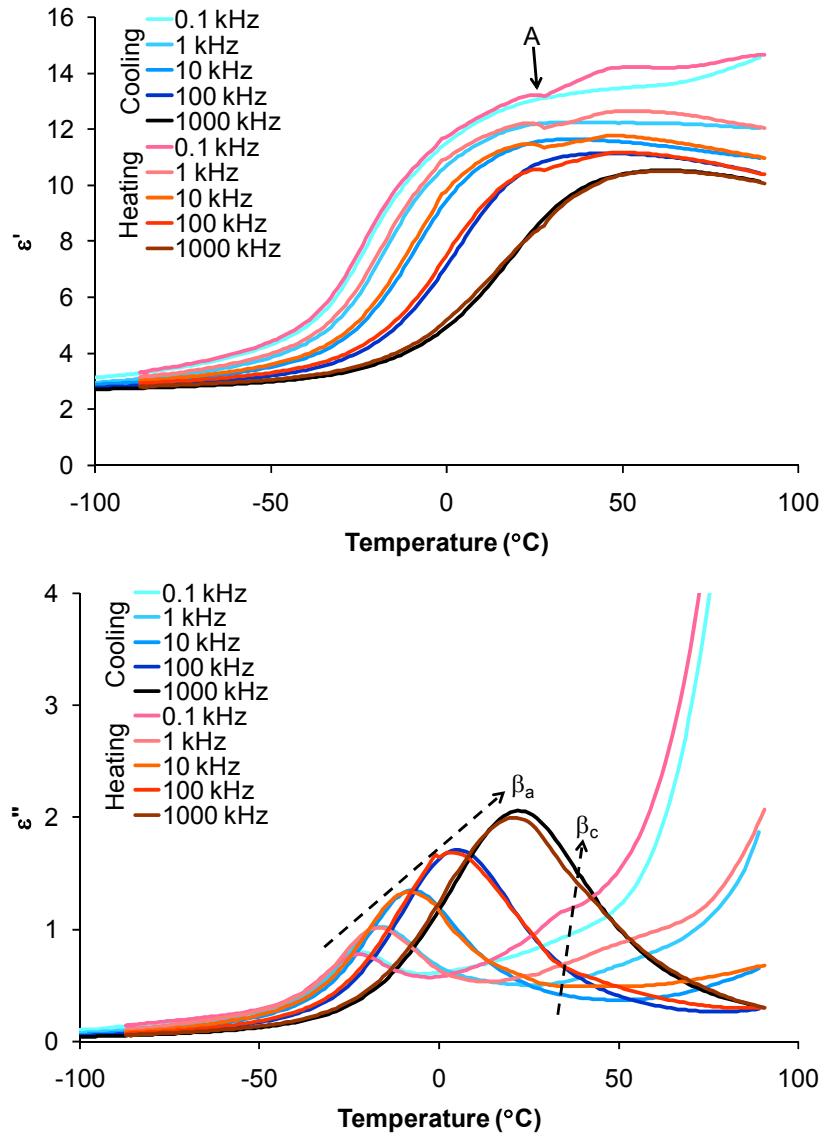


Figure 58 - Temperature varying dielectric properties of the 0.24 wt.% SiO₂ hybrid.

Electrical Breakdown

The electrical breakdown results for the hybrid materials are shown in Figure 59. The breakdown was measured using the electrostatic pull down method mentioned earlier at 25°C with a 500 V/s ramp rate. The Weibull statistics were computed from at least ten data points for each hybrid. The complete Weibull plots and calculated constants are shown in Appendix I. For the range of SiO₂ compositions measured, a maximum

breakdown strength of 297 MV/m was recorded for the 0.34 wt. % sample which was 34% increase over the 0.00 wt. % sample. The breakdown strength decreased above and below the 0.34 wt. % sample.

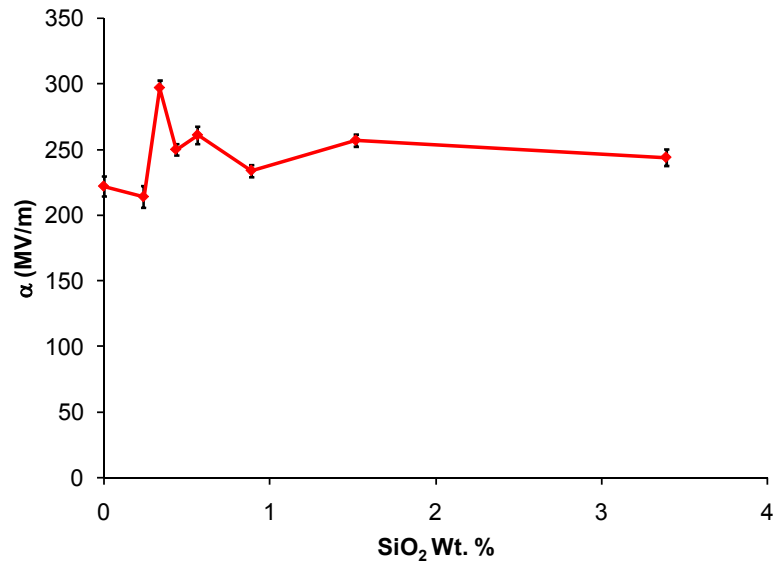


Figure 59 - Electrical breakdown strengths of SiO₂-P(VDF-CTFE) hybrids.

Mechanical Properties

The high strain mechanical properties of the hybrids were measured and are displayed in Figure 60 and listed in Table 24. The yield stress of the hybrids increases approximately 30% when the crosslinking reaction is performed in the hybrids indicating that chemical crosslinks were formed. The moduli also increased approximately 40% averaged across all the crosslinked materials when compared to the uncrosslinked 0.00 wt. % material. The yield stress was used to calculate the electromechanical breakdown strength based on Equation 20. No observed trend was observed from the calculated strengths with every value being higher than the equivalent measured value. The calculated strengths over predicted the measured strengths by an average of 44%

indicating that electromechanical breakdown is not the likely breakdown mechanism in the hybrids.

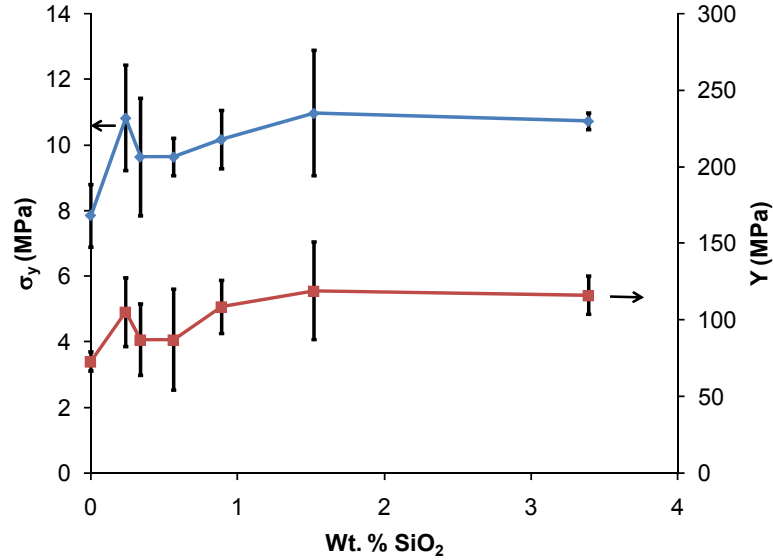


Figure 60 - Yield stresses and moduli of the SiO₂-P(VDF-CTFE) hybrids.

SiO ₂ wt%	σ _y (MPa)	Y (MPa)
0.00	7.85 (±0.96)	72.9 (±6.40)
0.24	10.8 (±1.61)	105 (±22.3)
0.34	9.63 (±1.79)	87.1 (±23.4)
0.56	9.63 (±0.58)	87.1 (±33.1)
0.88	10.2 (±0.89)	109 (±17.3)
1.52	11.0 (±1.91)	119 (±31.7)
3.39	10.7 (±0.26)	116 (±12.7)

Table 24 - Yield stresses and moduli of the SiO₂-P(VDF-CTFE) hybrids.

High Field Electric Displacement

The high electric field displacement was examined in the hybrids as an attempt to understand the electrical breakdown behavior. The electric displacement was measured at 1, 10, or 100 Hz using a unipolar triangle electric field signal. An example of a plot measured at 1 Hz for the 0.00 and 0.34 wt. % SiO₂ samples are shown in Figure 61. On

the initial electric field ramp, both materials have a linear increase in displacement. All the hybrid materials at all the frequencies showed this same trend which is an indicator for a linear dielectric material. However, the shapes of the loops are very different between the two presented materials. The area contained within the loop is a measure of the energy loss and can be calculated using Equation 12. The area within the loops of the 0.00 wt. % samples are much larger than 0.34 wt. % samples showing that more of the stored energy is not released in the former material.

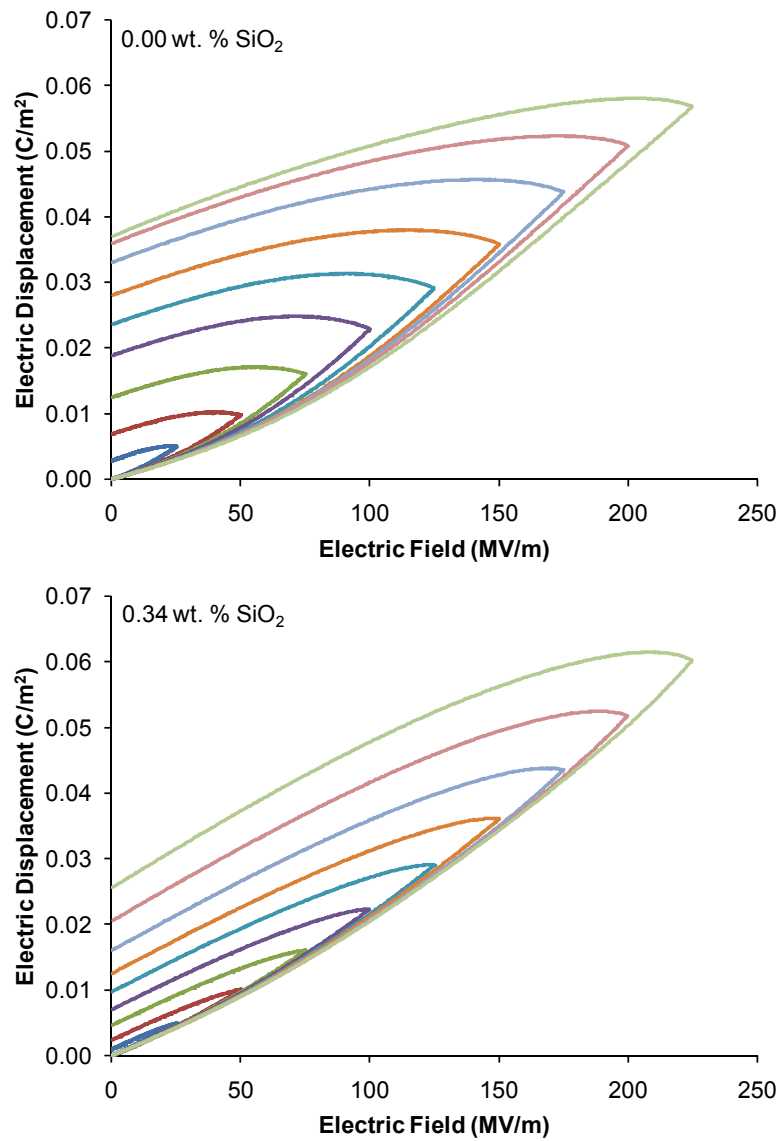


Figure 61 - Electric displacement measurements of the hybrid materials at 1 Hz.

Examining the same two materials at a higher frequency is shown in Figure 62 for 100 Hz. The loops at this frequency compared to the lower frequency are much slimmer with lower maximum displacement. The slimmer loops immediately point to lower losses at this higher frequency. This differs from the low electric field data shown in Figure 57 which shows a relatively flat loss curve at these frequencies. The difference in displacement for the two materials at the two frequencies also implies differences in the permittivities which can be calculated using a combination of Equation 3 and Equation 13. At these higher electric fields for the 0.00 wt. % material, the permittivity at 1 and 100 Hz are 34 and 15 respectively which is also reflected for the other samples. This large difference in permittivity is also not observed in the low electrical field permittivity data for the similar frequencies. One explanation for the larger permittivity observed in the high field displacement measurements at 1 Hz may be charge injection from the electrodes since the fields in these measurements are four orders of magnitude greater than the low field measurement. The combination of the injected charge and low frequency could generate an interfacial polarization which would be responsible for the increase in permittivity. The same charge injection probably happens for the higher frequency measurement, but doesn't generate the same interfacial polarization due to the limited time for charge movement resulting in a lower permittivity.

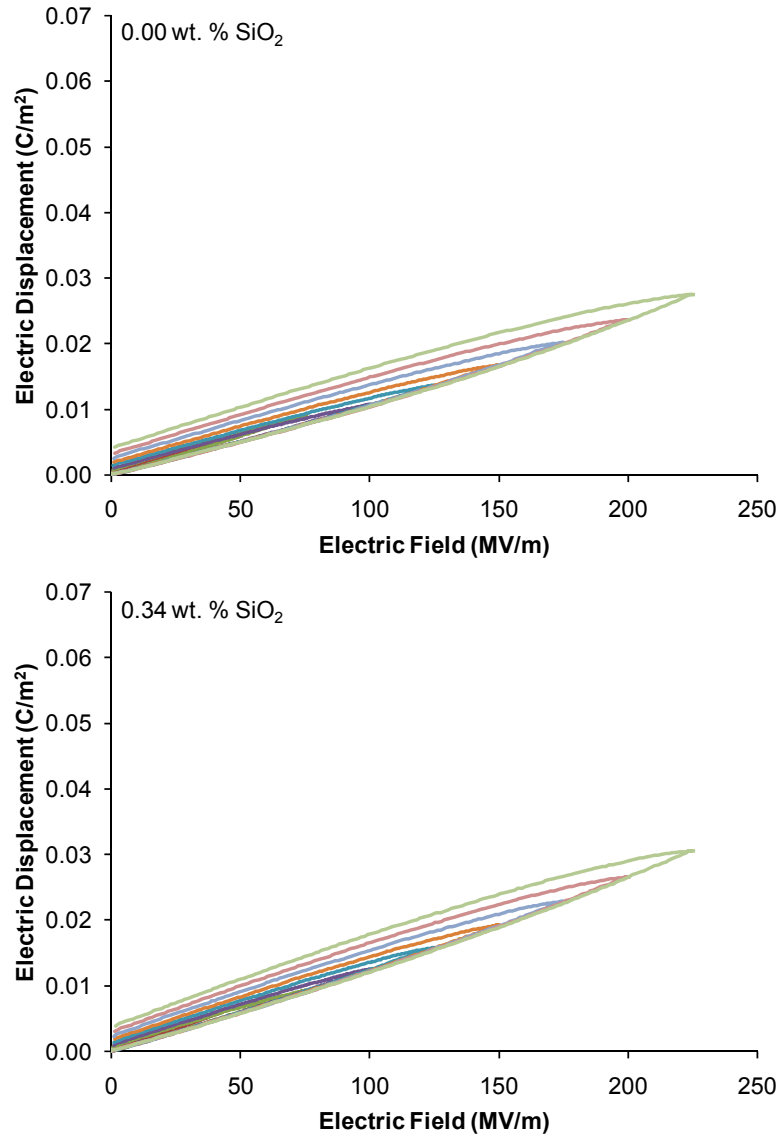


Figure 62 - Electric displacement measurements of the hybrid materials at 100 Hz.

The calculated losses for all the hybrid materials from the high field displacement measurements at 10 Hz are shown in Figure 63. A minimum in losses is observed around the 0.34 wt. % hybrid which is consistent across all the electric fields. This minimum coincides with the maximum observed in electrical breakdown strength in Figure 59. The minimum in the loss is observed in the same composition location for all three of the high field frequencies measured. Electrical loss in capacitors is dissipated as heat which

would implicate that a thermal breakdown mechanism is responsible for breakdown. The materials at the minimum in loss dissipate the least heat giving them higher breakdown strengths.

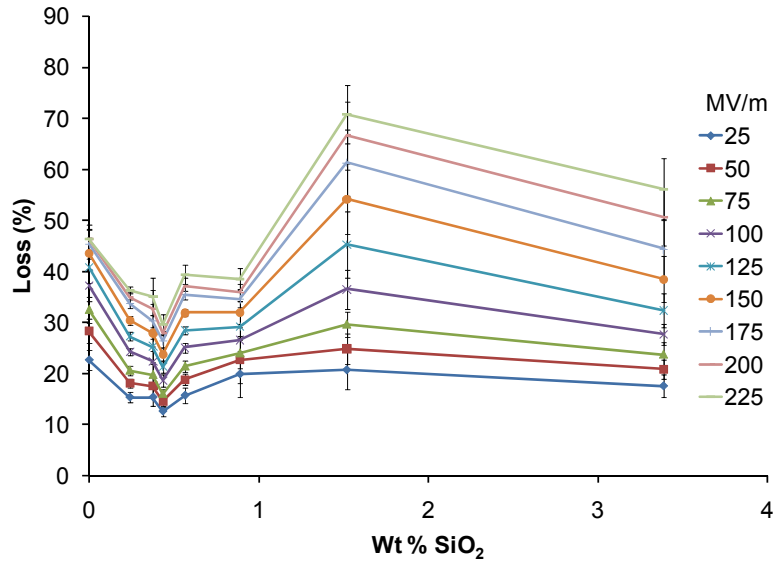


Figure 63 - High field losses calculated for all the hybrid materials at 10 Hz.

Finally, the energy storage properties of a hybrid material is shown in Figure 64 for the 0.43 wt. % material which is located in the loss minimum of Figure 63. Figure 64 demonstrates that the hybrids can have a high energy density with this material achieving 21.5 J/cm^3 at a field of 500 MV/m with a low loss of 44%.

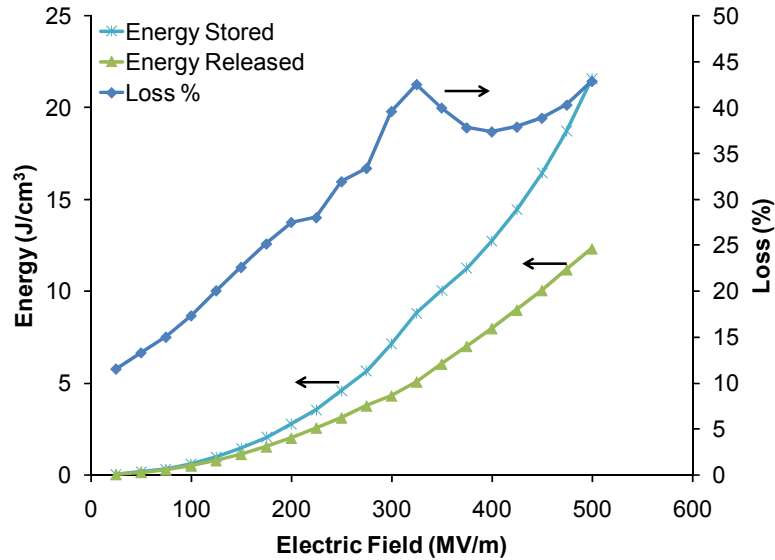


Figure 64 - Energy storage values of the 0.43 wt. % hybrid.

Thermally Stimulated Discharge Current Measurements

The discharge behavior of the hybrids was measured with thermally stimulated discharge current (TSDC) to further probe the mechanism of the electrical failure. TSDC measurements were performed using a four step procedure illustrated in Figure 65. Each of the samples was first heated to 90°C which is represented by 1 in the figure. Second, an electric field was applied to the hybrids as the temperature was maintained at 90°C. Third, the samples were rapidly cooled to -100°C with the electric field still applied. Lastly, the electric field was removed and the samples were short circuited and heated at a fixed rate to 100°C while the current was measured across the sample. The electric field applied to the material in the second and third steps as well as the heating rate in step four were used as variables to the measurement.

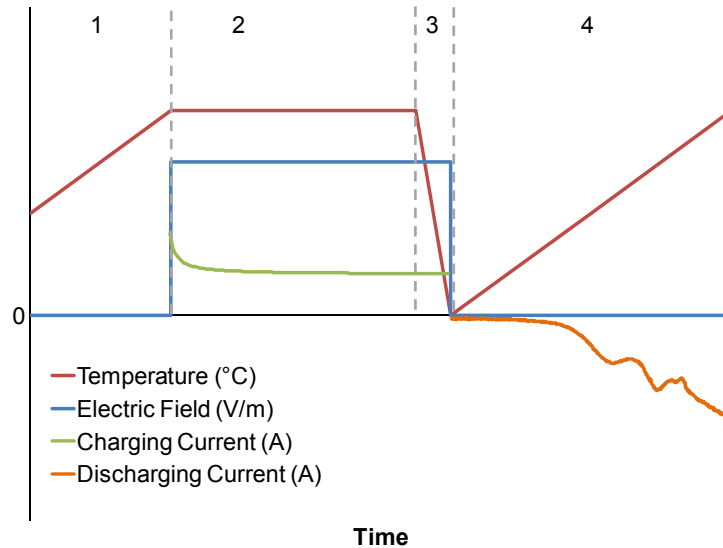


Figure 65 - Schematic of the TSDC measurement technique.

TSDC is complimentary technique to dielectric spectroscopy and is used to map out equivalent relaxations.⁹⁹ TSDC's advantages lies in the ability to apply much higher electric fields and its lower equivalent frequency which is on the order of 1×10^{-3} and 1×10^{-4} Hz for the materials measured here. These low frequencies are often very difficult to measure using dielectric spectroscopy due to long measurement times and high conduction losses. During the high temperature poling and subsequent cooling step, permanent dipoles and other charged species migrate in the material and are frozen in place in a charged state upon cooling. By heating the materials at a controlled rate, the charged species are able to move once the minimum temperature associated with that relaxation is reached and attempt to neutralize electric field across the sample. Heating in the TSDC technique enables the observations of long-time relaxations through a thermal activation process.

Current in TSDC is primarily caused by three mechanisms which are dipole reorientation, space charge limited drift, and diffusion of excess charges.¹⁰⁰ Dipole

reorientation has a current release efficiency of 100% since the decay process doesn't involve any charge neutralization. The same cannot be said of the other two current producing mechanisms where current is caused by the motion of monopole charged species. Current is only measured in TSDC when electrons move through the external ammeter to neutralize positive charges which can be holes or image charges. When monopole charges are involved, neutralization can occur through the former mechanism or by recombination in the bulk of the material where no current would be measured. As a result, release efficiencies can be less than 100% and give the appearance that charge is lost in the material. This necessitates the careful interpretation of TSDC data especially where complicated relaxation processes are involved. This is the primary reason why TSDC must be used in conjunction with traditional dielectric spectroscopy to identify relaxations.

The TSDC curves measured at a constant heating rate of 5°C/min and different electric poling fields are shown in Figure 66 for the 0.00 wt. % hybrid. Three relaxations are identified in the temperature range of the figure. The first is the β_a relaxation associated with the amorphous relaxation of the glass transition and occurs at -28°C. The location of this relaxation is in agreement with previous dielectric measurements. Additionally, the location of this relaxation falls in between other reported β_a value from TSDC measurements for P(CTFE) at 2°C and P(VDF) at (-53)-(-73)°C.^{29,101,102} The β_c relaxation between the amorphous and crystalline regions is centered around 9°C. This is lower than the temperature reported from dielectric data which shows this peak around 25°C measured at 100 Hz. In P(VDF), this transition is recorded at 47°C for TSDC data and in the P(VDF-CTFE-TrFE) 78.8/14.0/7.2 mol%, which is similar in CTFE

composition to the hybrid copolymer, this transition is seen around 19°C for spectroscopy data at 100 Hz.²⁹ As CTFE is added to P(VDF-CTFE), the β_c transition moves to lower temperatures. Since the TSDC measurement are at an equivalent 5 orders of magnitude lower frequency than the dielectric measurement at 100 Hz, it is not unreasonable that the β_c transition could move to a lower temperature. Finally, the γ_L peak at 36°C is a new one not present in the dielectric spectroscopy and is assigned to low temperature charge trap sites in the hybrid. This peak only appears in the highest field of 20 MV/m indicating that the peak may be present at the lower fields, but requires a certain charge threshold in order to be observed in the TSDC curves.

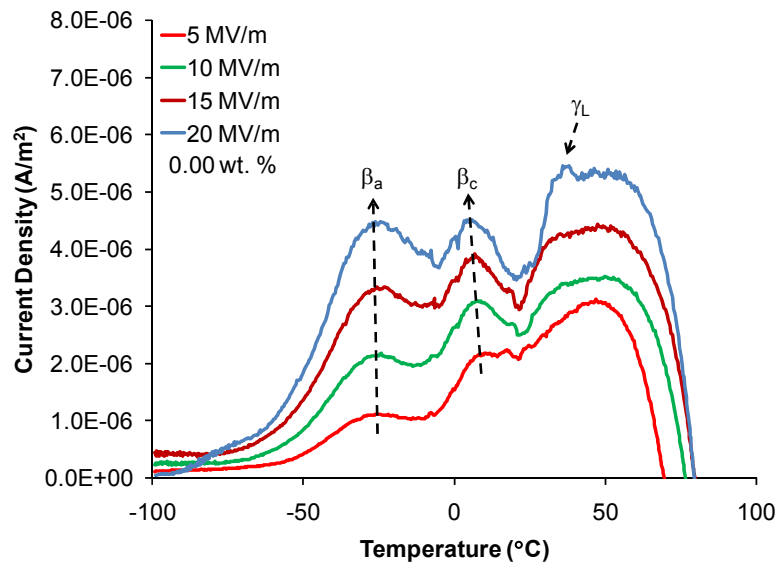


Figure 66 - Positive TSDC curves for the 0.00 wt. % hybrid at a constant heating rate.

Figure 67 shows the negative TSDC curves measured for the 0.00 wt. % hybrid. These negative peaks are unusual for TSDC, but present for all the hybrids measured. The negative current in this figure indicates a reversal in the direction of the current where the current is flowing in the same direction as it was during the initial poling phase

of the measurement. These negative peaks are called “anomalous” in some literature and are attributed to space charge movement.¹⁰³ As mentioned before, space charge can move in the material either by drift or diffusion mechanisms where charges are driven by an electric field or concentration gradient respectively. These two mechanisms having opposite vector directions as shown in

$$J(t) = \varepsilon \frac{\partial}{\partial t} F(x, t) + e\mu n(x, t)F(x, t) - eD \frac{\partial}{\partial x} n(x, t)$$

Equation 28 - Space charge movement by drift and diffusion.

where J is the current density, ε is the permittivity, t is the time, F is electric field, x is distance, e is electronic charge, μ is carrier mobility, n is concentration, and D is the diffusion constant.¹⁰⁴ Drift seeks to minimize electric field while diffusion seeks to evenly spread charge in a material. The difference in direction and magnitude of charge mobility and diffusion constants gives rise to the anomalous currents. When the hybrid is heated about 70°C, the trapped charges from the γ_L sites gain enough thermal energy to move by a diffusion mechanism and are responsible for the negative peaks. The γ_S peak in Figure 67 is assigned to the movement of space charge and is identified by a peak that shifts its maximum peak temperature and changes in shape as a function of the poling electric field.¹⁰⁵ The final peak occurring at 97°C is the δ peak and is assigned to melting and the release of all charges in the material.

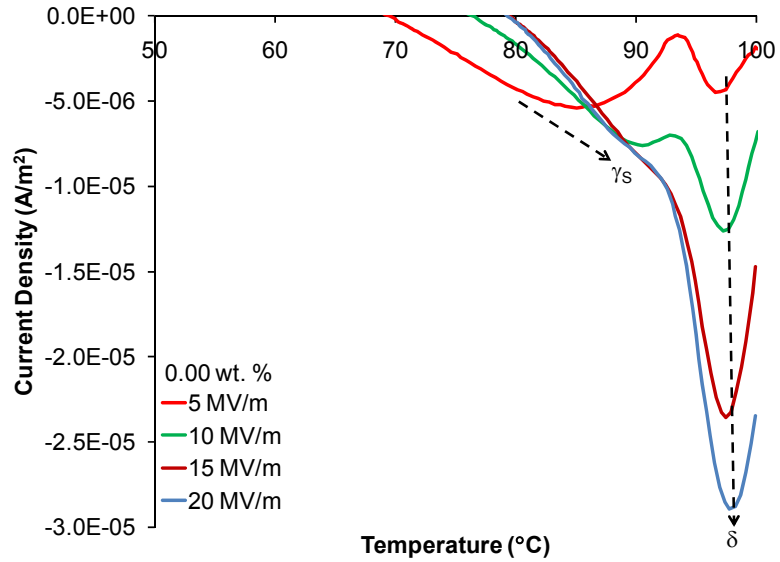


Figure 67 - Negative TSDC curves for the 0.00 wt. % hybrid at a constant heating rate.

The full TSDC curves for the 0.00 wt. % hybrid is shown in Figure 68 for a constant poling field of 10 MV/m and varying heating rate. As the heating rate is decreased from 10 to 1°C/min, the intensity of the γ_s and the δ peaks decrease. The reduction in the space charge is due to the increase in the time allowed for diffusion and the increased charge recombination for the longer measurements.

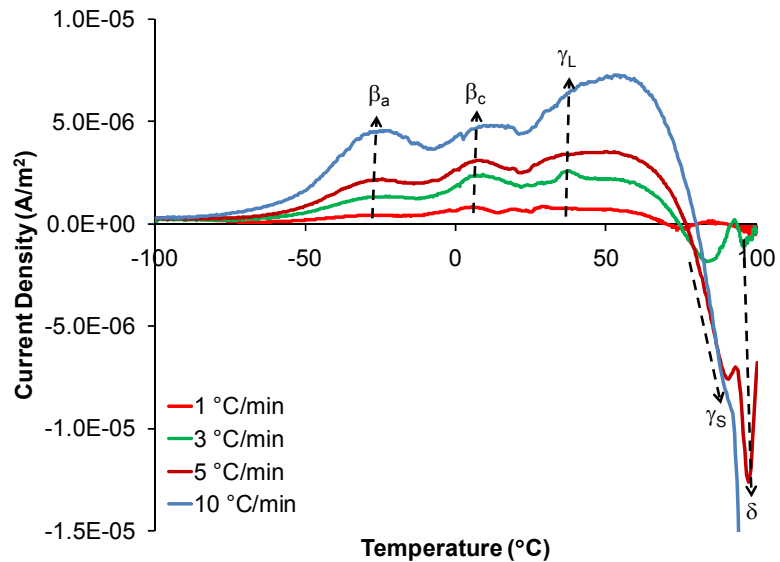


Figure 68 - Full TSDC curves for the 0.00 wt. % hybrid at a constant poling field.

The positive TSDC curves for the 0.34 wt. % hybrids are shown in Figure 69. All the relaxations present for the 0.00 wt. % sample are present with a few exceptions. The first is a shift in the β_c relaxation to approximately 25°C indicating an increased activation energy for this process when the material is crosslinked. The second is a more prominent γ_L peak which doesn't shift in temperature, but is much more prominent indicating a larger number of trap sites. Lastly, a new peak at 48°C is assigned γ_H and is a high temperature trap site with an increased activation energy and attributed to additional traps created as the result of crosslinking in the hybrid.

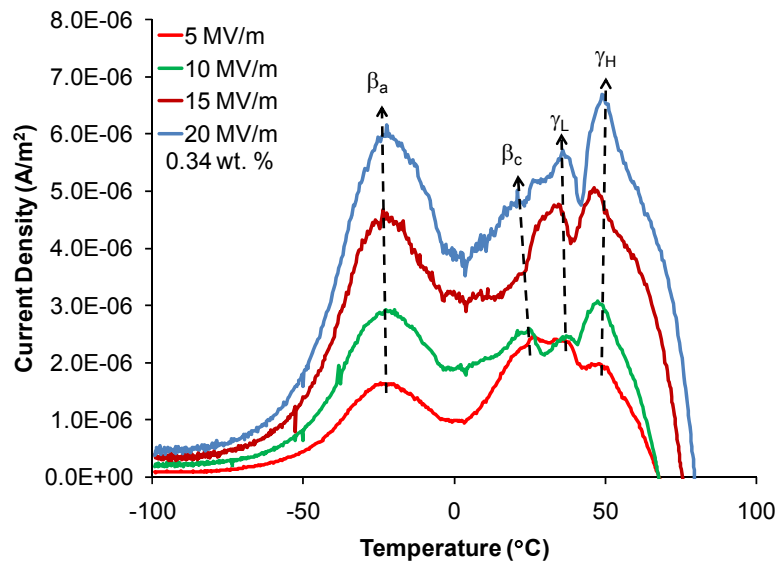


Figure 69 - Positive TSDC curves for the 0.34 wt. % hybrid at a constant heating rate.

The negative peaks of the 0.34 wt. % sample are shown in Figure 70. The γ_s peak assigned to the release of space charge resides in the same place as the 0.00 wt. % sample though the peaks here are broader. The δ peak associated with charge release from melting is not present and appears to have shifted to higher temperatures. As the material

is crosslinked, the crosslinks may act as barriers for diffusion requiring a higher energy and thus temperature to observe this melting transition charge release.

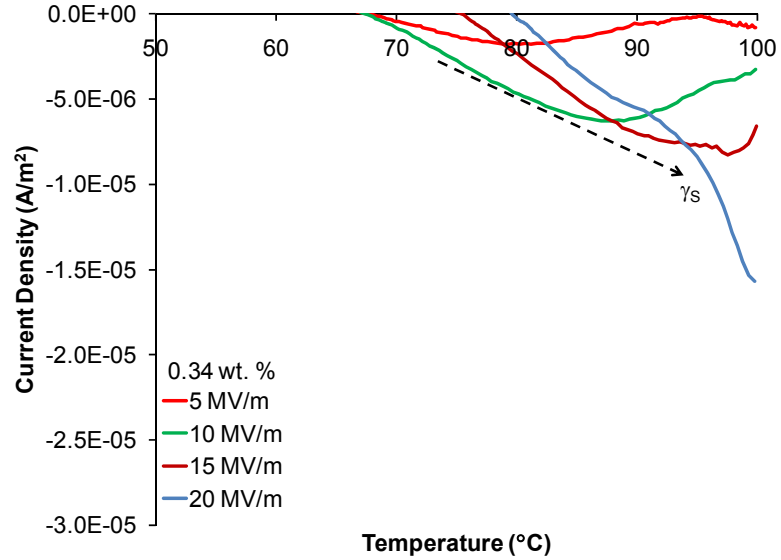


Figure 70 - Negative TSDC curves for the 0.34 wt. % hybrid at a constant heating rate.

Figure 71 summarizes all of the positive TSDC curves for the 0.00, 0.24, and 0.34 wt. % samples measured at a 20 MV/m poling field and 5°C/min heating rate. The complete curves for all three samples can be found in Appendix J. The β_a relaxation remains constant around -28°C for all the materials. The activation energy can be calculated according to

$$\ln(J_D(T)) \approx A - \frac{E}{kT}$$

Equation 29 - Initial rise method for calculating the activation energy from TSDC data for an Arrhenius process.

where J_D is the current density, T is the temperature, A is a constant, E is the activation energy, and k is Boltzman's constant.⁹⁹ Alternatively, the activation energy can also be calculated using

$$\ln \tau(T) = \ln \left[\int_{t(T)}^{\infty} J(t') dt' \right] - \ln(J_D(T)) = \ln(\tau_o) + \frac{E}{kT}$$

Equation 30 - Graphical integration method for calculating the activation energy from TSDC data for an Arrhenius process.

where τ relaxation time, t is the time, and τ_o is the pre-exponential factor.⁹⁹ The calculated activation energies are 0.24 and 0.36 eV for the initial rise and graphical integration methods respectively. The activation energy was also calculated from the imaginary part of the permittivity dielectric spectroscopy data using

$$f = A e^{\frac{-E}{kT_m}}$$

Equation 31 - Activation energy for an Arrhenius process.

where f is the frequency, and T_m is the temperature peak at that frequency.⁹ The calculated activation energy of 1.16 eV is higher than the energies calculated from the TSDC data. One reason for this may be that the TSDC peaks for the β_a transition may contain other relaxations making them too broad an effective evaluation of this parameter.

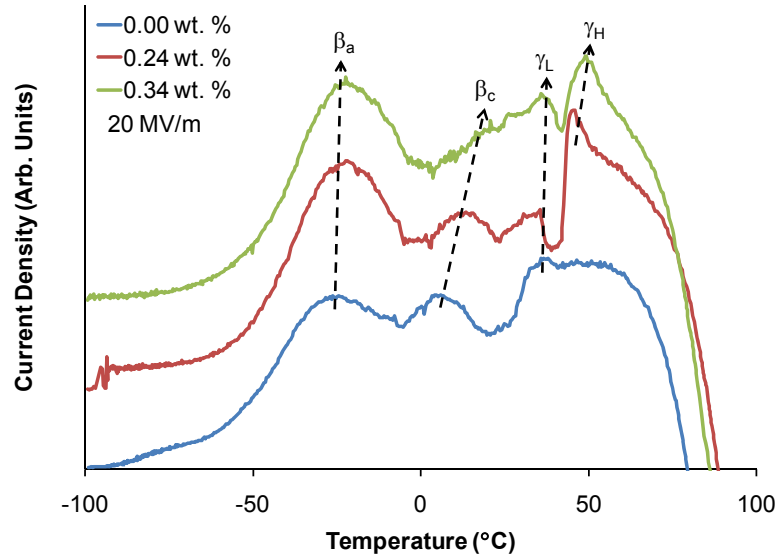


Figure 71 - Composite of the three hybrids at a constant heating rate and poling field.

The β_c relaxation increases in temperature from 9 to 25°C with the increase of SiO₂ content indicating an increasing activation energy. The γ_L low temperature trap site remains unchanged in its location at 36°C for all the hybrids. The γ_H higher temperature trap site is only present for the crosslinked hybrids and is located at 48°C indicating a deeper trap state in the materials with a higher activation energy. The combination of the increased β_c and γ_H in the crosslinked hybrids could be reasons behind the increased breakdown strength in the hybrid materials. The presence of additional deeper traps site could reduce space charge movement resulting in the observation of lower losses seen in the high field displacement data for the some of the hybrids. The lower losses mean lower power dissipation and support the thermal breakdown electrical breakdown mechanism. The higher breakdown strengths at a certain loading of seen in Figure 59 may be due to some optimization of the microstructure that is presently not observed.

CHAPTER 6 - CONCLUSION

Summary of the Results

The properties of several new fluoropolymer systems were explored in this dissertation and their energy storage properties were explored for applications as capacitor dielectrics. The important parameters in determining the energy density of a capacitor dielectric are the permittivity and the electrical breakdown strength which were both explored in this dissertation. The work began with the introduction of a novel synthetic method of producing VDF based fluoropolymers. This method involves a two step procedure beginning with the copolymerization of VDF and CTFE to produce the copolymer P(VDF-CTFE). The second step selectively hydrogenates the CTFE units to TrFE by means of a fully quantitative reaction to produce the terpolymer P(VDF-CTFE-TrFE). This two step procedure has several advantages over the traditional direct copolymerization of VDF, CTFE, and TrFE including precise control over the final terpolymer chemical composition. Using this novel procedure, approximately 50 different chemical compositions of low molecular weight copolymers based on this new synthetic method were produced and the resulting properties were studied.

Examining the chemical structure of the terpolymers revealed that the new synthetic method produced polymers containing a large amount of tail to tail defects originating in the initial VDF and CTFE copolymerization and continuing through to the final terpolymers. For an example terpolymer produced through the method presented here and direct copolymerization, it was found that almost none of the VDF to TrFE linkages in the new synthetic method existed in the head to tail tacticity arrangement

whereas 9% existed in this arrangement for the direct terpolymerization. The effects of the high number of tail to tail defects became apparent when comparing the properties of the polymers produced by the two methods.

The thermal properties of the polymers showed that the melt temperatures increased as the amount of TrFE increased for a fixed amount of VDF implying an increase in crystallinity. The melt temperature also increased with the amount of VDF in the polymers while holding the other monomers constant again implying increasing crystallinity. The Curie transition temperature was also found to decrease as the amount of CTFE increased at a fixed amount of VDF showing that this parameter could be controlled through chemical composition.

The crystal structure could be controlled through the chemical composition. Crystallinity decreased with increasing amounts of CTFE for fixed amounts of VDF and increased for increasing amounts of VDF with the other parameters fixed. The crystal phase varied with chemical composition changing from the α to γ to β phase as the polymers were hydrogenated from P(VDF-CTFE) to P(VDF-TrFE).

All of the changes in crystallinity and crystal phases altered the dielectric properties of the polymers. By varying the chemical composition, the permittivity of the polymers could be changed from a low value of about 10 to a high value of 50 measured at 1 kHz with losses remaining below 10%. High permittivities were obtained at optimized terpolymer compositions where the correct amount of ferroelectric crystal phases and overall crystallinity lead to high polarizability in the samples. Dielectric spectroscopy of a grouping of polymers with a fixed amount of VDF and changing ratios of CTFE and TrFE showed the gradual change of normal to relaxor ferroelectric behavior

and the characteristic relaxations associated with the change. Finally, a phase diagram mapping the paraelectric to ferroelectric transition in the P(VDF-TrFE) copolymers revealed shifted phase lines compared to the direct copolymerization of these two monomers illustrating again the effect of the tail to tail tacticity defects.

The electrical breakdown mechanisms of the fluoropolymers were explored beginning with the study of a P(VDF-CTFE) system. In this study, the molecular weight was varied at a constant composition to study its effect on the electrical breakdown strength. An emulsion polymerization method was used and proved successful in increasing the molecular weight five-fold compared to the solution method. A low crystallinity composition of P(VDF-CTFE) was used to minimize any crystallinity influence on breakdown strength while keeping most other properties identical for testing. The only significantly differing properties were the mechanical properties which improved as the molecular weight increased. Electrical breakdown was tested on three different molecular weights of copolymers at three different temperatures. At room temperature, an electromechanical breakdown mechanism was found to be responsible for failure and was verified through the use a new model incorporating the measured yield stress of the polymers. At -35°C below the glass transition temperature of the copolymer, a thermal breakdown mechanism was found to be responsible for the failure. This was verified through the application of an impulse thermal breakdown model incorporating various measured parameters to accurately predict the breakdown strengths. At an intermediate temperature of -15°C , a combination of the thermal and electromechanical mechanisms was found to operate. The energy density of the copolymer system was calculated for each of the copolymers at each of the three

temperatures. Energy density was found increase 123% across all the temperatures as the molecular weight was increased and 77% across all the molecular weights as the temperature was lowered from 25°C to -35°C. Despite the reduction in permittivity at low temperatures, the permittivity of the copolymers continued to increase due to the increase in electrical breakdown strength.

The breakdown mechanism of a more complicated system of fluoropolymers with constant molecular weight and VDF content, and varying chemical composition was studied combining the synthetic strategies from the previous works. This system presented an additional challenge due to the fact that the properties of the polymers changed with chemical composition. A high molecular weight polymer was used in this study based on the increased breakdown strength observed in the molecular weight study. Like the low molecular weight terpolymers, the crystallinity and melt temperature were found to increase as the amount of TrFE increased in the material. The crystal phase also changed from the paraelectric α phase to the ferroelectric γ and β phases as the amount of TrFE increased in the polymer. The permittivity showed a maximum at an intermediate hydrogenation also confirming the low molecular weight results.

Electrical breakdown in the composition study was attributed to an electromechanical breakdown mechanism at 25°C. For polymers with a high amount of CTFE, the Maxwell stress dominates the electromechanical stress due to the low crystallinity and moduli of the materials. At low amounts of CTFE or high amounts of TrFE, both the Maxwell and electrostrictive stresses contribute to the electromechanical stress due to the high crystallinity of these materials. The origin of the electrostrictive stress is a crystal phase change that occurs under high electric field and can be significant

depending on chemical composition. The electrostrictive stress thus has a negative effect on the breakdown strength and must be considered for ferroelectric samples. Energy density was found to saturate at high amounts of TrFE due a combination of increasing breakdown strength and decreasing polarizability with increasing TrFE.

Finally, the electrical breakdown performance in a novel SiO₂-P(VDF-CTFE) hybrid system was explored. The materials were produced using a copolymer made with a functionalized silane initiator and sol-gel process. A study of the microstructure of the hybrids revealed that all the materials had identical crystallinities and crystallized in the α phase. The presence of nanoparticles was not detected in TEM images, but elemental analysis revealed the presence of uniformly dispersed silicon indicating a finer dispersion of SiO₂ in the hybrids. An increase in permittivity was observed in the crosslinked hybrids despite the inclusion of the lower permittivity SiO₂ particles which was attributed to dipolar motion from free hydroxyl groups. Electrical breakdown strength increased 34% over the base polymer at an intermediate amount of SiO₂ wt. % of 0.34. Mechanical testing showed that an electromechanical breakdown model over predicted the breakdown strength. High electric field displacement measurements revealed a minimum in the loss of the hybrids around the 0.34 wt. % region implicating that thermal breakdown is the failure mechanism due to electrical power dissipation by heat. TSDC measurements confirmed these results showing that crosslinking introduces a high temperature charge trap sites that reduced space charge in the material. An energy density of 20 J/cm³ at 500 MV/m was demonstrated in a hybrid material containing 0.43 wt. % SiO₂ showing that these hybrid materials hold the potential for achieving a high energy density with further work.

Suggested Future Work

The work in this dissertation focused on exploring the breakdown mechanisms in vinylidene fluoride based fluoropolymers. Future work in this area should continue to examine the breakdown mechanisms as well as ways for improving breakdown strength through optimization of the materials.

The electrical breakdown behavior at low temperatures should be explored for a wider range of chemical compositions of the copolymers. It was shown that the breakdown strength and the resulting energy density increased as the temperature was lowered despite reductions in the permittivity. Testing at temperatures lower than -35°C may reveal different operable breakdown mechanisms. Additionally, the breakdown and energy storage behavior of terpolymers compositions may be especially interesting given their high room temperature permittivities and their unique crystal phases and how these properties translate at low temperatures. While cooling may not be practical for all capacitor applications, it may worthwhile for some specialty applications where this can be provided. Long term degradation testing would also be useful for determining how applicable these fluoropolymers are for capacitor applications. Voltage endurance measurements can determine the performance of these dielectrics in DC applications where a capacitor may be charged for an indefinite amount of time before discharging.

Many of the electrical properties measured in this worked where taken using low electric fields where the maximum fields were below 0.1 MV/m . For the fluoropolymers used here, three regimes of electric field intensity can be identified. A low field regime, where the fields are below 0.1 MV/m , is useful for basic characterizations where the

polymers behave as linear dielectric materials. A medium electric field regime from 0.1 to 10 MV/m is useful for probing the materials at higher fields, but for still in the linear regime for most fluoropolymers. Finally, a high electric field regime extending from 10 MV/m to the breakdown strength covers the range where the fluoropolymers will transition to nonlinear dielectric behavior. The medium and high field regimes are probably the most interesting for examining the electrical properties, but difficult to access due to voltage limitations on most characterization equipment. For a typical thickness of ten micrometers, which would be somewhere between the thicknesses produced in a laboratory and industrial setting, a voltage of 5000 volts would be necessary for measurement at 500 MV/m. Thinner films less than a micrometer thick could be produced through vapor deposition processes or spin coating reducing the voltage requirements, but these methods introduce microstructural differences between them and the thicker films. The typical voltages produced by most characterization equipment is limited to less than 100 volts and in some cases, 1000 volts.

One particular useful measurement would be high electric field dielectric spectroscopy. This technique would be similar to the high field electric displacement measurements, but enable the direct analysis of the complex permittivity. At various points in this dissertation, discrepancies were discovered between measured low and high electric field measurements and this technique could bridge that gap. Ultimately, the high field properties are the most important since any actual energy storage capacitor would be operated in this electric field range. Interesting new relaxations could be present at high fields not seen at lower ones. However, this technique would not be without its challenges. Any measurement at a given frequency would have to be cycled a

few times before a steady-state response was achieved. The associated loss in the fluoropolymers, which can be significant at low electric fields, would only magnify at higher fields. As mentioned before, loss is dissipated as heat making thermal breakdown a constant concern. In addition to measuring the complex permittivity, the raw current and voltage output data could be analyzed to track current and energy storage in the samples.

A detailed study into the conduction mechanisms of the fluoropolymers is recommended. As shown in the last chapter, when conduction due to space charge was reduced, an increase in breakdown strength was achieved. In any capacitor dielectric, one would like to minimize the DC conductivity to minimize loss when the device is in the charged state. This conduction is also manifested in AC operation as current that responds in phase with the electric field to produce AC losses. Conduction at high electric fields should be a special focus where contributions can come from a number of sources with the most important probably being electrode charge injection and chemical species ionization.

Finally, optimizing materials whether by chemical or structural means could lead to improvements in breakdown strength and energy density. In the last chapter, crosslinking lead to a limited increase at a certain level, but could perhaps be enhanced with a higher crosslinking density. Additional structural modifications such as different crosslinking agents and orientation of the polymer chains through mechanical stretching could lead to improvements.

APPENDIX A: THERMAL PROPERTIES OF THE HYDROGENATED POLYMERS

For the tables here, ‘-’ denotes that the quantity was not observed.

mol(%)			Heating			
			°C		J/g	
VDF	CTFE	TrFE	T _c	T _m	ΔH _c	ΔH _m
73.6	0.00	26.4	106	160	1.31	29.0
73.6	6.70	19.7	-	125	-	18.8
73.6	10.4	16.0	-	106	-	15.7
73.6	13.5	12.9	-	87	-	12.1
73.6	20.0	6.40	-	54	-	6.90

mol(%)			Heating			
			°C		J/g	
VDF	CTFE	TrFE	T _c	T _m	ΔH _c	ΔH _m
75.5	0.00	24.5	107	154	3.47	29.0
75.5	9.30	15.2	-	117	-	6.64
75.5	15.2	9.30	-	76	-	11.6
75.5	17.2	7.30	-	57	-	7.50
75.5	21.0	3.50	-	39	-	-

mol(%)			Heating			
			°C		J/g	
VDF	CTFE	TrFE	T _c	T _m	ΔH _c	ΔH _m
78.8	0.00	21.2	98	152	7.44	28.3
78.8	6.00	15.2	46	113	2.36	17.3
78.8	14.0	7.20	23	79	1.56	12.7
78.8	15.8	5.40	23	66	0.95	8.57
78.8	16.2	5.00	23	64	0.98	7.55

mol(%)			Heating			
			°C		J/g	
VDF	CTFE	TrFE	T _c	T _m	ΔH _c	ΔH _m
79.2	0.00	20.8	97	147	8.28	25.7
79.2	7.60	13.2	54	118	3.01	18.1
79.2	10.9	9.90	38	100	3.21	16.3
79.2	13.6	7.20	36	88	2.29	12.1
79.2	15.6	5.20	29	76	1.09	10.9

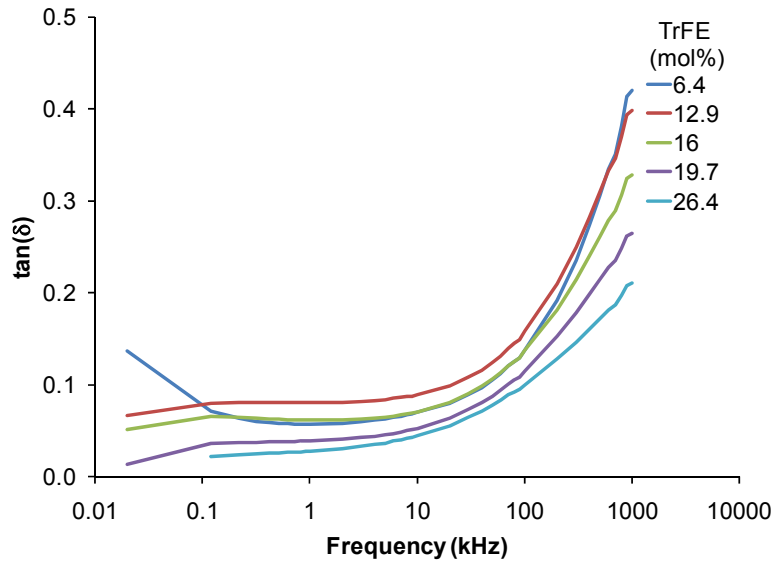
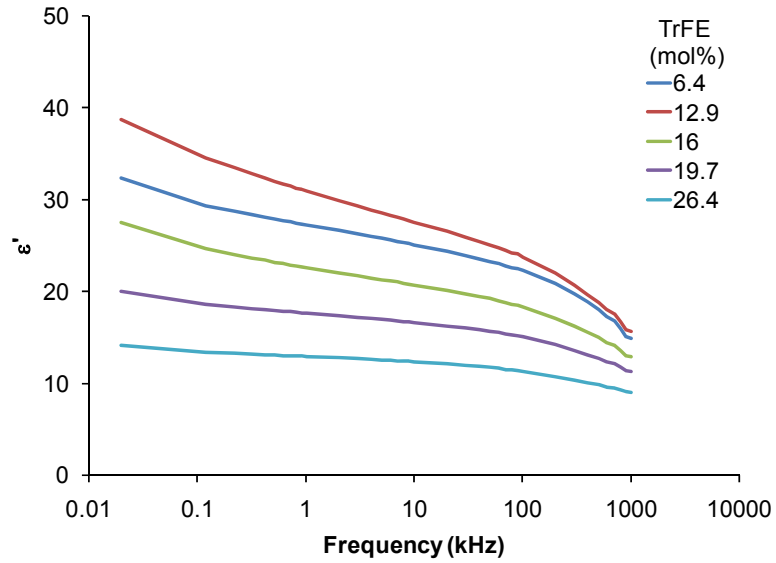
mol(%)			Heating			
			°C		J/g	
VDF	CTFE	TrFE	T _c	T _m	ΔH _c	ΔH _m
79.7	0.00	20.3	96	150	8.11	28.9
79.7	7.10	13.2	53	115	3.14	17.9
79.7	12.0	8.30	33	82	1.33	12.8
79.7	14.8	5.50	36	74	0.77	10.7
79.7	15.3	5.00	33	73	1.04	11.3

mol(%)			Heating			
			°C		J/g	
VDF	CTFE	TrFE	T _c	T _m	ΔH _c	ΔH _m
80.5	0.00	19.5	97	149	10.5	28.2
80.5	6.90	12.6	56	116	5.19	19.8
80.5	10.8	8.70	43	83	1.84	12.3
80.5	12.5	7.00	43	86	2.17	12.0

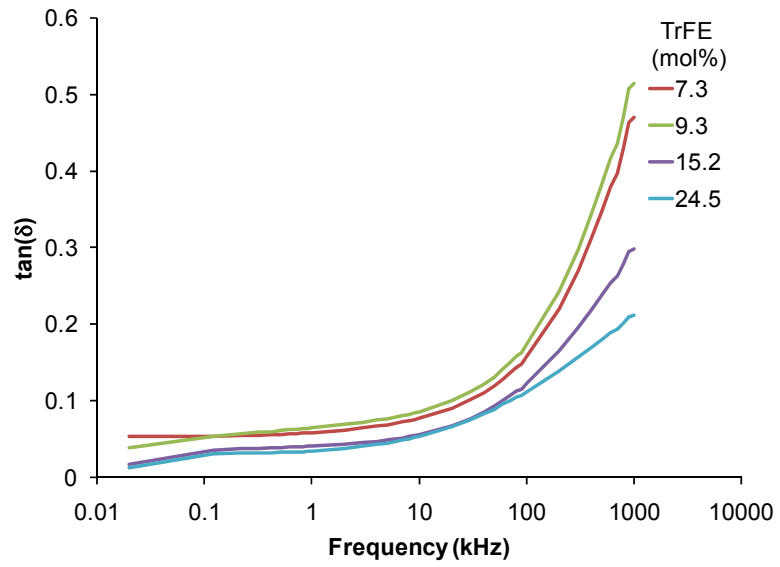
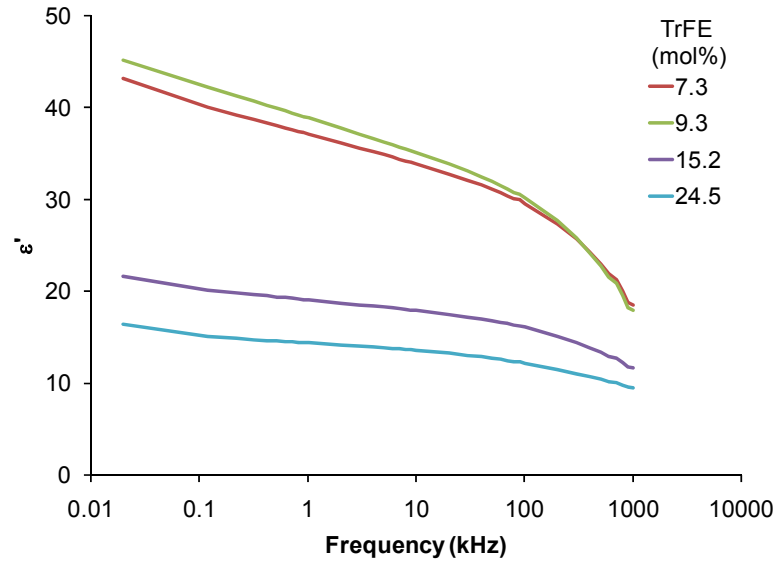
mol(%)			Heating			
			°C		J/g	
VDF	CTFE	TrFE	T _c	T _m	ΔH _c	ΔH _m
81.2	0.00	18.8	97	148	12.9	28.6
81.2	7.20	11.6	69	120	6.06	21.0
81.2	11.8	7.00	51	92	2.31	15.1
81.2	12.1	6.70	51	90	1.60	13.8
81.2	16.2	2.60	-	65	-	11.9

mol(%)			Heating			
			°C		J/g	
VDF	CTFE	TrFE	T _c	T _m	ΔH _c	ΔH _m
84.4	0.00	15.6	102	146/124	15.2	45.6
84.4	4.60	11.0	67	123/95	10.9	32.7
84.4	9.20	6.40	-	110/100	-	21.0
84.4	10.6	5.00	-	105/95	-	20.5
84.4	13.5	2.10	-	99/84	-	14.8

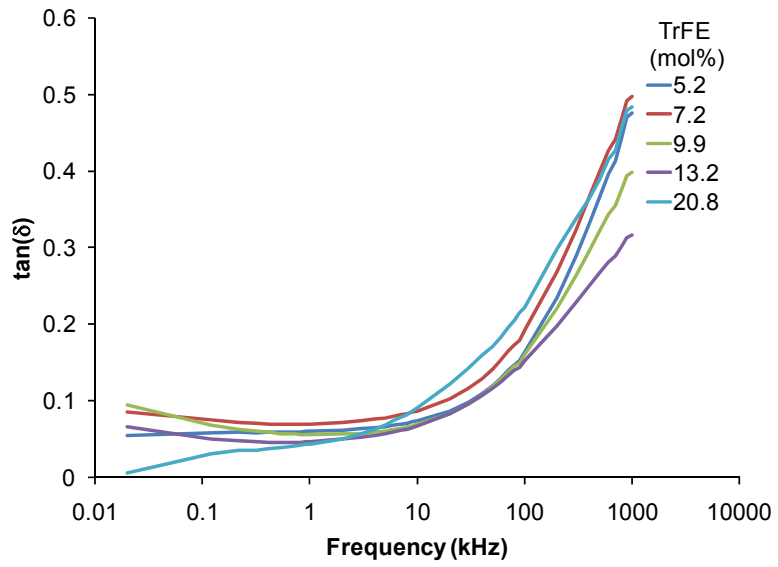
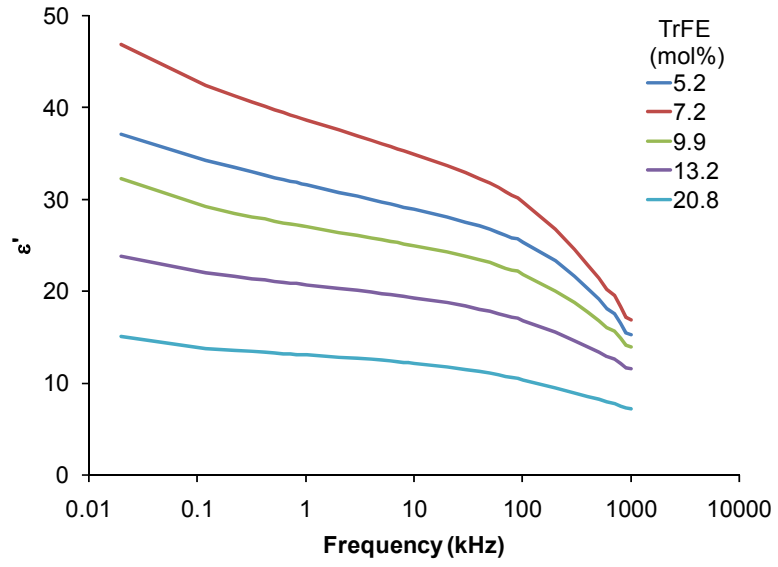
APPENDIX B: DIELECTRIC PROPERTIES OF THE HYDROGENATED POLYMERS



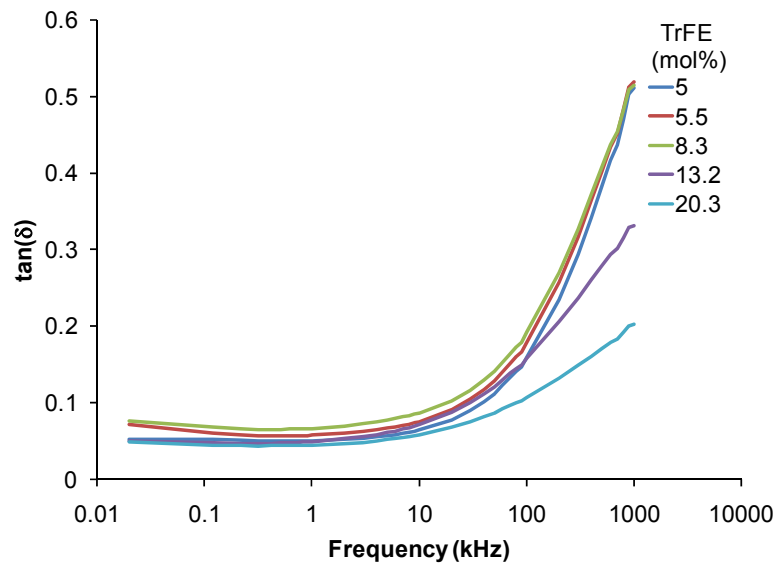
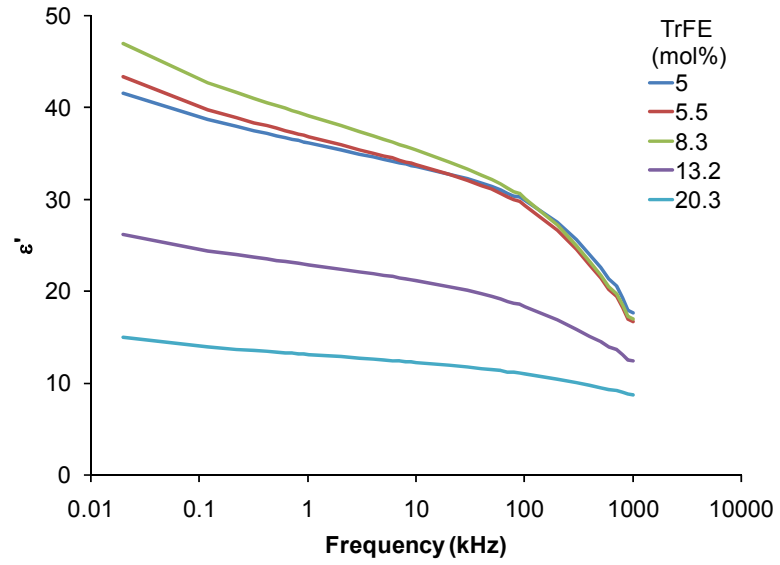
Room temperature permittivity and loss tangent versus frequency for the 73.6 VDF mol% polymers.



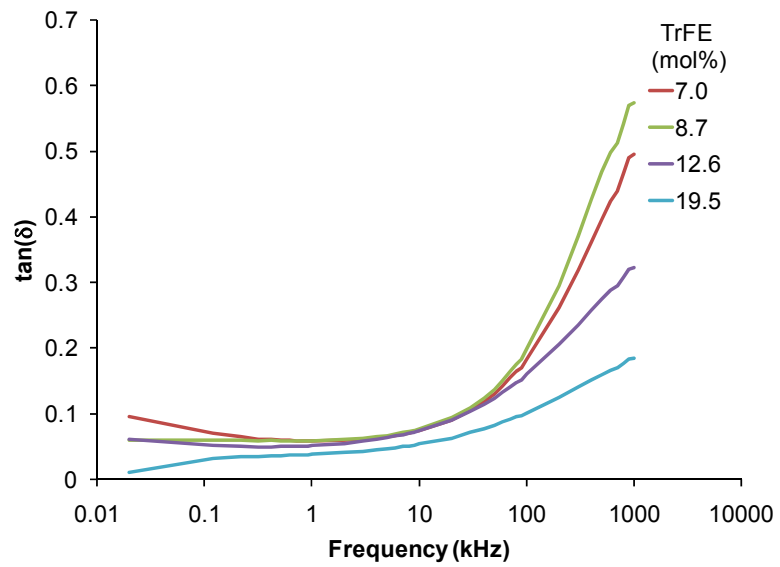
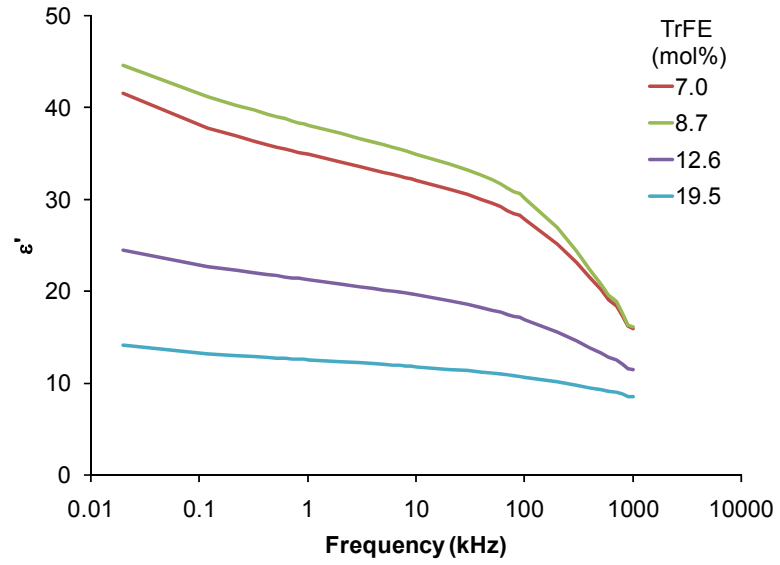
Room temperature permittivity and loss tangent versus frequency for the 75.5 VDF mol% polymers.



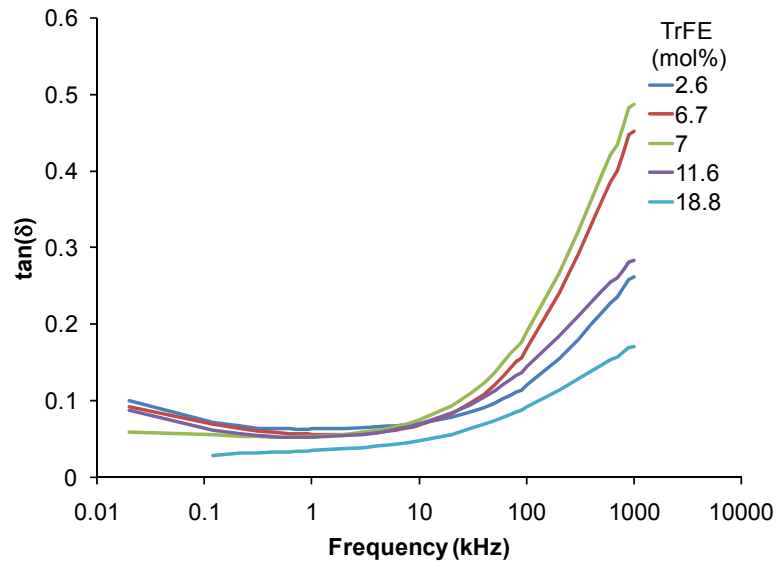
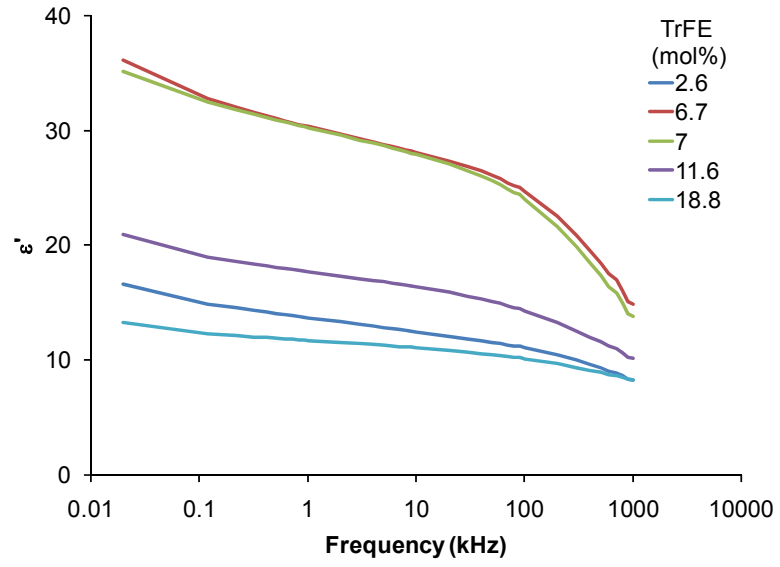
Room temperature permittivity and loss tangent versus frequency for the 79.2 VDF mol% polymers.



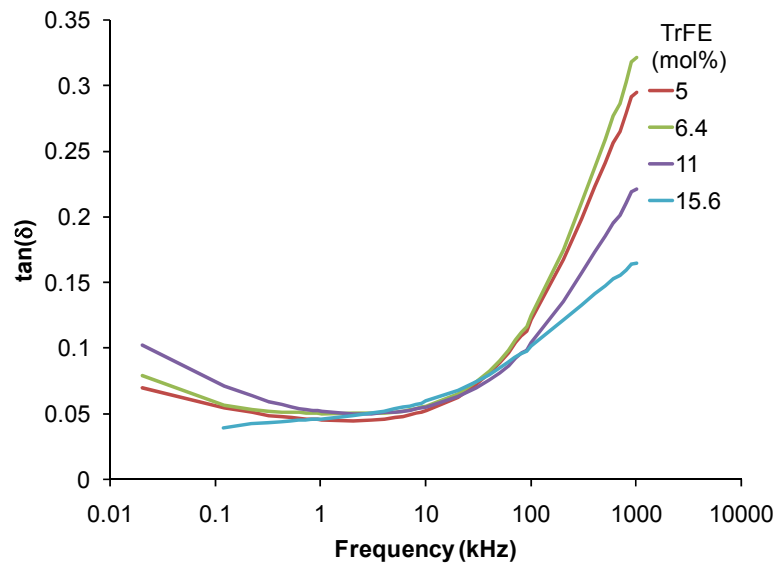
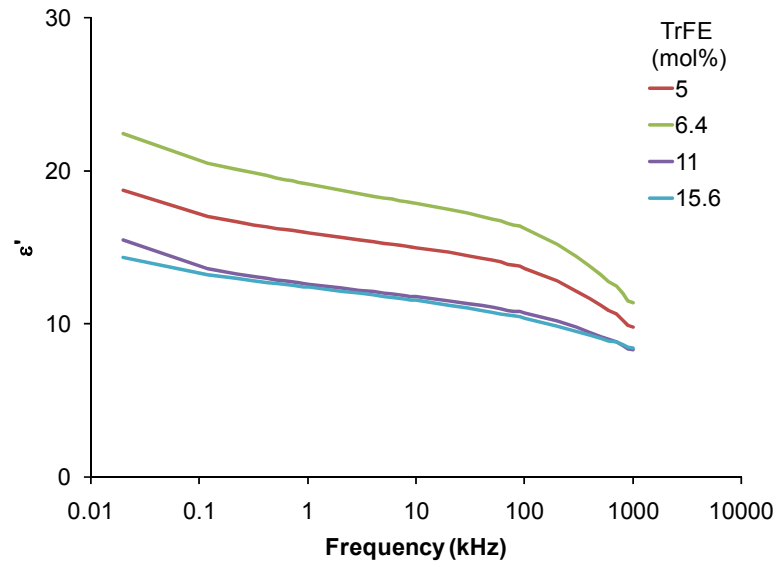
Room temperature permittivity and loss tangent versus frequency for the 79.7 VDF mol% polymers.



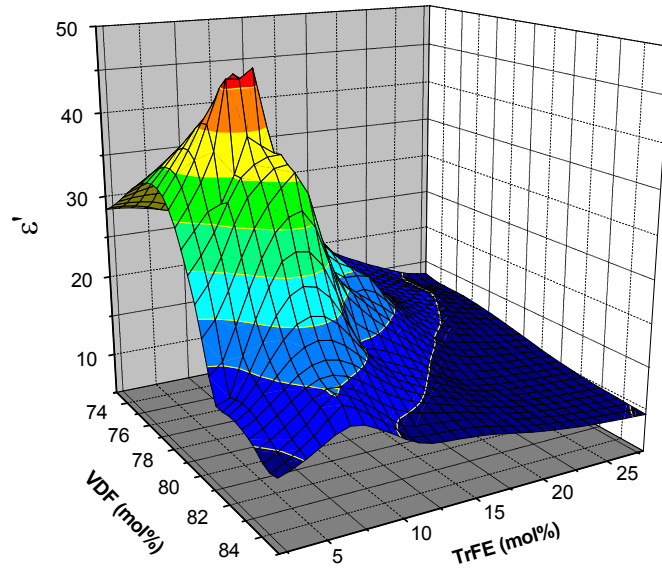
Room temperature permittivity and loss tangent versus frequency for the 80.5 VDF mol% polymers.



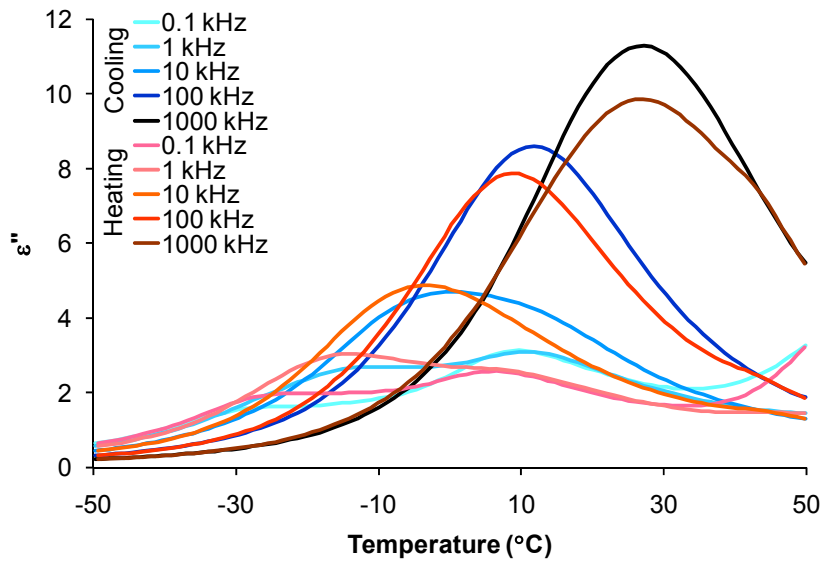
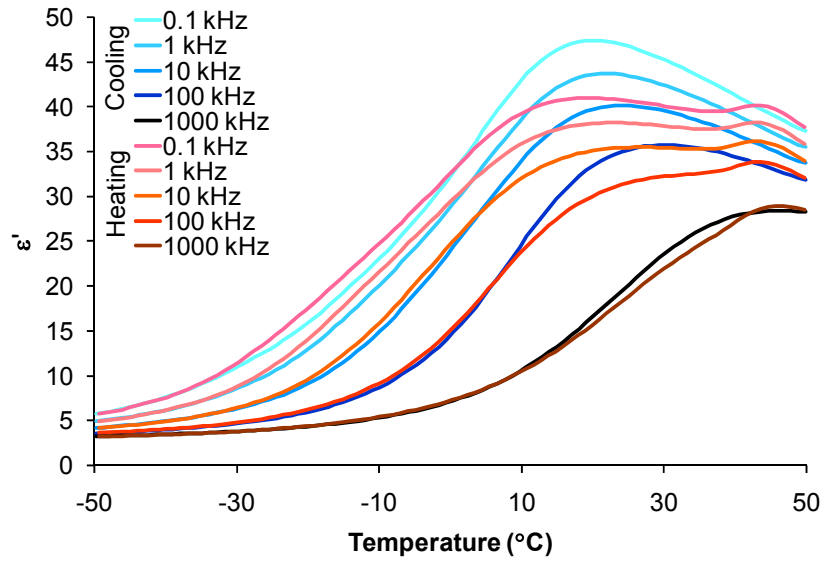
Room temperature permittivity and loss tangent versus frequency for the 81.2 VDF mol% polymers.



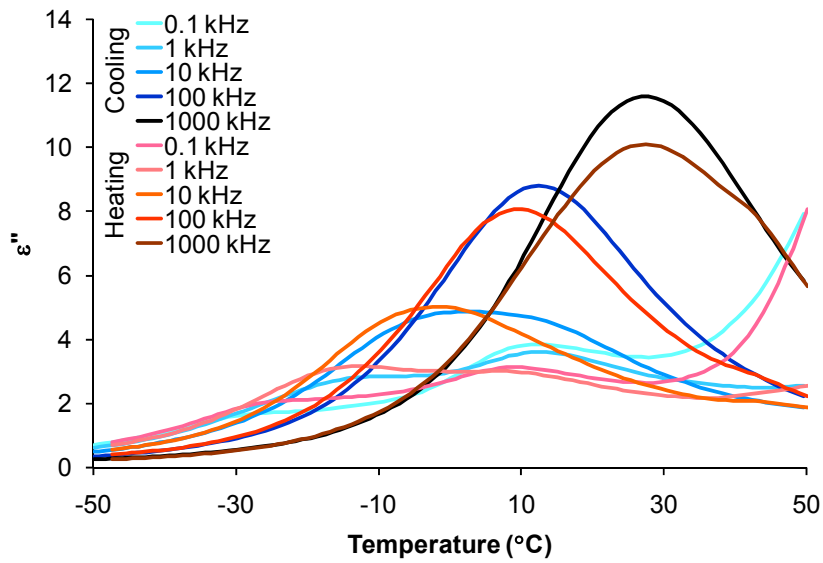
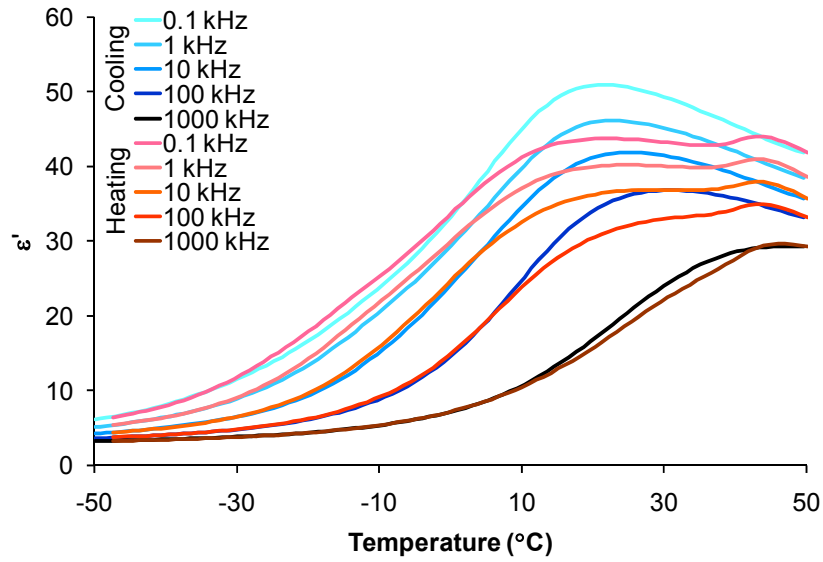
Room temperature permittivity and loss tangent versus frequency for the 84.4 VDF mol% polymers.



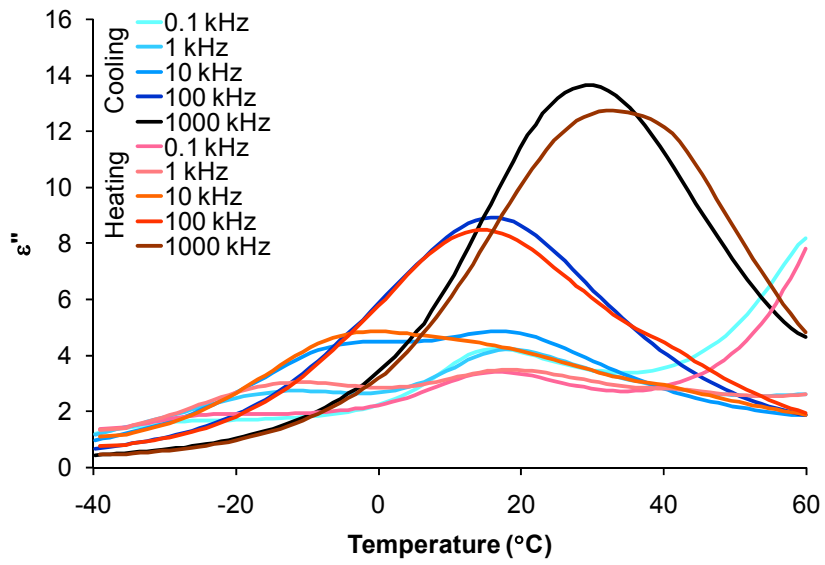
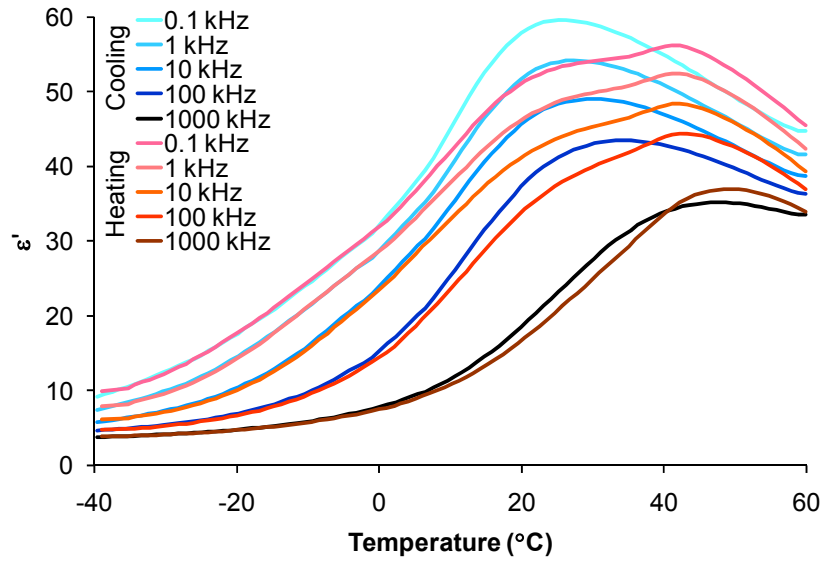
Three dimensional surface of permittivity as a function of chemical composition. Values are measured at room temperature and 1kHz.



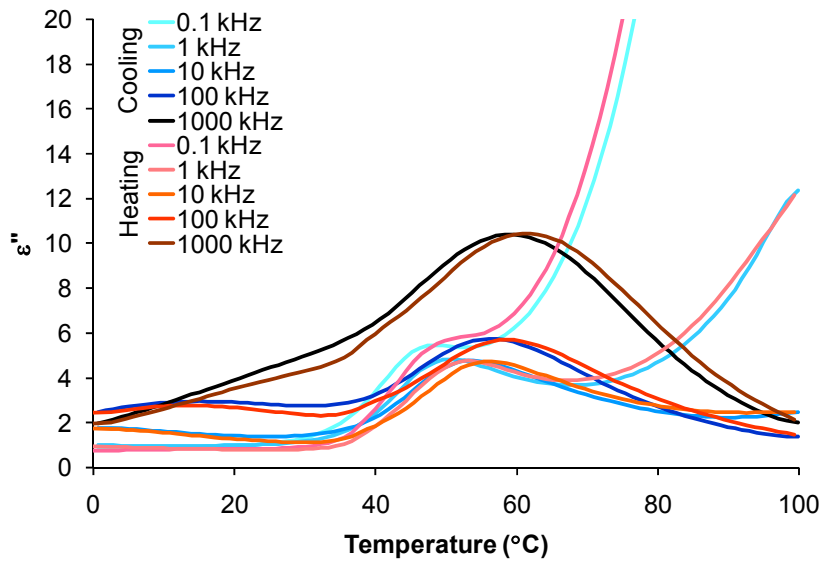
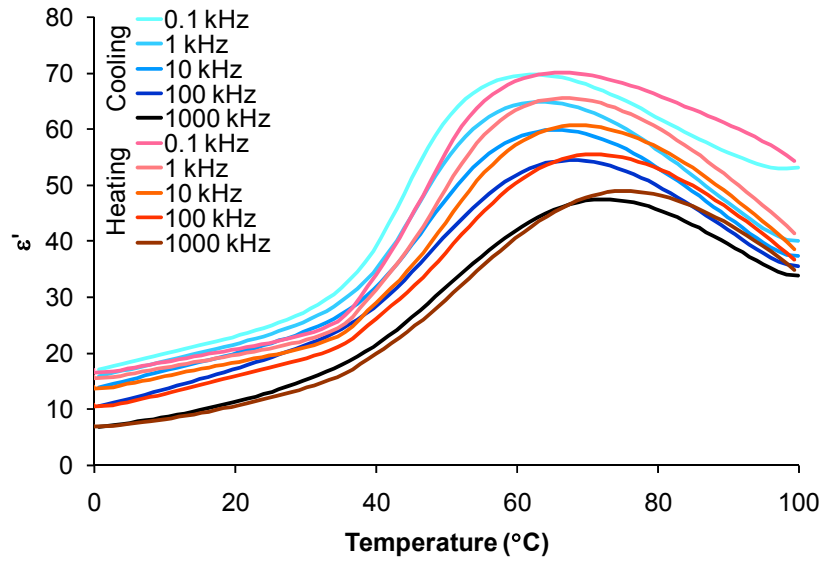
Temperature varying dielectric properties for the P(VDF-CTFE-TrFE) 78.8/16.2/5.0 mol%.



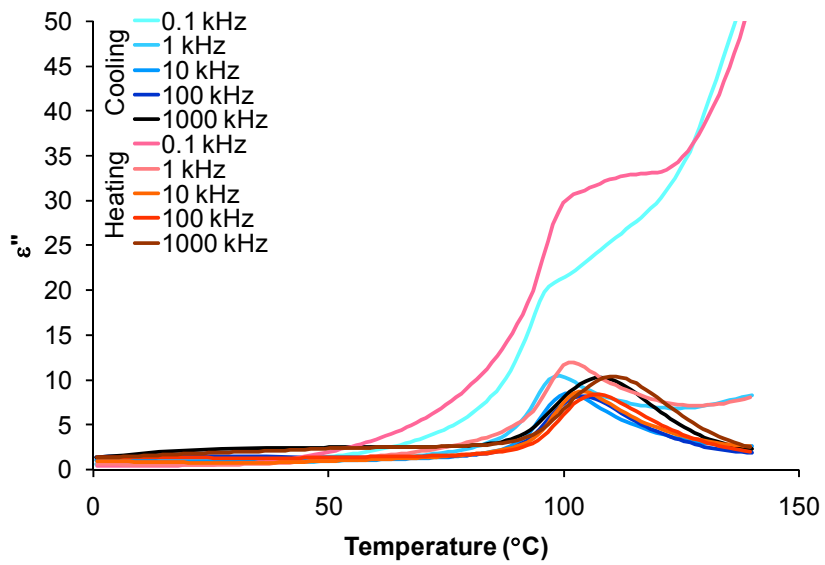
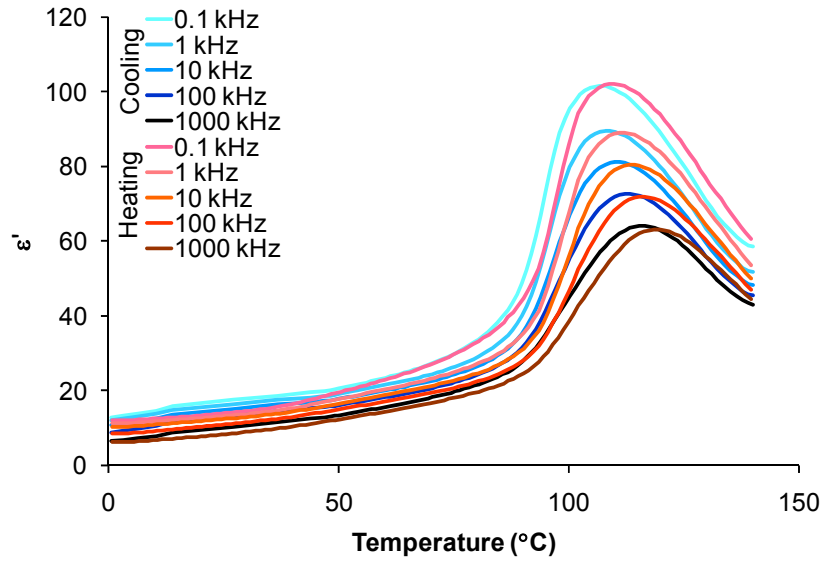
Temperature varying dielectric properties for the P(VDF-CTFE-TrFE) 78.8/15.8/5.4 mol%.



Temperature varying dielectric properties for the P(VDF-CTFE-TrFE) 78.8/14.0//7.2 mol%.

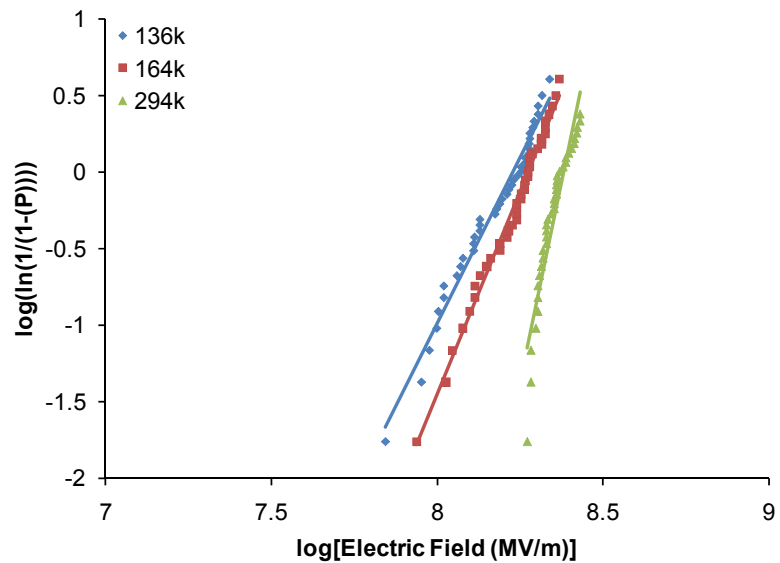


Temperature varying dielectric properties for the P(VDF-CTFE-TrFE) 78.8/6.0/15.2 mol%.

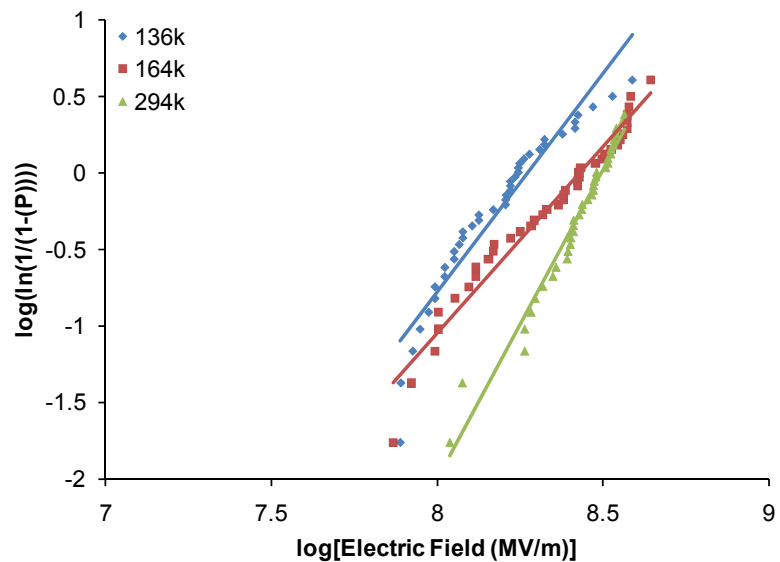


Temperature varying dielectric properties for the P(VDF-CTFE-TrFE) 78.8/0.0/21.2 mol%.

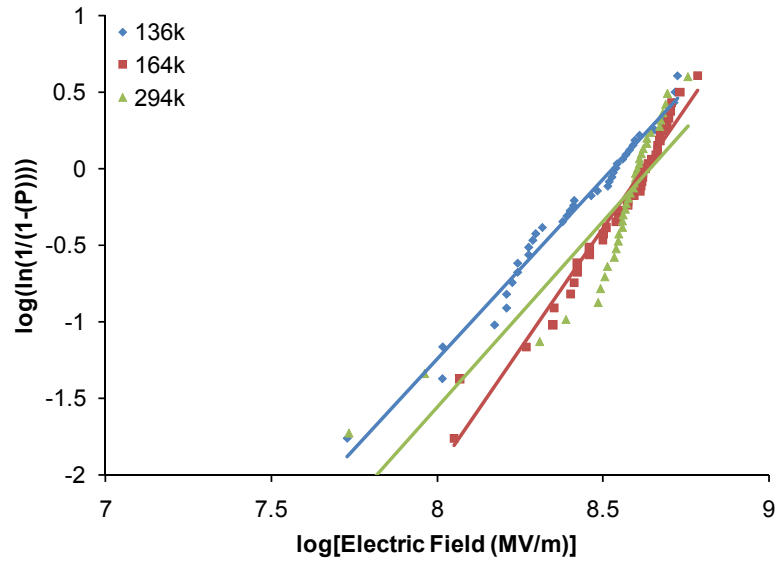
APPENDIX C: WEIBULL PLOTS FOR THE P(VDF-CTFE) 78.4-21.6 MOL% COPOLYMERS



Weibull plot at 25°C for the P(VDF-CTFE) copolymers.



Weibull plot at -15°C for the P(VDF-CTFE) copolymers.



Weibull plot at -35°C for the P(VDF-CTFE) copolymers.

M_n (kg/mol)	-35°C		-15°C		25°C	
	α (MV/m)	β	α (MV/m)	β	α (MV/m)	β
136	339	2.35	187	2.86	170	4.34
164	422	3.15	269	2.44	188	5.31
294	438	2.44	312	4.11	244	9.59

Summarized calculated parameters for the Weibull plots of the copolymers at the three different temperatures.

APPENDIX D: DERIVATION OF THE TEMPERATURE VERSUS ELECTRIC FIELD EQUATION

Terms

- V - voltage
- R - voltage ramp rate
- t - time
- E - electric field
- d - thickness
- C - heat capacity
- D - density
- σ - conductivity
- T - temperature
- T_s - starting temperature
- T_o - ambient temperature
- σ_o, g, a - constants

Voltage as a function of rate and time

$$1 \quad V = Rt$$

Definition of electric field

$$2 \quad E = \frac{V}{d}$$

Take derivative of (1)

$$3 \quad d(V) = d(Rt)$$

Substitute (2) into (3)

$$4 \quad d(Ed) = d(Rt)$$

Solve for dt

$$5 \quad dt = \left(\frac{d}{R}\right)dE$$

Impulse thermal breakdown

$$6 \quad CD\left(\frac{dT}{dt}\right) = \sigma(T, E)E^2$$

Conductivity as a function of electric field and temperature

$$7 \quad \sigma = \sigma_o \exp[gE + a(T - T_o)]$$

Substitute (7) into (6)

$$8 \quad \frac{CDR}{d}\left(\frac{dT}{dE}\right) = \sigma_o \exp[gE + a(T - T_o)]E^2$$

Rearrange temperature and electric field terms

$$9 \quad \frac{CDR}{d} \exp(-a(T - T_o))dT = \sigma_o \exp(gE)E^2 dE$$

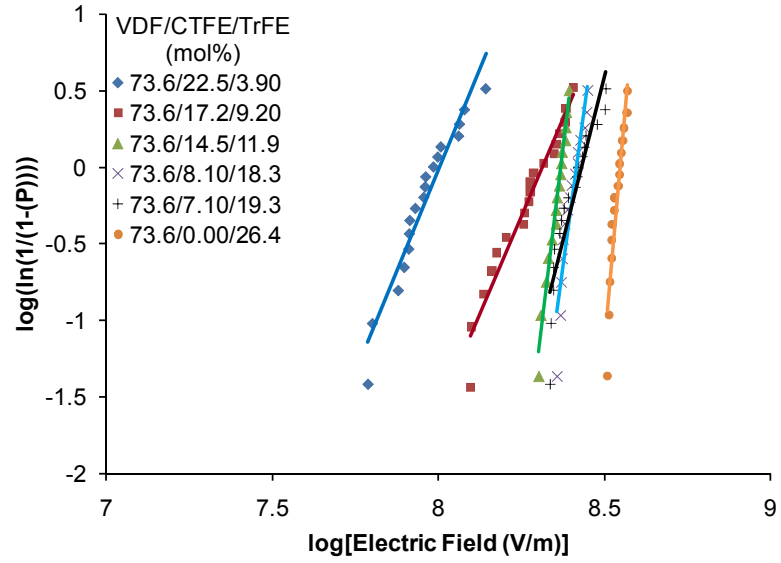
Integrate both sides

$$10 \quad \int_{T_s}^T \frac{CDR}{d} \exp(-a(T - T_o))dT = \int_0^E \sigma_o \exp(gE)E^2 dE$$

T as a function of electric field solved for the integrated equation

$$\mathbf{11} \quad T = -\frac{1}{a} \ln \left[\left\{ \left(\frac{-\sigma_o da}{CDR} \right) \exp(-aT_o) \left(\exp(gE) \left(\frac{E^2}{g} - \frac{2E}{g^2} + \frac{2}{g^3} \right) - \frac{2}{g^3} \right) \right\} + \exp(-aT_s) \right]$$

APPENDIX E: WEIBULL PLOTS FOR THE 73.6 MOL% VDF POLYMERS



Weibull plot at 25°C for the 73.6 mol% VDF polymers.

VDF (mol%)	CTFE (mol%)	TrFE (mol%)	α (MV/m)	β
73.6	22.5	3.9	101 (± 3.14)	5.29
73.6	17.2	9.2	205 (± 6.65)	5.10
73.6	14.5	11.9	234 (± 2.15)	17.99
73.6	8.1	18.3	261 (± 2.72)	15.84
73.6	7.1	19.3	271 (± 5.22)	8.56
73.6	0.0	26.4	353 (± 2.41)	24.3

Weibull constants at 25°C for the 73.6 mol% VDF polymers.

APPENDIX F: DERIVATION OF THE ELECTROSTATIC MAXWELL STRESS

Terms

F - force

q - charge (assumed constant)

E - electric field

W - energy

V - voltage

s - thickness (assumed constant)

U - energy density

A - area

σ - stress

Force on a charge

$$1 \quad F = qE$$

Derivate of force

$$2 \quad dF = qdE + Edq = qdE$$

Stored energy of the charge

$$3 \quad W = \int qdV$$

Derivative of electric field

$$4 \quad dE = \frac{dV}{s} + d\left(\frac{1}{s}\right)V = \frac{dV}{s}$$

Solve 4 for dV

$$5 \quad dV = sdE$$

Energy density related to stress by equations 2, 3, and 5

$$6 \quad U = \frac{W}{As} = \int \frac{sqdE}{As} = \int \frac{dF}{A} = \sigma$$

APPENDIX G: CONSTANTS FOR THE ELECTROMECHANICAL STRESS CALCULATIONS

VDF	CTFE	TrFE	Q	Y
	(mol%)		m⁴/C²	(MPa)
73.6	7.10	19.3	8	400
73.6	0.00	26.4	2.5	730

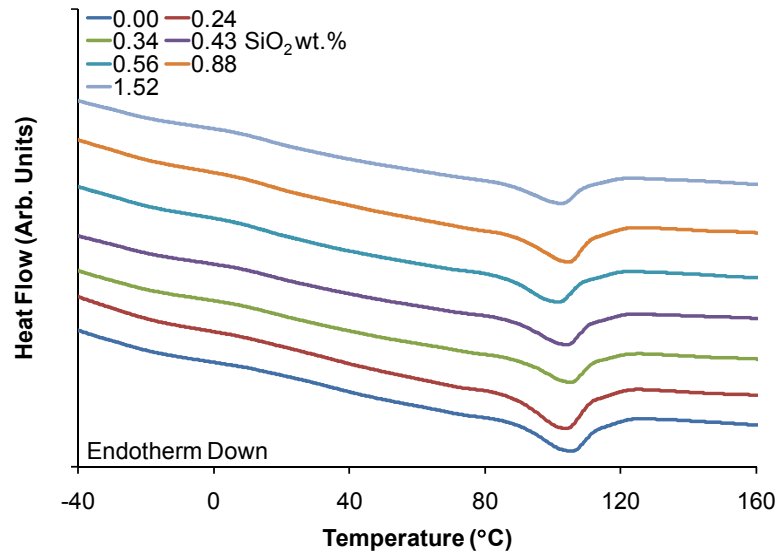
Constants for the electromechanical stress calculations.

Taken from references:

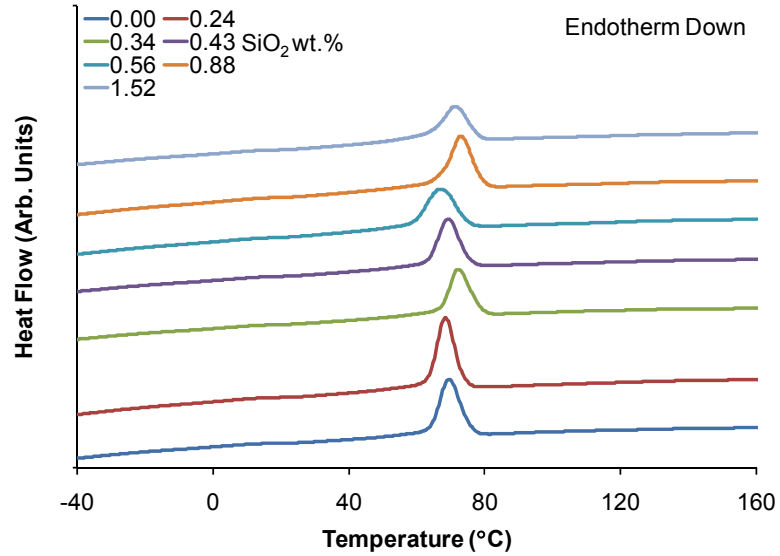
Cheng, Z.-Y.; Bharti, V.; Xu, T.-B.; Xu, H.; Mai, T.; Zhang, Q.M.. Electrostrictive poly(vinylidene fluoride-trifluoroethylene) copolymers. *Sens. Actuators, A* **2001**, *90*, 138-147.

Serrado Nunes, J.; Kouvatov, A.; Mueller, V.; Beige, H.; Brandao, P. M.; Belsley, M.; Moreira, M. V.; Lanceros-Mendez, S.. Piezoelectric and Optical Response of Uniaxially Stretched (VDF/TrFE) (75/25) Copolymer Films. *Materials Science Forum* **2006**, *514-516*, 945-949.

APPENDIX H: THERMAL PROPERTIES OF THE SiO_2 -P(VDF-CTFE) HYBRIDS

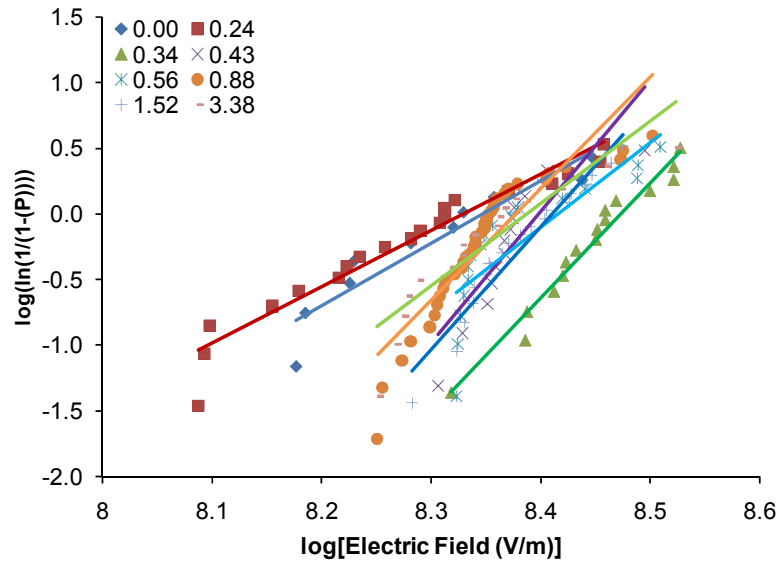


DSC heating curve for the SiO_2 -P(VDF-CTFE) hybrids.



DSC cooling curve for the SiO_2 -P(VDF-CTFE) hybrids.

APPENDIX I: ELECTRICAL BREAKDOWN DATA FOR THE SiO₂-P(VDF-CTFE) HYBRIDS

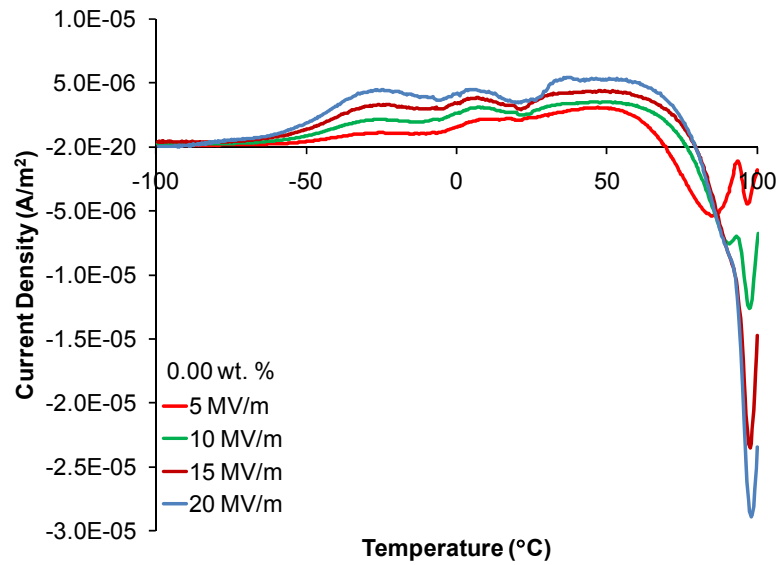


Weibull plot for the SiO₂-P(VDF-CTFE) hybrids at 25°C.

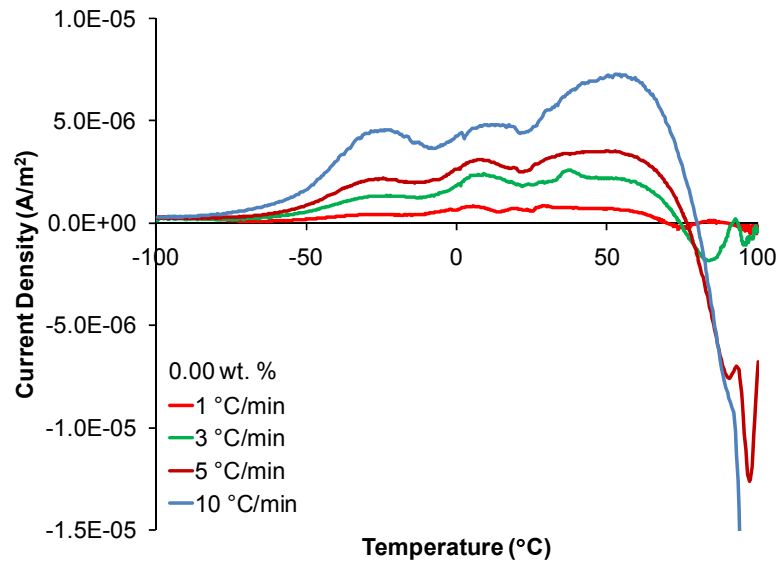
SiO ₂ (wt.%)	α (MV/m)	β
0.00	222 (± 7.73)	4.75
0.24	214 (± 8.24)	4.28
0.34	297 (± 5.61)	8.76
0.43	250 (± 4.13)	10.0
0.56	261 (± 6.65)	6.47
0.88	234 (± 4.64)	8.49
1.52	257 (± 4.54)	9.36
3.38	244 (± 6.42)	6.28

Computed Weibull constants for the SiO₂-P(VDF-CTFE) hybrids at 25°C.

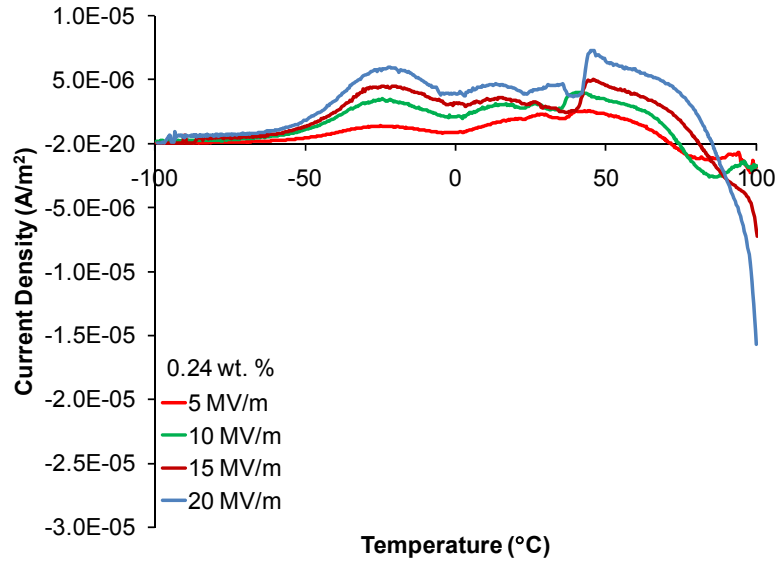
APPENDIX J: THERMALLY STIMULATED DISCHARGE CURRENT DATA FOR THE SiO_2 -P(VDF-CTFE)



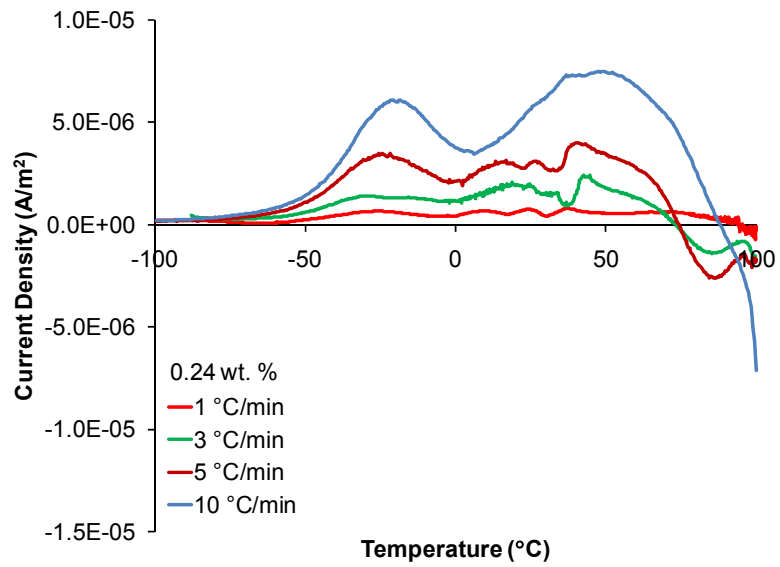
TSDC curves for the 0.00 wt. % hybrid at a constant heating rate of 5°C/min.



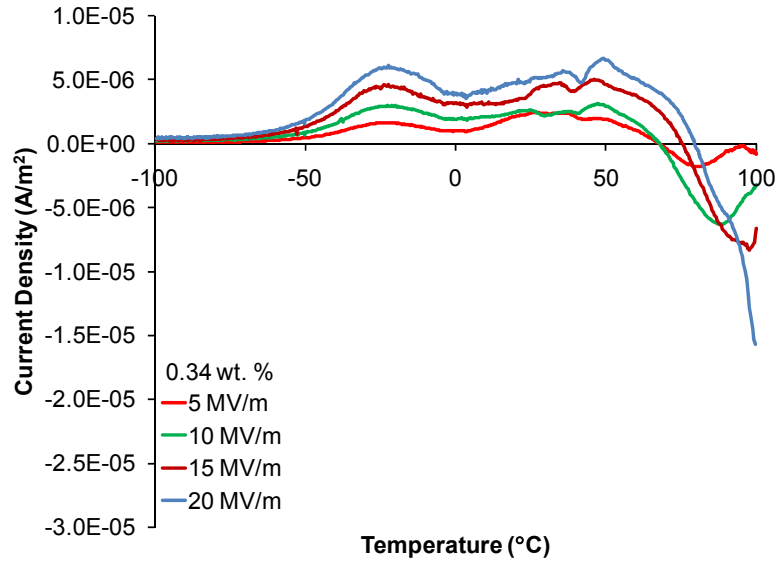
TSDC curves for the 0.00 wt. % hybrid at a constant poling rate of 10 MV/m.



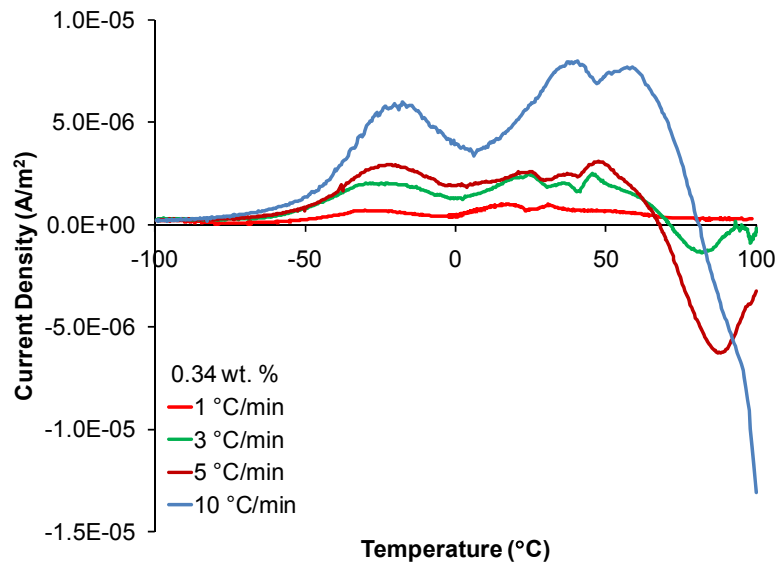
TSDC curves for the 0.24 wt. % hybrid at a constant heating rate of 5°C/min.



TSDC curves for the 0.24 wt. % hybrid at a constant poling rate of 10 MV/m.



TSDC curves for the 0.34 wt. % hybrid at a constant heating rate of 5°C/min.



TSDC curves for the 0.34 wt. % hybrid at a constant poling rate of 10 MV/m.

REFERENCES

- 1 - Encyclopædia Britannica Inc.. Capacitance. *The New Encyclopædia Britannica*, 15th ed.; Encyclopædia Britannica: Chicago, 2007; Volume 2, 823.
- 2 - Encyclopædia Britannica Inc.. Electricity and Magnetism. *The New Encyclopædia Britannica*, 15th ed.; Encyclopædia Britannica: Chicago, 2007; Volume 18, 189.
- 3 - Williams, H.S.. The Leyden Jar Discovered. *A History of Science : in Five Volumes. Volumes II: The Beginnings of Modern Science*; Harper & Brothers: New York, 1904; 279-285.
- 4 - Houston, E.J.. Chapter V Von Kleist and the Leyden Jar. *Electricity in every-day life*; Collier & Son: New York, 1905; Volume 1, 71-84.
- 5 - Bernal, J.D.. Electricity and Magnetism. *A History of Classical Physics: From Antiquity to the Quantum*; Barnes & Noble: New York, 1997; 285-288.
- 6 - Segré, E.. Electricity: From Thunder to Motors and Waves. *From Falling Bodies to Radio Waves. Classical Physicists and Their Discoveries*; W.H. Freeman and Company: New York, 1984; 109-112.
- 7 - Livingston, J.D.. Insulator and Capacitors. *Electronic Properties of Engineering Materials*; John Wiley & Sons: New York, 1999; 39-52.
- 8 - Kasap, S.O.. Dielectric Materials and Insulation. *Principles of Electronic Materials and Devices*, 2nd ed.; Tata McGraw-Hill Publishing Company Limited: New Delhi, 2000; 507-575.
- 9 - Blythe, T.; Bloor, D.. Dielectric Relaxation. *Electrical Properties of Polymers*, 2nd ed.; Cambridge University Press: New York, 2005; 58-110.
- 10 - Halliday, D.; Resnick, R.; Krane, K.. Capacitors and Dielectrics. *Physics*, 4th ed.; John Wiley & Sons: New York, 1992; Volume 2, 677-690.
- 11 - Kotz, R.; Carlen, M.. Principles and applications of electrochemical capacitors. *Electrochim. Acta* **2000**, *45*, 2483-2498.
- 12 - Winter, M.; Brodd, R.. What are batteries, fuel cells, and supercapacitors? *Chem. Rev.* **2004**, *104*, 4245-4269.
- 13 - Conway, B.E.. *Electrochemical Supercapacitors: Scientific Fundamentals and Technological Applications*; Kluwer Academic: New York, 1999.
- 14 - Young, L.. Electrolytic Capacitors. *Anodic oxide films*; Academic Press: New York, 1961, 181-185.
- 15 - Deeley, P. M.. *Electrolytic Capacitors*; The Cornell-Dubilier Electric Corp.: New Jersey, 1938.
- 16 - Moulson, A.J.; Herbert, J.M.. Dielectrics and Insulators. *Electroceramics*, 2nd ed.; Wiley: New Jersey, 2003; 243-337.
- 17 - Klose, P.H.. Electrical Properties of Manganese Dioxide and Manganese Sesquioxide. *J. Electrochem. Soc.* **1970**, *117*, 854-858.
- 18 - Cross, L.E.. Ceramic Capacitor Technology. In *Handbook of Solid State Batteries & Capacitors*; Munshi, M.Z.A., Ed.; World Scientific: New Jersey, 1995; 663-687.
- 19 - Moulson, A.J.; Herbert, J.M.. Elementary Solid State Science. *Electroceramics*, 2nd ed.; Wiley: New Jersey, 2003; 5-93.
- 20 - Gregor, L.V.. Polymer Dielectric Films. *IBM Journal of Research and Development* **1968**, *12*, 140-162.

- 21 - Jow, J.R.; Cygan, P.J.. Dielectric breakdown of polyvinylidene fluoride and its comparisons with other polymers. *J. Appl. Phys.* **1993**, *73*, 5147-5151.
- 22 - Picci, G.; Rabuffi, M.. Status Quo and Future Prospects for Metallized Polypropylene Energy Storage Capacitors. In *Pulsed Power Plasma Science, 2001. PPPS-2001. Digest of Technical Papers*, Las Vegas, NV, June 2001; IEEE: New Jersey, 2001; 417-420.
- 23 - Anderson, R.. Select the Right Plastic Film Capacitor for your Power Electronic Application. In *Industry Applications Conference, 1996. Thirty-First IAS Annual Meeting, IAS '96., Conference Record of the 1996 IEEE*, San Diego, CA, October 1996; IEEE: New Jersey, 1996; 1327-1330.
- 24 - Yializis, A.. Metallized Capacitors. In *Handbook of Solid State Batteries & Capacitors*; Munshi, M.Z.A., Ed.; World Scientific: New Jersey, 1995; 645-662.
- 25 - Kerrigan, R.. New Polymer Film Type Capacitor for High Frequency High Voltage Applications. *Electronic Components and Technology Conference, 1994. Proceedings., 44th*; IEEE: New Jersey, 1994; 248-254.
- 26 - Yen, S.P.S; Lewis, C.R.; Jow, T.R; Cygan, P.J.. Development of High Temperature Polyimide Dielectric Film for Lead and Surface Mount Capacitor Application. In *Power Sources Symposium, 1992., IEEE 35th International*; IEEE: New Jersey, 1992; 363-366.
- 27 - Christen, T.; Carlen, M.W.. Theory of Ragone plots. *J. Power Sources* **2000**, *91*, 210-216.
- 28 - Kawai, H.. The Piezoelectricity of Poly(vinylidene Fluoride). *Jpn. J. Appl. Phys.* **1969**, *8*, 975-976.
- 29 - Torres, A.; Jiménez, B.; Vega, B.; De Saja, J.A.. Thermally stimulated depolarization currents in PVDF- α : a dipolar interaction approach to β and γ transitions. *J. Mater. Sci.* **1987**, *22*, 1623-1629.
- 30 - Lovinger, A.J.. Ferroelectric Polymers. *Science* **1983**, *220*, 1115-1121.
- 31 - Lovinger, A.J.. Poly(vinylidene fluoride). In *Developments in crystalline polymers-1*; Bassett, D.C., Ed.; Applied Science Publishers: New Jersey, 1982; 195-273.
- 32 - Furukawa, T.. Ferroelectric Properties of Vinylidene Fluoride Copolymers. *Phase Transitions* **1989**, *18*, 143-211.
- 33 - Lovinger, A.J.. Unit Cell of the γ Phase of Poly(vinylidene fluoride). *Macromolecules* **1981**, *14*, 322-325.
- 34 - Furukawa, T.; Ohuchi, M.; Chiba, A.; Date, M.. Dielectric Relaxations and Molecular Motions in Homopolymers and Copolymers of Vinylidene Fluoride and Trifluoroethylene. *Macromolecules* **1984**, *17*, 1384-1390.
- 35 - Tashiro, K.; Kobayashi, M.. Structural Phase Transition in Ferroelectric Fluorine Polymers: X-Ray Diffraction and Infrared/Raman Spectroscopic Study. *Phase Transitions* **1989**, *18*, 213-246.
- 36 - Lovinger, A.J.; Furukawa, T.; Davis, G.T.; Broadhurst, M.G.. Crystallographic changes characterizing the Curie transition in the three ferroelectric copolymers of vinylidene fluoride and trifluoroethylene:1. As-crystallized samples. *Polymer* **1983**, *24*, 1255-1232.

- 37 - Lovinger, A.J.; Davis, G.T.; Furukawa, T.; Broadhurst, M.G.. Crystalline Forms in a Copolymer of Vinylidene Fluoride and Trifluoroethylene (52/49 mol %). *Macromolecules* **1982**, *15*, 323-328.
- 38 - Bharti, V.; Zhang, Q.M.. Dielectric study of the relaxor ferroelectric poly(vinylidene fluoride-trifluoroethylene co-polymer system). *Phys. Rev. B* **2001**, *63*, 184103-1-184103-6.
- 39 - Furukawa, T.; Seo, N.. Electrostriction as the Origin of Piezoelectricity in Ferroelectric Polymers. *Jpn. J. Appl. Phys.* **1990**, *29*, 675-680.
- 40 - Zhang, Q.M.; Bharti, V.; Zhao, X.. Giant Electrostriction and Relaxor Ferroelectric Behavior in Electron-Irradiated Poly(vinylidene fluoride-trifluoroethylene) Copolymer. *Science* **1998**, *280*, 2101-2104.
- 41 - Lovinger, A.. Polymorphic Transformations in Ferroelectric Copolymers of Vinylidene Fluoride Induced by Electron Irradiation. *Macromolecules* **1985**, *18*, 910-918.
- 42 - Zhang, Q.M.; Cheng, Z.Y.; Bharti, V.. Relaxor ferroelectric behavior in high-energy electron-irradiated poly(vinylidene fluoride-trifluoroethylene) copolymers. *Appl. Phys. A* **2000**, *70*, 307-312.
- 43 - Chung, T.C.; Petchsuk, A.. Synthesis and Properties of Ferroelectric Fluoroterpolymers with Curie Transition at Ambient Temperature. *Macromolecules* **2002**, *35*, 7678-7684.
- 44 - McMurry, J.; Robert, C.F.. Periodicity and Atomic Structure. *Chemistry*, 3rd ed.; Prentice Hall: New Jersey, 2001; 159-200.
- 45 - Moggi, G.; Bonardelli, P.; Bart, J.C.J.. Copolymers of 1,1-Difluoroethene with Tetrafluoroethene, Chlorotrifluoroethene, and Bromotrifluoroethene. *J. Polym. Sci. Polym. Phys.* **1984**, *22*, 357-365.
- 46 - Yagi, T.; Tatemoto, M.. A Fluorine-19 NMR Study of the Microstructure of Vinylidene Fluoride-Trifluoroethylene Copolymers. *Polym. J.* **1979**, *11*, 429-436.
- 47 - Lu, Y.; Claude, J.; Zhang, Q.; Wang, Q.. Microstructures and Dielectric Properties of the Ferroelectric Fluoropolymers Synthesized via Reductive Dechlorination of Poly(vinylidene fluoride-co-chlorotrifluoroethylene)s. *Macromolecules* **2006**, *39*, 6962-6968.
- 48 - Kim, K.J.; Kim, G.B.; Vanlencia, C.; Rabolt, J.F.. Curie Transition, Ferroelectric Crystal Structure, and Ferroelectricity of a VDF/TrFE(75/25) Copolymer 1. The Effect of the Consecutive Annealing in the Ferroelectric State on Curie Transition and Ferroelectric Crystal Structure. *J. Polym. Sci., Part B: Polym. Phys.* **1994**, *32*, 2435-2444.
- 49 - Reynolds, N.M.; Kim, K.J.; Chang, C.; Hsu, S.L.. Spectroscopic Analysis of the Electric Field Induced Structural Changes in Vinylidene Fluoride/Trifluoroethylene Copolymers. *Macromolecules* **1989**, *22*, 1092-1100.
- 50 - Osaki, S.; Ishida, Y.. Effects of Annealing and Isothermal Crystallization upon Crystalline Forms of Poly(vinylidene Fluoride). *J. Polym. Sci.: Polym. Phys. Ed.* **1975**, *13*, 1071-1083.
- 51 - Sasabe, H.; Saito, S.; Asahuna, M.; Kakutan, H.. Dielectric Relaxations in Poly(vinylidene Fluoride). *J. Polym. Sci., Part A2*, 1969, *7*, 1405-1414.

- 52 - Zhang, S.; Klein, R.; Ren, K.; Chu, B.; Zhang, X.; Runt, J.; Zhang, Q.M.. Normal ferroelectric to ferroelectric relaxor conversion in fluorinated polymers and the relaxor dynamics. *J. Mater. Sci.* **2006**, *41*, 271-280.
- 53 - Dissado, L.; Fothergill, J.. Overview of electrical degradation and breakdown. *Electrical Degradation and Breakdown in Polymers*; Peter Peregrinus Ltd.: London, 1992; Vol. 9, 49-68.
- 54 - Dissado, L.; Fothergill, J.. Electronic breakdown. *Electrical Degradation and Breakdown in Polymers*; Peter Peregrinus Ltd.: London, 1992; Vol. 9, 271-286.
- 55 - Blythe, T.; Bloor, D.. Dielectric Breakdown. *Electrical Properties of Polymers*, 2nd ed.; Cambridge University Press: New York, 2005; 186-216.
- 56 - Dissado, L.; Fothergill, J.. Thermal breakdown. *Electrical Degradation and Breakdown in Polymers*; Peter Peregrinus Ltd.: London, 1992; Vol. 9, 242-262.
- 57 - Dissado, L.; Fothergill, J.. Electromechanical breakdown. *Electrical Degradation and Breakdown in Polymers*; Peter Peregrinus Ltd.: London, 1992; Vol. 9, 263-270.
- 58 - Dissado, L.; Fothergill, J.. Partial discharge and free volume breakdown. *Electrical Degradation and Breakdown in Polymers*; Peter Peregrinus Ltd.: London, 1992; Vol. 9, 287-316.
- 59 - Chu, B.; Zhou, X.; Ren, K.; Neese, B.; Lin, M.; Wang, Q.; Bauer, F.; Zhang, Q.M.. A Dielectric Polymer with High Electric Energy Density and Fast Discharge Speed. *Science* **2006**, *313*, 334-336.
- 60 - Dawber, M.; Farnan, I.; Scott, F.. A classroom experiment to demonstrate ferroelectric hysteresis. *Am. J. Phys.* **2003**, *9*, 819-822.
- 61 - Odian, G.. Radical Chain Polymerization. *Principles of Polymerization*, 4th ed.; Wiley Interscience: New Jersey, 2004; 198-349.
- 62 - Ward, I.M.; Sweeney, J.. Principles of Linear Viscoelasticity. *The Mechanical Properties of Solid Polymers*, 2nd ed.; John Wiley & Sons, Ltd.: England, 2004; 53-78.
- 63 - Ward, I.M.; Sweeney, J.. Yielding and Instability in Polymers. *The Mechanical Properties of Solid Polymers*, 2nd ed.; John Wiley & Sons, Ltd.: England, 2004; 241-271.
- 64 - Abernethy, R.. Plotting the data & interpreting the plot. *The New Weibull Handbook*, 2nd ed.; Robert B. Abernethy: Florida, 1993; 2-1 - 2-22.
- 65 - Johnson, L.. The Median Ranks of Sample Values In Their Population With An Application To Certain Fatigue Studies. *Industrial Mathematics* **1951**, *2*, 1-9.
- 66 - Stark, K.H.; Garton, C.G.. Electric Strength of Irradiated Polythene. *Nature* **1955**, *176*, 1225-1226.
- 67 - Ashby, M.F.; Jones, D.R.H.. The yield strength, tensile strength, hardness, and ductility. *Engineering Materials 1. An Introduction to their properties & Applications*, 2nd ed.; Butterworth Heinmann: Oxford, 1996; 77-92.
- 68 - Klein, N.; Burstein, E.. Electrical Pulse Breakdown of Silicon Oxide Films. *J. Appl. Phys.* **1969**, *40*, 2728-2740.
- 69 - Furukawa, T.; Seo, N.. Electrostriction as the Origin of Piezoelectricity in Ferroelectric Polymers. *Jpn. J. Appl. Phys.* **1990**, *29*, 675-680.
- 70 - Tajitsu, Y.; Chiba, A.; Furukawa, T.; Date, M.; Fukada, E.. Crystalline phase transition in the copolymer of vinylidene fluoride and trifluoroethylene. *Appl. Phys. Lett.* **1980**, *36*, 286-288.

- 71 - Xia, F.; Li, H.; Huang, C.; Huang, M. Y. M.; Xu, H.; Bauer, F.; Cheng, Z.-Y.; Zhang, Q. M.. Poly(vinylidene fluoride-trifluoroethylene) Based High Performance Electroactive Polymers. In *Smart Structures and Materials 2003. Electroactive Polymer Actuators and Devices (EAPAD)*, Ed: Y. Bar-Cohen, SPIE: Bellingham, Washington, United States of America, 2003; 133-142.
- 72 - Cheng, Z.-Y.; Xu, H.S.; Mai, T.; Chung, M.; Zhang, Q. M.. P(VDF-TrFE)-based Electrostrictive Co/Ter-polymers and its Device Performance. In *Smart Structures and Materials 2001. Electroactive Polymer Actuators and Devices (EAPAD)*, Ed: Y. Bar-Cohen, SPIE: Bellingham, Washington, United States of America, 2001; 106-116.
- 73 - Cheng, Z.-Y.; Bharti, V.; Xu, T.-B.; Xu, H.; Mai, T.; Zhang, Q.M.. Electrostrictive poly(vinylidene fluoride-trifluoroethylene) copolymers. *Sens. Actuators, A* **2001**, *90*, 138-147.
- 74 - Serrado Nunes, J.; Kouvatov, A.; Mueller, V.; Beige, H.; Brandao, P. M.; Belsley, M.; Moreira, M. V.; Lanceros-Mendez, S.. Piezoelectric and Optical Response of Uniaxially Stretched (VDF/TrFE) (75/25) Copolymer Films. *Materials Science Forum* **2006**, *514-516*, 945-949.
- 75 - Ieda, M.; Nagao, M.; Hikita, M.. Recent Progress of High Field Conduction and Breakdown in Insulating Polymers. Conduction and Breakdown in Solid Dielectrics, 1992., Proceedings of the 4th International Conference on,; IEEE: New Jersey, 1992; 383-392.
- 76 - Ueki, M.M.; Zanin, M.. Influence of Additives on the Dielectric Strength of High-density Polyethylene. *IEEE Transactions on Dielectric and Electrical Insulation* **1999**, *6*, 876-881.
- 77 - Tuncer, E.; Duckworth, R.C.; Sauers, I.; James, D.R.; Ellis, A.. Dielectric properties of polyvinyl alcohol filled with nanometer size barium titanate particles. 2007 Annual Report Conference on Electrical Insulation and Dielectric Phenomena,; IEEE: New Jersey, 2007; 225-227.
- 78 - Nelson, J.K.. The Promise of Dielectric Nanocomposites. Conference Record of the 2006 IEEE International Symposium on Electrical Insulation,; IEEE: New Jersey, 2006; 452-457.
- 79 - Kasap, S.O.. Electrical and Thermal Conduction in Solids. *Principles of Electronic Materials and Devices*, 2nd ed.; Tata McGraw-Hill Publishing Company Limited: New Delhi, 2000; 507-575.
- 80 - Nelson, J.K.; Fothergill, J.C.. Internal charge behavior of nanocomposites. *Nanotechnology* **2004**, *15*, 586-595.
- 81 - Fothergill, J.C.; Nelson, J.K., Fu, M.. Dielectric Properties of Epoxy Nanocomposites containing TiO₂, Al₂O₃, and ZnO fillers. 2004 Annual Report Conference on Electrical Insulation and Dielectric Phenomena,; IEEE: New Jersey, 2004; 406-409.
- 82 - Tuncer, E.; Sauers, I.; James, D.R.; Ellis, A.R.; Duckworth, R.C.. Nanodielectric System for Cryogenic Applications: Barium Titanate filled Polyvinyl Alcohol. *IEEE Transactions on Dielectric and Electrical Insulation* **2008**, *15*, 236-242.

- 83 - Dang, Z.M.; Wang, H.Y.; Xu, H.P.. Influence of silane coupling agent on morphology and dielectric property in BaTiO₃/polyvinylidene fluoride composites. *Appl. Phys. Lett.* **2006**, *89*, 112902-1 - 112902-3.
- 84 - Zhang, Q.M.; Li, H.; Poh, M.; Xia, F.; Cheng, Z.Y.; Xu, H.; Huang, C.. An all-organic composite actuator material with a high dielectric constant. *Nature* **2002**, *419*, 284-287.
- 85 - Lewis, T.J.. Interfaces: nanometric dielectrics. *J. Phys. D: Appl. Phys.* **2005**, *38*, 202-212.
- 86 - An, A.L.; Boggs, S.A.; Calame, J.. Energy Storage in Polymer Films with High Dielectric Constant Fillers. Conference Record of the 2006 IEEE International Symposium on Electrical Insulation,; IEEE: New Jersey, 2006; 466-469.
- 87 - Calame, J.. Microstructure-Based Simulation of the Dielectric Properties of Polymer-Ceramic Composites for Capacitor Applications. Materials Research Society Symposium Proceedings Volume 949,; Materials Research Society: Pennsylvania, 2007; 0949-C05-01.
- 88 - Coppard, R.W.; Bowman, J.; Dissado, L.A.; Rowland, S.M.; Rakowski, R.T.. The effect of aluminum inclusions on the dielectric breakdown of polyethylene. *J. Phys. D: Appl. Phys.* **1990**, *23*, 1554-1561.
- 89 - Hong, J.I.; Schadler, L.S.; Siegel, R.W.; Mårtensson, E.. Rescaled electrical properties of ZnO/low density polyethylene nanocomposites. *Appl. Phys. Lett.* **2003**, *82*, 1956-1958.
- 90 - Ma, D.; Siegel, R.W.; Hong, J.I.; Schadler, L.S.. Influence of nanoparticle surfaces on the electrical breakdown strength of nanoparticle-filled low-density polyethylene. *J. Mater. Res.* **2004**, *19*, 857-863.
- 91 - Murata, Y.; Sekiguchi, Y.; Inoue, Y.; Kanaoka, M.. Investigation of Electrical phenomena of Inorganic-filler/LDPE Nanocomposite Material. Proceedings of 2005 International Symposium on Electrical Insulating Materials, Kitakyushu, Japan, June 5-9 2005; IEEE: New Jersey, 2005; 650-653.
- 92 - Roy, M.; Reed, C.W.; MacCrone, R.K.; Schadler, L.S.; Nelson, J.K.; Keefe, R.; Zenger, W.. Evidence for the Role of the Interface in Polyolefin Nanocomposites. Proceedings of 2005 International Symposium on Electrical Insulating Materials, Kitakyushu, Japan, June 5-9 2005; IEEE: New Jersey, 2005; 233-226.
- 93 - Zilig, C.; Kämpfer, D.; Thomann, R.; Muelhaupt, R.; Montanari, G.C.. Electrical properties of polymer nanocomposites based upon organophilic layered silicates. 2003 Annual Report Conference on Electrical Insulation and Dielectric Phenomena; IEEE: New Jersey, 2003; 546-550.
- 94 - Tanaka, T.; Kozako, M.; Fuse, N.; Ohki, Y.. Proposal of a Multi-core Model for Polymer Nanocomposite Dielectrics. *IEEE Transactions on Dielectric and Electrical Insulation* **2005**, *12*, 669-681.
- 95 - Li, K.; Liang, S.; Lu, Y.; Wang, Q.. Synthesis of Telechelic Fluoropolymers with Well-Defined Functional End Groups for Cross-Linked Networks and Nanocomposites. *Macromolecules* **2007**, *40*, 4121-4123.
- 96 - Hench, L.L.. Sol-Gel Kinetics. *Sol-Gel Silica*,; Noyes Publications: New Jersey, 1998; 8-23.

- 97 - Iler, R.K.. Colloidal Silica-Concentrated Sols. *Chemistry of Silica*,; John & Wiley Sons, Inc.: United State of America, 1979, 312-461.
- 98 - Ferrari, G.; Watling, J.R.; Roy, S.; Barker, J.R.; Asenov, A.. Beyond SiO₂ technology: Simulation of the impact of high- κ dielectrics on mobility. *J. Non-Cryst. Solids* **2007**, 353, 630-634.
- 99 - Vanderschueren, J.; Gasiot, J.. Field-Induced Thermally Stimulated Currents. In *Thermally Stimulated Relaxation in Solids*,; Bräunlich, P., Ed; Springer-Verlag Berlin Heidelberg: Germany, 1979; 135-223.
- 100 - Turnhout, J.V.. General Introduction. *Thermally Stimulated Discharge of Polymer Electrets*,; Elsevier Scientific Publishing Company: Netherlands, 1975; 1-24.
- 101 - Shimizu, H.; Nakayama, K.. Thermally Stimulated Depolarization Current Study of Molecular Motions in Polychlorotrifluoroethylene. *Jpn. J. Appl. Phys.* **1989**, 28, L1616-L1619.
- 102 - Grimau, M.; Laredo, E.; Bello, A.; Suarez, N.. Correlation between Dipolar TSDC and AC Dielectric Spectroscopy at the PVDF Glass Transition. *J. Polym. Sci., Part B: Polym. Phys.* **1997**, 35, 2483-2493.
- 103 - Mizutani, T.; Oomura, T.; Ieda, M.. Anomalous TSC and Space Charge in High-Density Polyethylene. *Jpn. J. Appl. Phys.* **1982**, 21, 1195-1198.
- 104 - Mizutani, T.; Kaneko, K.; Ieda, M.. Anomalous Discharging Currents due to Space Charge. *Jpn. J. Appl. Phys.* **1981**, 20, 1443-1448.
- 105 - Bucci, C.; Fieschi, R.; Guidi, G.. Ionic Thermocurrents in Dielectrics. *Phys. Rev.* **1966**, 148, 816-823.

VITA

Jason Claude was raised in Brooklyn, New York before moving to Cambridge, Massachusetts to attend the Massachusetts Institute of Technology. After bouncing from major to major, he finally settled into the Materials Science and Engineering department where he graduated with his BS in 2002. Upon graduation, he worked at several internships around the country before deciding to return to graduate school at the Pennsylvania State University in University Park, Pennsylvania also known as Happy Valley. He once again joined the Materials Science and Engineering department and received his MS in 2007 and is at the moment on the cusp of completing his PhD. After completing his degree, he plans on taking a lot of time off to relax and pursue his neglected photography before joining the DuPont Company.